DEVELOPMENT OF BRIGHT-FIELD MICROSCOPE IMAGE RESOURCE, AND IDENTIFICATION OF ROBUST FOCUS MEASURE FUNCTIONS FOR AUTOMATED CAPTURING OF IMAGES

A thesis submitted in fulfillment for the requirements of the degree of

Doctor of Philosophy

by

MOHAMMAD IMRAN SHAH

DEPARTMENT OF BIOTECHNOLOGY AND BIOINFORMATICS

JAYPEE UNIVERSITY OF INFORMATION TECHNOLOGY

WAKNAGHAT, SOLAN, HP, INDIA

OCTOBER, 2018

DEVELOPMENT OF BRIGHT-FIELD MICROSCOPE IMAGE RESOURCE, AND IDENTIFICATION OF ROBUST FOCUS MEASURE FUNCTIONS FOR AUTOMATED CAPTURING OF IMAGES

A thesis submitted in fulfillment for the requirements of the degree of

Doctor of Philosophy

by

MOHAMMAD IMRAN SHAH

DEPARTMENT OF BIOTECHNOLOGY AND BIOINFORMATICS

JAYPEE UNIVERSITY OF INFORMATION TECHNOLOGY

WAKNAGHAT, SOLAN, HP, INDIA

OCTOBER, 2018

`

TABLE OF CONTENTS

1.1. Type of Medical Data

1.2. Necessity of Medical Data

     1.2.1. Create the Basis for the Historical Record

     1.2.2. Support Communication Among Providers

     1.2.3. Anticipate Future Health Problems

     1.2.4. Standard Preventive Measures

     1.2.5. Identify Deviations from Expected Trends

     1.2.6. Support Clinical Research

1.3 Limitations of The Traditional Medical Record System

     1.3.1. Pragmatic and Logistical Issues

     1.3.2. Redundancy and Inefficiency

     1.3.3. Storage and management of medical images

     1.3.4. Influence on Clinical Research

     1.3.5. The Passive Nature of Paper Records

     1.3.6. Computer aided analysis of medical images

1.4 Solution for These Limitations

     1.4.1. Electronic Health Records (EHR)

1.5 Diagnostics in Developing Countries

1.6 Medical Imaging

     1.6.1. Radiology

     1.6.2. Histopathology

1.7 Computer Aided Diagnosis (CAD)

     1.7.1. CAD for Tuberculosis Diagnosis

     1.7.2. Differences between Radiology and Histopathology CAD System

     1.7.3. Automated Microscopy for Histopathological Diagnosis: an Automated CAD System

     1.7.4. Automated Microscopy for Tuberculosis Diagnosis

     1.7.5. Database Available for automated microscopy algorithm Development for Tuberculosis Screening

1.8. Problem Identification

1.9. Objectives of The Thesis

`

DECLARATION

I certify that:

a. The work contained in this thesis is original and has been done by me under the guidance of my supervisor.
b. The work has not been submitted to any other organization for any degree or diploma.
c. Wherever, I have used materials (data, analysis, figures or text), I have given due credit by citing them in the text of the thesis.
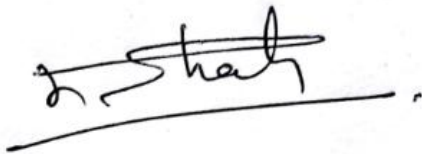
Mohammad Imran Shah   **Date: _____/_____/2018**

Enrollment No. 136504

Department of Biotechnology & Bioinformatics

Jaypee University of Information Technology

Waknaghat, Solan, India

CERTIFICATE

This is to certify that the thesis entitled, **"Development of Bright-field Microscope Image Resource, and Identification of Robust Focus Measure Functions for Automated Capturing of Images"** which is being submitted by **Mohammad Imran Shah (Enrollment No. 136504)** in fulfillment for the award of degree of **Doctor of Philosophy** in **Bioinformatics** at Jaypee **University of Information Technology, Waknaghat, India** is the record of candidate's own work carried out by him under my supervision. This work has not been submitted partially or wholly to any other University or Institute for the award of this or any other degree or diploma.

Late Dr. Chittaranjan Rout
Supervisor
Associate Professor
Department of Biotechnology and
Bioinformatics
Jaypee University of Information
Technology
Waknaghat, India

Dr. Udayabanu, M
Administrative Supervisor
Assistant Professor (Senior Grade)
Dept. of Biotechnology and Bioinformatics
Jaypee University of Information Technology
Waknaghat, India

Date: _____/_____/2018

ACKNOWLEDGEMENT

The list of the people I need to thank will not fit to a single Acknowledgement section. I just mention some people whose contribution is obvious. It is my privilege and honor to express my gratitude to the following without whose guidance and support I would not have been able to complete my Ph.D thesis.

My first debt of gratitude must go to my supervisor, **Late Dr Chittaranjan Rout**. The insuperable contribution and peer support rendered by my supervisor is incomprehensible. He patiently provided the vision, encouragement and advice necessary for me to proceed through the doctorial program and complete my dissertation. I want to thank **Dr Rout** for his unflagging encouragement. He has been a strong and supportive adviser to me throughout my doctorial career.

I would also like to thank my administrative supervisor, Dr. Duayabanu, M for his constant support for the completion of my final PhD viva.

I wish to thank my parents, **Mohd Rafiq Shah** and **Shakeela Shah,** and **grandparents, Mohd Hatim Shah** and **Khatun Shah**. Their love, support and motivation provided me inspiration and encouragement, and they were the driving force to successfully complete my work. I owe them everything and wish I could show them just how much I love and appreciate them.

I emphatically express my loyal and venerable thanks to JUIT administration, **Prof (Dr) Vinod Kumar (Vice Chancellor), Prof (Dr) S.D. Gupta (Director & Dean, Academics & Research), Maj. Gen (Retd.) Rakesh Bassi (Registrar), Prof (Dr) Y. Medury (Former COO, JES), Prof (Dr) S.K. Kak (Former vice chancellor), Brig (Retd.) K.K. Marwah (Former Registrar), Brig (Retd.) Balbir Singh (Former Registrar), Prof (Dr) T.S. Lamba (Former Dean, Academic & Research)** for providing opportunity to pursue a Doctorate Degree, teaching assistantship and advanced lab infrastructure to accomplish this scientific venture of my life.

I am also highly beholden to **Prof (Dr) Malay Sarkar, Prof Sanjeev Sharma, Indira Gandhi Medical College, Shimla** for their guidance, valuable suggestions and tremendous cooperation. I am also thankful to **Mr. Vinod Chauhan**, PG students and Technical Staff of Pulmonary Medicines and Radio-diagnosis Departments, Indira Gandhi

ABSTRACT

An efficient healthcare system always takes advantage of observation and interpretation of medical data that include narrative, textual data, numerical measurement, recorded signals, radiographs and pathological images. Medical imaging is one of the most important tools for disease diagnosis. Digitization and analysis of imaging data have been attracting attention in recent years due to their societal impact in the domains of diagnosis, observation and the training of doctors. From simple chest X-rays (CXR) to pathological microscopic images (sputum smear image) require the highest levels of quality for acquisition, storage and processing. Infectious disease like tuberculosis which is caused by *Mycobacterium tuberculosis* requires radiological (CXR) and pathological (sputum smear microscopy) tests for the effective diagnosis. The former is not a confirmatory test due to its non-specific and redundant patterns. Therefore, Ziehl-Neelsen stained conventional bright field microscopic (CM) test is the most widely used confirmatory method in low and middle income countries. However, the manual screening of tuberculosis bacilli using sputum smear CM microscopy may misdiagnose 33 to 50% of active cases due to patient load at the hospital. The majority of current issues on tuberculosis diagnosis can be addressed by incorporating automated methods. Autofocusing, auto-stitching, and image segmentation and classification are the three sequential steps in automated microscopy system for the tuberculosis screening. However, lack of unified datasets impedes the development of robust algorithms on these three domains. Keeping in view of these limitations, the proposed thesis work is based on four objectives which are described in the four different chapters (Chapter 2, 3, 4 & 5). In the 1st objective, Ziehl-Neelsen Sputum smear Microscopy image Database (ZNSM-iDB) has been developed to facilitate the development of algorithms and methods related to automated microscopy system, and it is freely available at http://14.139.240.55/znsm. In the 2nd objective, the robust focus measure functions were identified for the automated capturing of Ziehl-Neelsen (ZN) sputum smear images. In the 3rd objective, a robust hybrid focus measure function system was established as a universal method for auto-focusing. In the final objective, automatic bacilli segmentation was performed using watershed segmentation method to identify whether a patient is tuberculosis positive or negative. Accomplishment of these objectives has advanced the knowledge of automated microscopy development for tuberculosis diagnosis.

LIST OF ABBREVIATIONS

ANN	Artificial Neural Network
BGR	Brenner Gradient
CAD	Computer Aided Diagnosis
CM	Conventional Microscopy
COR	Correlation
C-SLFN	Compact-Single hidden-Layer feed-Forward Neural network
CT	Computed Tomography
CXR	Chest X-ray
DH	Digital Histology
DLP	Diagonal Laplacian
ECG	Electrocardiogram
EGR	Energy Of Gradient
HER	Electronic Health Record
EHS	Histogram Entropy
ELM	Extreme Learning Machine
ELP	Energy Of Laplacian
FM	Fluorescent Microscopy
FMF	Focus Measure Function
FSIM	Feature Similarity
GDR	Gaussian Derivative
GLV	Gray-Level Variance
GNV	Gray-Level Variance Normalized
HIV/AIDS	Human immunodeficiency Virus/ Acquired immunodeficiency Syndrome
HMLP	Hybrid Multi-Layered Perceptron network
HOG	Histogram of Oriented Gradients
HSM	Hemli And Scherer's Mean

HSV	Hue Saturation Value
ICR	Image Curvature
IGRA	Interferon-γ Release Assay
KC	Kinyoun Cold
kNN	k-Nearest Neighbor
LLV	Gray-Level Variance
M. Tuberculosis	*Mycobacterium Tuberculosis*
MDCT	Modified Discreet Coefficients Transform
MLP	Modified Laplacian
MoG	Mixture of Gaussians
MP	Mega Pixels
MRI	Magnetic Resonance Imaging
MS-1	Microscope-1
MS-2	Microscope-2
MS-3	Microscope-3
NM	Nuclear medicine
PACS	Picture Archiving and Communication System
PHOG	Pyramid Histogram of Oriented Gradients
PNN	Probabilistic Neural Network
RANSAC	Random Sample Consensus
RGB	Red Green Blue
RHS	Histogram Range
ROI	Region of Interest
RWC	Ratio of The Wavelet Coefficient
SD	Standard Daviation
SFB	Steerable Filters-Based
SFM	Spatial Frequency Measure
SGR	Squared Gradient

SIFT	Scale Invariant Feature Transform
SSIM	Structural Similarity
SURF	Speeded Up Robust Feature
SVM	Support Vector Machine
SWC	Sum Of Wavelet Coefficients
TB	Tuberculosis
TGR	Tenengrad
THR	Thresholded Gradient
TST	Tuberculin Skin Test
US	Ultrasound
VCR	Vollath's Autocorrelation
VGR	Tenengrad Variance
VLP	Variance Of Laplacian
VWC	Variance Of Wavelet Coefficients
WHO	World Health Organization
WSI	Whole Slide Imaging
ZN	Ziehl-Neelsen
ZNSM-iDB	Ziehl-Neelsen Sputum smear Microscopy image Database

LIST OF FIGURES

LIST OF TABLES

From the beginning, the treatment of any unhealthiness was always based on the observation and interpretation of medical data[1]. Collection and interpretation of these data into meaningful information is always primary to healthcare process whether it is early Greek literature for disease description, guideline and management, or the contemporary way of using laboratory and X-ray studies to diagnose and treat disease [1]. The total amounts of data that may be used in patient care have become enormous due to the technology advancement and use of medical imaging modalities to evaluate risks, prognosis and response to therapy. The crucial and vital role of gathering, analyzing and using data in the process of "decision making" is currently recognized as a core part of the entire healthcare [1]. This data helps to categorize or differentiate a subgroup of patient(s) from a larger population of patients. This data and its subsequent analysis also help a medical doctor to decide what additional information is required further, or how to gain a better insight in patient's problem and treat the diagnosed problem in the most effective way [1].

1.1. Type of medical data

The medical data ranges from narrative, textual data and numerical measurement to record signals, drawing, and radiographs and pathological images (Fig. 1.1) [1].

The first one (narrative data) is collected in the care of patients by asking several questions like symptoms of present illness of patient. Doctors verbally ask specific questions regarding the illness and recorded as text in the medical record which also includes the familial and social history, and the clinical report of physical examination. Traditionally, these narrative data were handwritten by physicians, clinicians and then stored in patient's medical records. Increasingly, the narrative summaries are transcribed by typist and included as electronic records which has several advantages than traditional one. It not only includes patient histories and physical examinations but also other descriptions like specialty consultations reports, pathologic tests, surgical procedures, and hospitalization details [1].

Several data in medicine uses discrete numeric values. These include laboratory tests, pulse rate, temperature, and certain measure during physical examination. However, the issue of precision becomes important in interpretation. For example, can physicians differentiate reliably between a 9-cm and a 10-cm span of liver during the examination of a patient's

abdomen? Is a fluctuation of 1-kg in weight since last week significant? Analog data in the form of continuous signals are particularly important in some fields of medicine. Electrocardiogram (ECG), a tracing of the electrical activity from a patient's heart is a well known example. A graphical tracing is included with a written interpretation when such data are stored in medical records [1].

Visual images acquired from machines (radiological or microscopic) or sketched by the physician are very important category of medical data. Radiologic images such as X-Ray, CT, ultrasound, MRI, etc., or pathological imaging (e.g. sputum smear microscopy) are the most significant tools for disease diagnosis and monitoring the progress of the treatment. These imaging data enable medical professionals to see the actual complications or treatment's effectiveness on internal body organs without surgical biopsies procedures [1].
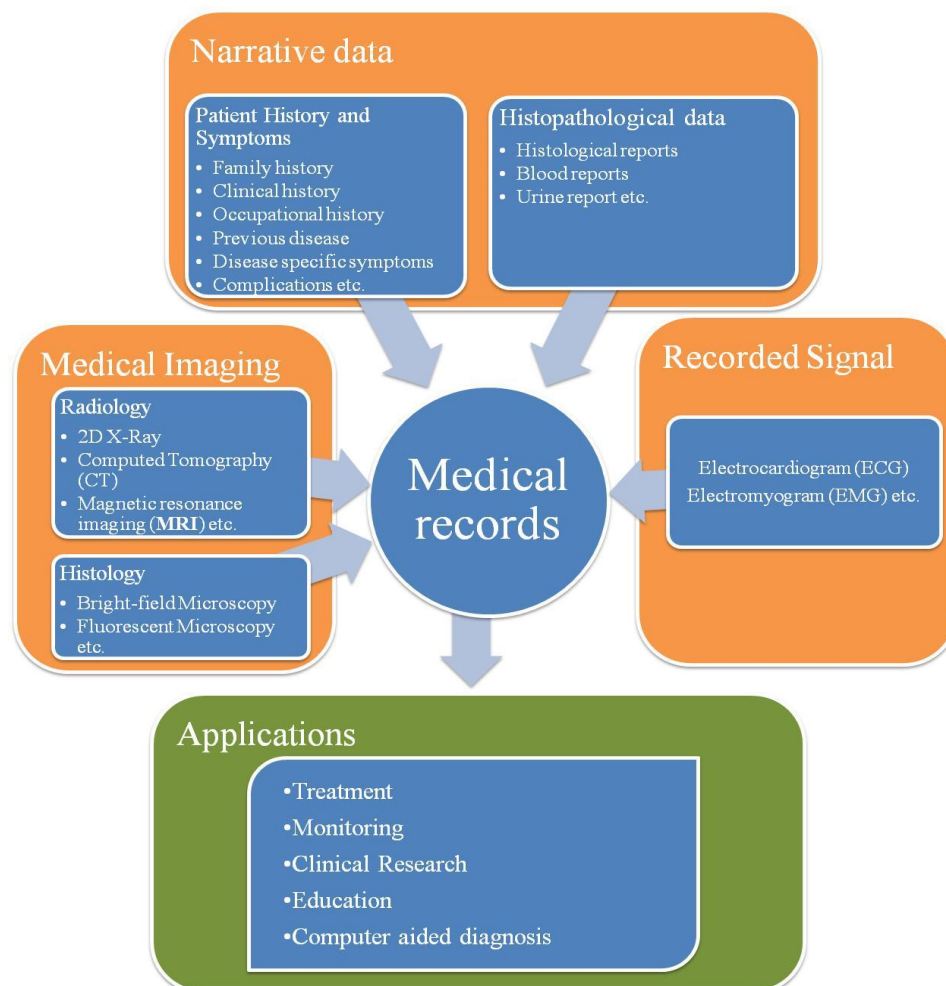
Fig. 1.1 Types of medical records and their applications.

1.2. Necessity of medical data

Healthcare data are recorded for a variety of reasons. Clinical data may be needed for proper treatment of the patient from whom they were acquired. It also can contribute to clinical research through the acquisition of knowledge through analyses of these data from populations of individuals [1, 4]. The major usages of medical data are as follow:

1.2.1. Create the Basis for the Historical Record

Medical records are intended to provide a detailed compilation of information about individual patients [4]. They provide the answers for the following questions.

- What is the patient's history (present illness; coexisting diseases; past illness that is resolved; familial, social, and demographic information)?
- What patient's symptoms have been reported? When they began, and what has provided relief?
- What physical signs have been reported on examination?
- What are the changes in symptoms and signs over the time?
- What types of laboratory results are available?
- What other tests, like radiologic, have been performed?
- What medications are being prescribed and are there any allergies reported?

1.2.2. Support Communication among Providers

In the recent years, emergence of specialization in healthcare professionals has emphasized the central role of the medical record [1]. Now this record not only contains observations by a physician for reference, but they also serves as a communication among physicians and other medical personnel who are dealing with same patients, such as physical or respiratory therapists, nursing staff, radiology technicians, etc [1]. In remote areas, patients receive treatment over time from a variety of physicians, and medical records enable them to avoid repetitive tests.

1.2.3. Anticipate Future Health Problems

Better health care not only involves responding to patients' health problems but also educate patients about how their environment and lifestyle could contribute to, or reduce the risk of, future progression of disease [1]. Clinical data are significant in identifying risk factors, and guiding patient for preventive interventions like diet, medication, exercise, etc.

1.2.4 Standard Preventive Measures

The medical record also used to provide data on interventions which have been performed to prevent several disorders [1, 9, 10]. For example, if a patient casualty room with a wound, the physicians check when the patient had a tetanus immunization. If this information is easily accessible in the record, it can prevent unnecessary treatments which may be costly or associated with risk [1].

1.2.5. Identify Deviations from Expected Trends

Sometime medical data is useful in examining temporal changes in patent's response to the treatment [1, 11, 12]. For example, the routine monitoring of children for normal growth and development by pediatricians is required [1]. Single observation regarding height and weight may not be informative, while multiple observations over months or years may provide the interpretation to a medical problem.

1.2.6. Support Clinical Research

Clinical data also support research through the statistical and other analysis of observations collected from population of patients to identify and validate common clinical patterns that can have general applicability [1, 13, 14]. Clinical research can also be performed on new large patient's datasets even for people who did not enrolled earlier in any clinical research directly, often called as retrospective studies. For example, risk of tobacco smoking based on statistics derived from populations with and without heart disease, lung cancer and other pulmonary disease [1].

1.3. Limitations of the Traditional Medical Record System

The preceding section highlighted the positive points of medical records storage and retrieval. However, medical professionals face the problems associated with traditional paper records, which limit their access leading to poor effectiveness for its anticipated use [1].

1.3.1. Pragmatic and Logistical Issues

Firstly, medical data can only be used effectively for the delivery of better healthcare if they are recorded in organized manner. It is important that the recorded data can be find when it is needed. For example, medical personnel should have easy access to the paper medical records in which data were recorded; he/she must be able to find the data within the record; he/she must be able to access specific information quickly; finally, once he/she find the data, is it easily to read or interpret. However, the traditional records fails to provide

aforementioned information efficiently and medical personal may not be able to use it for better healthcare services [1].

1.3.2. Redundancy and Inefficiency

Health professionals use variety of techniques to find data quickly in chart or medical records that leads to redundant recording [1, 17]. For example, radiological results or typically recorded on radiology reporting form, and same data often reported as brief notes in the narrative part of the chart. Furthermore, these results often mentioned in reports of admitting and consulting physicians and nursing staff. Theses redundant information accelerate the growth of paper document and complicates the management of medical data (chart). It is often difficult to access specific data due to this redundancy which often leads to re-capturing of the same data and again increase in redundancy by entering it to the records.

1.3.3. Storage and management of medical images

Management and storage of medical image is one of the biggest challenges in medicine [1, 18]. Patients with complicated medical problems may require several radiological studies when they consult doctors at different places. Therefore, these studies may be unknowingly duplicated. Simultaneous access to radiological images to multiple physicians may be needed for better interpretation. The film-based radiological system cannot meet these expectations, and may lose as storage of these films is relatively high.

1.3.4. Influence on Clinical Research

Retrieving information from traditional record is tedious, laborious and time consuming task which is prone to transcription errors. It requires several days to extract and format data for their structured statistical analysis [1, 19]. Often, huge medical data is untouched in paper record because there is no easy and efficient way to extract and analyze these data.

1.3.5. The Passive Nature of Paper Records

Another limitation of paper records is that traditional medical system is manual [1]. The chart is insensitive to the properties of the data recorded in the same page. Paper records cannot respond to the implications present in their pages [1].

1.3.6. Computer aided analysis of medical images

In recent years, automation of diagnosis process has been the attraction point for researchers. Analyzing medical or pathological images requires them in digital form which is not feasible with traditional film records. Therefore; traditional records keeping process is the main

bottleneck in development of computer aided diagnosis which can provide second opinion to the doctors regarding the disease.

1.4. Solution of these limitations

Medical data contains narrative, numerical, signal and two-dimensional and three dimensional images [20]. Currently, digitization of such data is underway to unify patient information, accelerate information access, prevent loss of any data and improve the diagnosis process [20]. The ultimate aim of the digitization of medical data is to create a paperless/filmless system to quickly access the entire patient's information anytime and anywhere [20]. Digitized system address all the issues associated with traditional Medical Record System. This digitized system with all the facilities is called electronic health record (EHR).

1.4.1. Electronic Health Records (HER)

Electronic health record (EHR) systems address all these practical problems of traditional paper records, and film of radiological and pathological images. Therefore, several hospitals and individual practitioners are implementing EHRs.

Presently, the term EHR represents the comprehensive, cross-institutional, and longitudinal collection of healthcare data [21]. It not only includes the data related to patient's medical treatment but also patient's health in general. The patient is actively involved in his/her treatment by accessing, adding, and managing his/her healthcare data [21]. Automated record systems in EHR provide the opportunities for dynamic responses to the data that is being recorded. Computational techniques make it possible to develop the record systems that can monitor their contents and produce warnings or advice for providers based on observation and trends erroneous data [1].

EHRs overcome the need to retrieve the hard copy of charts, and researcher can use computational data retrieval and analysis techniques to find specific patients, locating relevant data, and formatting the data for statistical analyses (Fig. 1.2) [1].

Picture archiving and communication system (PACS): Most of the medical data such as textual and numerical information can be handled without specialized hardware and software. Whereas medical images cannot be stored and managed in the usual manner; rather, specialized software and hardware are required to store, retrieve and view these images. A specialized system is known as picture archiving and communication system (PACS) [22]

which generally include one or more imaging modalities consisting images of a patient using X-ray, computed tomography (CT), magnetic resonance imaging (MRI), nuclear medicine (NM), and ultrasound (US), microscopic images, to name a few. This PACS system addresses the limitations of film-based systems by providing storage, rapid retrieval and simultaneous access to images acquired with multiple modalities at multiple sites [22].
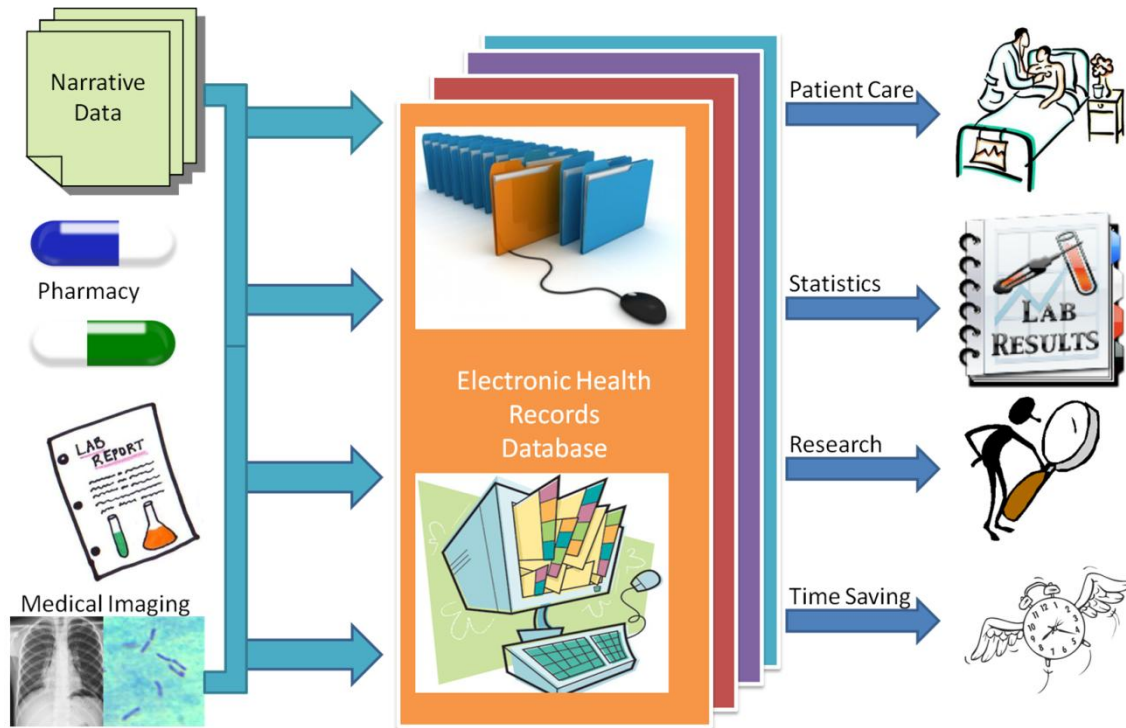
Fig. 1.2 Electronic health record contents and its applications

Digitization and storage of medical images on centralize computer system also provide the opportunity to automatically analyze these high resolutions images using CAD approaches. Automated analyses provide faster and effective results with less human interventions that could be used as second opinion regarding a disease. Automation also helps in the early diagnosis of the disease as several patients data can be visualized on the go in lesser time. These CAD systems can also improve the accuracy of poorer test like bright-field sputum smear test by analyzing large numbers of images.

1.5. Diagnostics in developing countries

Several low- and middle- income countries with poorly resourced healthcare systems are burdened with levels of infectious disease. However, tuberculosis (TB), Ebola and HIV/AIDS remain major public health concerns and are the most frequently recorded cause of adult death in parts of sub-Saharan Africa [23]. Laboratories in developing countries are often limited and access to these laboratories is difficult by economic or geographical factors.

These laboratories also have limited resources, and basic amenities like electricity and water may not be available properly. Lack of skilled technical is also a problem in some countries, particularly in remote areas [23]. Majority of population may not used particular diagnostic test for infectious diseases due to its high cost or lack of robustness [24]. Appropriate tests have not yet been developed for tropical or neglected diseases. Weak regulation and protocols have also contributed to poor diagnostics services. In some countries, tests of unknown or low quality are sold without any obstacle [25, 26].

Tuberculosis is an endemic disease that affects people worldwide. In 2015, 10.4 million new cases of TB reported; therefore, WHO has started several initiatives to eradicate TB [27]. However, In spite of WHO recommendation for sputum smear fluorescent microscopy test for tuberculosis screening, low and middle income countries are using less accurate conventional sputum smear test due its low cost, easy availability, least expertise and minimal bio-safety standard [28]. Also, the most accurate and gold standard test like culture is time-taking and not feasible due to the higher patient load in TB-endemic countries [29]. Technological advances like computer aided diagnosis (CAD) and the development of novel devices that can be used outside of the laboratory have the potential to overcome some of the challenges faced by healthcare providers in developing countries [30]. The CAD can improve the accuracy and reduce the time complexity of poor test like conventional microscopy or non-confirmatory chest X-Ray. As we already discussed, the digitization of medical data, including medical images, is primary step to provide better healthcare outcomes by managing record electronically and using CAD system for disease screening.

In the following sections, medical imaging modalities, digitization and computer aided diagnosis (CAD) using medical images are discussed. Initially, all the available imaging techniques (radiology and histopathology) with their limitations are described. Furthermore, CAD and its assistance for tuberculosis diagnosis and their limitations are discussed. Finally, Automated CAD for histopathology images (automated microscopy) with their limitations is presented.

1.6. Medical Imaging

1.6.1. Radiology

(i). Different radiological imaging modalities

An imaging modality is a particular imaging technique or system that is used to capture abnormalities in internal part of bodies. In this section, we have provided a brief overview of common imaging modalities.

Two-dimensional radiography (2D X-ray), computed tomography (CT), and nuclear medicine use ionizing radiation. The first two transmit x-rays through the body part, and body's tissues selectively reduce the x-ray intensities to form an image [31]. These modalities transmit the energy through body; hence, termed as transmission imaging modalities. In nuclear medicine, radioactive compounds are injected into the body that moves selectively to different organs or regions within the body. These compounds emit gamma rays with different intensity based on the compound's local concentration [31]. Radioactive sources emit radiation from within the body; hence, nuclear medicine is also termed as emission imaging modalities.

Ultrasound imaging modalities transmits the high-frequency sound into the body and receives the echoes from structures within the body. This method relies on acoustic reflections to create images; hence, often called reflection imaging. Finally, magnetic resonance (MRI) requires a strong magnetic field and radio frequency Faraday induction to image properties of the proton nucleus of the hydrogen atom. This technique exploits the property of nuclear magnetic resonance; hence, called magnetic resonance imaging [31].

Different modalities reveal the different properties of human body or organ. Therefore, it is often useful to use multiple imaging modalities to capture images from a patient. This is called medical image fusion. For example, CT and MRI can be combined to look at bones and soft tissues, respectively, or MRI and PET can be used to examine brain structure and brain function, respectively. Similarly, CT and PET are particularly useful for combining functional and structural information, respectively and also because the CT data can be directly used to improve the reconstructed PET images. Therefore, virtually all modern PET modality systems are sold as PET/CT systems that integrate the two modalities in a single platform [31].

(ii). Limitations of Radiology

Radiation exposure is the main disadvantage of radiology which can cause cancer and other health issues. Ionic radiation, a proven carcinogen, is the high frequency form of radiation. Even chemical used to develop x-ray films can be hazardous (Applied Industrial Hygiene). American Cancer Society has linked radiation to the breast cancer, thyroid cancer, skin cancer, lung cancer, stomach cancer and multiple myeloma [32, 33]. Barium, a chemical used in x-ray diagnostic work, can cause harm to patient undergoing radiography. According to Los Alamos National Laboratory's Chemistry Division website, Barium can cause deathly anaphylaxis, an allergic. Radiography has also linked to the sterility in men and women. It is reported that male radiographers were at a higher risk for reproductive problems. In women who partnered with the male radiographer, a higher rated of miscarriages were reported. Congenital anomalies, infertility and still births were also higher among the radiographer group [34].

Sometimes, ultrasound results may identify an area as potential concern that is not malignant. These false-positive results could lead to more complicated procedures like invasive biopsies which are not essential . The higher false-positive results with ultrasounds than with mammography (2.4%-12.9% for ultrasound and 0.7%-6% for mammography) were reported . Several cancers cannot be diagnosed via an ultrasound . Sometime calcifications are not visible on ultrasound scans; therefore early diagnosis of the portion of breast cancers that begin with calcifications can be neglected .

MRI generates powerful magnetic fields which will attract metal objects. It can also pull any metal containing objects inside the body, such as aneurysm clips and medicine pumps. MRI scan can cause malfunction of pacemakers, cochlear implants and defibrillation devices .

1.6.2 Histopathology

Histopathology is used to diagnose the diseases using microscopic examination of a biopsies or surgical specimens that are processed and fixed onto glass slides [39]. One or more stains are used to dye sections so that different components of the tissue can be visualized under the microscope [39]. One stain is used to reveal cellular component or bacterial, while counter stains are used to provide contrast. Hematoxylin-Eosin (H&E), Ziehl-Neelsen (ZN) and Auramine-O stain are the most popular staining techniques. The first-one stains cell nuclei blue, while the counter Eosin stains cytoplasm and connective tissue pink [40]. Similarly, ZN staining is used in conventional bright field microscopy (CM) whereas Auramine-O staining

requires fluorescence microscopy (FM). These are the most widely used non-invasive techniques for the screening of endemic infectious disease like tuberculosis by sputum smear. CM is used in low and middle income countries, and employed as primary technique for tuberculosis screening due to its low cost and minimal bio-safety standard, while FM is in practice in developed countries due to its better sensitivity rate.

Digital histology diagnostics: Digital histology (DH) is the process by which histology slides are digitized to produce high-resolution images. DH is becoming more common due to the growing availability of computerized whole slide digital scanners [41]. Whole slide scanners have addressed the issues associated with previous static and live systems [42]. There are several advantages of digitization of histology images:

- Digitization of microscopic slides facilitates telepathology, i.e. the transfer of digital images of pathology across several locations for the diagnosis, research and education. It also has the potential to improve clinical service by reducing the need of storing glass slides physically, and reducing the risk of slides getting lost or broken.

- Automated image analysis will enhance diagnostic efficacy in histopathology. Automated screening of pathogens like Mycobacterium *Tuberculosis* can also be performed by developing automated algorithms. This automated system will assist pathologists in efficient and accurate diagnosis. It can also facilitate the mass screenings in shorter time for endemic diseases.

1.7 Computer Aided Diagnosis (CAD)

Radiology is facing the problems by its own success [43]. The number of expert radiologists still is limited, the workload of radiologist has increased drastically, and the costs of medical imaging have increased fast [44]. Novel approaches are needed to handle the rapid increment of imaging data. The CAD can overcome this problem by speeding up the diagnosis, improving the quantitative evaluation and reducing the diagnostic errors. CAD also stands for computer-aided detection as it is mostly used for the detection of disease condition. The CAD provides second opinion in medical image interpretation [44-54]. These CAD systems can be a game changer in resource limited low- and middle-income countries where radiologists and pathologist are limited but the patent load is significantly higher due to the endemic disease like TB, HIV and Ebola. The CAD facilitates radiologists for mass screening of cases in faster and effective manner by decreasing inter-observer variation. This method also provides the quantitative support for clinical decision like whether biopsy is required or not for the disease confirmation. This method helps in reducing the false-positive biopsy and

thoracotomy. One of the major applications of CAD is the identification of tumor's benignancy/malignancy [48, 49, 54-58]. To differentiate between disease or control cases, CAD performs mainly three steps: feature extraction [48, 50, 51, 58-62], feature selection [62-65] and classification. These three steps need to be performed in efficient manners for better performances of whole CAD system.

1.7.1. CAD for TB diagnosis (*Jaeger, S et al., 2013*)

Computer and medical scientists are not only working for CAD in cancer diagnosis but also for endemic disease like tuberculosis which affects mainly the lung. Generally, patient with TB undergoes X-ray study to screen active TB, and ensure a proper treatment [66]. Standard chest X-ray (CXR) is an inexpensive test to screen the TB in patients, but interpretation of it is subject to human error and depends on the expertise of radiologist [66-70]. Furthermore, manual mass screening of large population is a time-consuming and laborious task which needs considerable amount of time and efforts. Therefore, the development of CAD for TB detection has great importance in TB-endemic countries. This system can provide the mass screening of cases with minimal detection error with higher accuracy rate.

The abnormalities in the CXR of TB patients show the changes in texture and geometry of the lungs [66]. Therefore, previous studies described the methods for texture and geometry feature extraction to classify CXRs as TB-positive or negative [68, 71-85]. Some studies try to address TB diagnosis as a whole, while others address only a specific TB manifestation. Chauhan et al. (2014) used Gist and PHOG features in CAD of tuberculosis without segmentation [86]. They have used Gabor, Gist, histogram of oriented gradients (HOG), and pyramid histogram of oriented gradients (PHOG) features extracted from the whole CXR image to discriminate between TB and non-TB CXRs in an automated manner.

TB detection is the complex process as it posses large variety of TB manifestation, which ranges from subtle milliary pattern to obvious effusions [66]. Several texture abnormalities occur in TB but these are also occurred in other diseases that make them unspecific [66]. The CXRs of some active TB patients does not exhibit any of above patterns and looks normal to the human eye, and some do demonstrate very subtle findings that may be missed by the radiologists [87]. Therefore, CXRs are not the confirmatory test for TB diagnosis.

1.7.2. Differences between Radiology and Histopathology CAD System

Currently, the CAD systems for radiological imaging modalities are being used in diagnosis of different diseases [39]. However, the questions arise that can this CAD enable disease detection overcome inherent limitation associated with spatial resolution of radiological data [39]. For example, in mammography, the CAD systems have been developed to automatically classify the mammographic legions, whereas in histopathology, simple identification of presence or absence of tumor/legion may not be as important as sophisticated finding such as what is the stage of cancer [39]? Furthermore, on histological (microscopic) scale, different subtypes of cancer can de differentiate which is quite difficult or impossible in radiological scale.

CAD for histopathology is still evolving, and pathology data are not as well articulated as some of radiological problems being investigated. This is may be due to the enormous density of data that histology posses compare to radiology. Histopathology images are required to be processed in multi resolution framework due to their relatively large size and content. Also, radiological CAD mostly deal with gray-scale images, while histopathological CAD system require to process color images. These fundamental differences in histopathology and radiology data have resulted in the need of specialized CAD approaches for histopathology data.

1.7.3. Automated microscopy for histopathological diagnosis: an automated CAD system

Generally, the CAD systems are semi-automated and need radiologist or pathologist intervention to input the images, select region of interest, and segment the images. An automated CAD system requires minimal intervention of humans for diagnosis. Here, automated microscopy: an automated CAD system for diagnosis from microscopic image is discussed in detail. Automation of microscopy prevents physical & mental fatigue and reduces the time of view-fields analysis [28, 29, 88, 89]. Further, it allows to store and share image as an electronic health record for review of cases in future for monitoring diagnosis processes. Therefore, automations could assist diagnosis with better sensitivity and specificity [29, 88, 89]. The automated microscopy requires efficient algorithms in following three domains: **(i) autofocusing, (ii) autostitching and (iii) object segmentation and classification.**

(i). Autofocusing: Generally, autofocus technology calculates a focus value for each image captured at different focus position by moving the microscope objective lens. Autofocusing

of any imaging system is accomplished by searching for the focal length that provides the best focused image [28, 29, 90-93]. In a stack of images captured from a single view-field with different focuses, an image with the best average focus over entire view-field is defined as the focused one. Generally, a focus measure function (FMF) processed all the pixels in the images to calculate the degree of focus. In spatial viewpoint, a focused image can be thought of as one that has higher intensity difference among neighboring pixels. While in a frequency viewpoint, higher frequencies component are directly proportional to the degree of focus. Higher the frequency contents, the better focused is the image. The maximum/minimum value of the FMF corresponds to the best-focused image [94]. This method would facilitate automated capturing of the best-focused image. In recent years, various autofocusing algorithms have been proposed and implemented in microscopy images including fluorescence and conventional microscopy for various biological applications [28, 90-105].

(ii). Autostitching: This method stitches view-fields of a smear-slide to form a mosaic or virtual-slide map. This technique facilitates whole slide imaging (WSI), which can be stored in high resolution and can be used further for CAD, research and education. Though many autostitching methods were developed [106-108], they were not validated on diverse datasets. Many studies have already been performed for image stitching that used Harris corner detection [109], and scale invariant feature transform (SIFT) [110, 111] and speeded up robust feature (SURF) feature extraction algorithms for extracting features. A MicroMos, open-source software, builds mosaics using digital microscopy images of view field [108]. Autostitch software uses SIFT features extraction technique for image stitching to building slide map [106].

(iii). Object segmentation and classification: Object segmentation and classification step is similar to the semi automated CAD. Segmentation and classification algorithms detect the objects based on their shape, size and color, and classify image into different categories such as diseased and non-diseased. Generally, object segmentation and classification is performed in to two steps: (a) segmentation and (b) Feature extraction and classification.

(a). Segmentation
Segmentation is the process of partitioning the image into more meaning full regions and identify region of interests for further processing. Segmentation helps to focus on only specific region of interest (ROI), and then remove unwanted regions to improve the accuracy of classification techniques. In recent years, several segmentation algorithms have been

proposed which follow the discontinuity or the similarity principle [29]. Segmentation enables us to differentiate between ROI and background pixels. Several segmentation methods have been proposed for segmenting *M. tuberculosis* to detect TB. These methods can be broadly classified as (i) thresholding methods, (ii) neural network-based approaches, (iii) K-means clustering, (iv) fuzzy segmentation, (v) Bayesian segmentation, etc [29]. For example, color is the most important feature previously used to detect *M. tuberculosis* by above mentioned methods. In ZN stained microscopy bacteria and background turned red and blue respectively [112], while in auramine-O stained fluorescent microscopy, bacteria appears in the range between green and yellow and background turns to black [113]. Most of the previous studies had used color-based segmentation [29].

(b). Feature extraction and classification

Segmentation itself cannot provide accurate results as small artifacts and unwanted region may still present in the images. Standard classification methods can be used to extract true objects from the images [29]. These methods use set of features which can characterized these objects in a better manner. For an instance, the shape of *M. tuberculosis* bacteria are rod shaped with length of 1-10μm [114]. Eccentricity, axis ratio, perimeter, area, Hu's moments and Fourier descriptors were commonly used shape feature descriptors that were being used to extract the shape of *M. tuberculosis* bacilli [29]. Once the feature vectors are obtained, bacilli can be separated from non-bacillus object using various classification techniques. Several methods such as support vector machine (SVM), k-nearest neighbor (kNN) classifier, Bayesian classifiers, artificial neural networks (ANNs) and probabilistic neural networks (PNNs) are used for classifying objects like bacteria, cell etc.

1.7.4. Automated microscopy for tuberculosis Diagnosis

Apart from CXR, variety of other methods such as tuberculin skin test (TST), sputum, smear microscopy, culture test, interferon-γ release assay (IGRA), and GeneXpert are available for TB screening. However, microscopic (histopathological) examination of extracted sputum from the lung using a bright field microscope is the most widely used confirmatory method due to its low cost, requirement of least expertise, easy to perform and obtaining fast results [29].

Sputum smear test can be performed either by conventional bright field microscopy (CM) or fluorescent microscopy (FM). Former is in practice in low- and middle-income countries due to its low cost, easy to handle and minimal bio-safety standards [28, 29, 115].

The World Health Organization (WHO) recommended that at least 100 view-fields of CM images need to be observed to infer a patient as TB-positive or negative, but microscopist only observe very few view-fields due to the high load of patients in TB-endemic countries [28, 116]. As a result, this test exhibits high false negative rate and misdiagnose 33-50% of active TB cases [29], especially in the cases of extra-pulmonary, pediatric or patients co-infected with HIV due to very low bacterial load in their sputum [117]. Majority of current limitations on TB screening can be addressed by CAD that increase the sensitivity and specificity by analyzing 100-300 view-fields of CM images in an efficient and fast manner for *Mycobacterium tuberculosis* identification [89].

Automated microscopy could provide a better and faster diagnosis in TB endemic countries where mass screening of cases is needed. Automated microscopy needs least human intervention to screen the TB cases. Therefore, early and mass screening of TB patient can be performed in an efficient manner in TB-endemic countries like India. Several efforts were made in this direction, but researchers did not attain success on major level due to the different factors like changes in image contents, presence of debris, improper staining of sputum smear slides, etc. The availability of fully automated systems is limited, and these systems are in initial stage of development. For example, Lewis et al., (2012) have developed an automated TB screening system called TBDx for auramine-stained smear fluorescence microscopy [118]. It is capable of automatic loading of slides onto a microscope, focusing, digital capturing of images and then classifying the sputum smear as positive or negative using image processing techniques. However, it is still in Proof-of-Concept stage and attainment of success is limited [118]. As per author's knowledge, no automated microscopy system is available for TB bacilli screening using conventional microscope. The following section discusses the past work on automated microscopy algorithm development for TB diagnosis. As discussed earlier, algorithms were developed for autofocusing, autostitching and bacilli segmentation and classification for conventional and fluorescent microscopes.

(i). Autofocusing of sputum smear images

In recent years, several studies have been performed related to autofocus algorithms development for automated capturing of sputum smear images from fluorescent and conventional microscopes. Some of those studies are discussed below:

A comparative evaluation of different focus measure functions (FMFs) have been performed by Mateos-Pe´rez et al. [98]. Authors have determined the accuracy as well as time complexity of all the implemented algorithms to check their feasibility to implement in real-

time systems. Robustness of these algorithms to different imaging conditions like filtering, noise and uneven illumination were also tested. It is observed that filtering with appropriated filter size can reduce the mean error, while the noise level can significantly deteriorate the performance of autofocus functions. Modified discrete coefficients transform (MDCT) and Tenengrad (TNG) has performed better in term of accuracy.

The comparative evaluation of different autofocus algorithms were also performed on conventional bright-field microscopes (Ziehl-Neelsen and Kinyoun stained). Junior et al. [97], CostaFilho et al. [94], Russel et al. [102] and Osibote et al. [28] separately evaluated autofocus functions on conventional microscopic images. Junior et al. and CostaFilho et al. have evaluated nine FMFs and suggest that variance and entropy are the best focus measure functions in term of accuracy and computational time, respectively. Russel et al. considered only three (Gaussian derivative, variance of a log histogram and the energy of the image Laplacian) FMFs in their study and not included variance and entropy FMFs which have performed better in aforementioned studies. In this study, the energy of the image Laplacian outperformed others. Osibote et al. have evaluated six FMFs and recommended that Vollath's F4 and Brenner gradient are better in term of accuracy. Variance and entropy were not considered in this study.

Although several FMFs have been proposed for autofocusing, there is no single FMF that performs best for all type of imaging contents and modalities. Their performance depends on various factors like noise, image characteristics, debris and artifacts, and the background of image. For example, FMFs performed differently in FM and CM images as features acquired from both the modalities are different. In several studies, authors have applied different filtering techniques to get rid of noise and improve the performance of FMFs. However, implementation of preprocessing techniques increases the computational time. Generally, the time complexity of most of the FMFs are in the order of $O(MN)$, where M and N are image dimensions in the x and y direction, respectively. However, the total acquisition time also vary due to the step motors, experimental setups, etc. A comprehensive and extensive study considering all the commonly available FMFs is required to identify a robust FMF for conventional microscopic images. It is also required to identify a robust FMF which can perform better on different imaging modalities like conventional and fluorescent microscopes.

(ii). Autostitching of sputum smear images

WHO recommended analysis of 300 view-fields which can be achieved faster and efficiently by automated stitching of overlapping view-fields to make a mosaic (virtual slide map), and number of bacilli can be determined by using segmentation methods [119]. The bacilli segmentation algorithms use bacilli shape and size as the potential features to identify the bacilli from the other objects [113, 120]. Therefore, the autostitching also facilitates automatic detection of bacilli on the edge by joining half bacillus structures on the boundaries of two different view-fields.

To achieve autostitching in bright-field TB microscopy, Bhavna et al. (2013) [121]proposed a method that uses geometric hashing technique for model-based object recognition [122-124]. This technique was also applied to the microscopy of lung and prostate tissue [125] and microscopy of integrated circuits [126]. Robustness of this algorithm was evaluated on real distorted query images. Dogan et al. (2014) have used four different steps to perform autostitching of ZN stained images [127]. In the first step, feature extraction was performed by SIFT (scale invariant feature transform), Harris corner detection and SURF (Speeded Up Robust Feature) feature extraction algorithms. In the second step, feature point matching was performed among the different images. Nearest Euclidean distance and cross-correlation algorithms were used to find relation between feature points of different images. In the third step, minimization of matching error and model fitting were performed by RANSAC (random sample consensus) method. Finally image blending was performed to compose to images into one large image.

Chauhan et al., 2015 have also performed autostitching of ZN stained images [128]. The overlapping subparts of the view-fields were stitched together into a mosaic using scale-invariant feature transform (SIFT) feature extraction and random-sample-consensus (RANSAC) selection method. The divide and conquer algorithm was implemented for faster stitching and mosaic formation. Comparison of similarity between original and stitched image was performed using correlation (COR), structural similarity (SSIM) and feature similarity (FSIM) methods.

(iii). Bacilli segmentation and classification
It is the process of segmentation and counting of bacilli either from a view-field or stitched mosaic or slide-map. Pattern recognition and machine learning techniques have been used to detect the bacilli in images [113, 116, 120, 129-131][4, 5, 7, 12, 21, 22], but their efficacy and scopes are limited due to the implementation on non-unified and limited datasets.

Automatic TB bacilli segmentation on bright-field microscopic images was performed first time by Costa et al. [129]. They have eliminated green channel from their RGB images as their analysis shows that bacilli are more visible in R(-G)B images than RGB or HSV images. Artifacts present in the segmented images were removed using morphological and size filters. However, the sensitivity of method was low. Sadpal et al. [132], have used a Bayesian segmentation method to segment *M. tuberculosis*. Shape features were used on segmented object to classify whether the segmented object is true or false bacilli. In this study, axis ratio and eccentricity were used as shape feature. Authors have also incorporated size-invariant shape selection which allows to segment bacilli in differing magnification and to increase the robustness of method. However, experimental analysis shows that method was not promising in identifying overlapping bacilli.

Makkapati et al. (2009) later proposed an approach based on HSV color space [112]. Adaptive hue range was selected to segment the bacilli. However, the segmented objects also includeed artifacts and out-of-focus bacilli. Therefore, the beaded structures inside the segmented objects were considered to refine the segmentation results. In 2009, Sotaquir´a et al. [116], performed bacilli segmentation on RGB, LAB, HSV, YIQ and YCbCr color spaces and achieved the best results on YCBCr color space with fewer false positives.

Osman et al. [133] have used the hybrid multi-layered perceptron network (HMLP) for the detection of TB bacilli in HSV color space. In another study, Osman et al. [28] performed image segmentation using moving k-means clustering followed by feature extraction using Zernike moments. In both the studies, authors have implemented 5x5 median filter to remove unwanted objects in the image. Neural network based approaches were also used in some other studies [134-136] to segment TB bacilli. In Osman et al. (2011) [135] study, a single-layer feed-forward neural network was used for the segmentation of TB bacilli. This network was trained by extreme learning machine (ELM) technique. In Osman et al., (2010) [134], genetic algorithm-neural network (GA-NN) was used. Although above methods produces acceptable results, the effectiveness of the proposed method was limited in different imaging backgrounds.

Khutlang et al. have performed two separate studies in which a combination of pixel classifiers was proposed to detect the TB bacilli from convention bright-field images [120, 137]. In the first study, a combination of two-class pixel classifier was used to segment and classify bacilli [137]. Feature subset selection and Fisher trans-formation were used to extract

the features from the images followed by the classification of TB bacilli. In second study, two one-class classifiers were used for bacilli screening [120]. One class was used to classify pixel and other class was used to classify object. The former class uses color features and pixel intensity values followed by invariant feature extraction of geometric transformation, while latter one uses shape features (such as compactness, eccentricity, moments and Fourier features). Different classifiers such as Gaussian, mixture of Gaussians (MoG), principle component analysis, and the K-nearest neighbor using ROC were evaluated on extracted shape features. Nevertheless, these methods are unable to detect overlapped bacilli.

Even though many methods were presented for TB bacilli segmentation from conventional microscopic images, one common drawback of most of the methods is their inability to classify touching or overlapped bacilli as true bacilli. Most of the available methods do not work on overlapping or occluded bacilli, and they detect it as artifacts. Sometime smear slides contains large number of occluded bacilli that may be missed in screening process, and false negatives cases may increase. Therefore, algorithms to deal with this type of problems are needed.

1.7.5. Database available for automated microscopy algorithm development for tuberculosis screening

Mateos-Pérez et al., 2012 have developed an image database for autofocusing algorithms evaluation on auramine-stained sputum smear fluorescent microscopy images [98]. Database contains three hundred stacks belonging to 10 different TB-positive patients. Each stack consisted of 20-images acquired at different focus points using a constant Z step (Z = 3 μm) over the same view-field. This database does not contain datasets for autostitching, and segmentation and classification. However, the best focused image of every stack can be used for bacilli segmentation and classification.

Costa et al. [138] have developed an image database for testing TB bacilli detection in 2014. The database comprises two parts: an autofocus database with 1200 images and a segmentation and classification database with 120 images. The ground truth was also marked, which can be used as gold standard for the validation of the algorithms. Images with different background in the database will help to do extensive experiments to see how the existing and new algorithms perform on various conditions. However, images in this database are not Ziehl-Neelsen stained. This database contains Kinyoun-stained sputum smear bright-field images from single microscope for autofocusing and bacilli segmentation [37], and bacilli in

these images are less visible than those in ZN-stained images. Bacilli detection using Kinyoun-stained images had low sensitivity, and tuberculosis-affected countries do not use this staining for smear microscopy test [38]. Apart from staining, datasets for autostitching methods are not available in this database. This database contains only two categories of images, which are low and high density background. Therefore, a unified and diverse resource for automated microscopy development using Ziehl-Neelsen stained sputum smear images is needed.

1.8. Problem Identification

Limitations of current diagnosis techniques in developing countries motivated us to contribute towards better disease diagnosis by implementing image analysis techniques. The proposed work has focused on improving diagnosis of tuberculosis as it is ranked 1st alongside HIV for worldwide death by single infectious agent.

As discussed earlier, conventional sputum smear microscopy test is a primary and most widely techniques in TB-endemic developing countries like India which accounts for highest number of TB incidence (2.2 million). This technique is cost effective, need least maintenance and expertise, and has minimal bio-safety standards. However, the sensitive is the limiting factor for this test. Sensitivity of CM is 10-20% less than FM test. CM needs the higher numbers of view-fields to examine as the images are acquired at 100x magnification, while FM is acquired at 40x magnification. Therefore, the current work has put the efforts to improve the tuberculosis diagnosis using CM images.

1.9. Objectives of the Thesis

To overcome the limitations of automated microscopy domain, we have defined the following four objectives.

1. *Development of a **Z**iehl–**N**eelsen **S**putum smear **M**icroscopy image **D**ata**B**ase (ZNSM-iDB) which facilitate the validation of automated microscopy algorithms.*
2. *Identification of robust focus measure functions for the automated capturing of focused images from Ziehl-Neelsen stained sputum smear microscopy slide.*
3. *Establishment of hybridized focus measure functions as universal method for auto-focusing.*
4. *Automatic detection and classification of tuberculosis bacilli from ZN-stained sputum smear images using watershed segmentation.*

1.10. Organization of the Thesis

The thesis has been organized into distinct six chapters as follows.

In this chapter (Chapter 1), introductory part and related work of the thesis has been presented. In Chapter 2, a newly developed **Z**iehl–**N**eelsen **S**putum smear **M**icroscopy image **D**ata**B**ase (ZNSM-iDB) has been presented which can assist the development and validation of automated microscopy algorithms. In Chapter 3, a systematic analysis on identification of robust focus measure functions for the automated capturing of focused images from Ziehl-Neelsen stained sputum smear microscopy slide has been discussed. In Chapter 4, a detailed study is provided on establishment of hybridized focus measure functions as universal method for auto-focusing. In Chapter 5, a study on automatic detection and classification of tuberculosis bacilli from ZN-stained sputum smear images using watershed segmentation has been presented. In final chapter (Chapter 6), conclusion of the thesis and future prospect has been presented.

ZIEHL-NEELSEN SPUTUM SMEAR MICROSCOPY IMAGE DATABASE (ZNSM-IDB): A RESOURCE TO FACILITATE AUTOMATED BACILLI DETECTION FOR TUBERCULOSIS DIAGNOSIS

Summary

Ziehl-Neelsen stained sputum smear microscopy is the most widely used test for tuberculosis diagnosis, but its success rate is limited. The world health organization (WHO) recommends the observation of 100-300 view-fields to improve the sensitivity, but only a few view-fields are examined due to the higher patient load. Therefore, automated screening of sputum smear sample through automated capturing of focused image (autofocusing), stitching of multiple view-fields to form mosaic (autostitching), and automatic bacilli segmentation (grading) is required to significantly improve the sensitivity and reduce the computation time. Nevertheless, unavailability of a unified database hindered the development of automated screening algorithms on these three domains. Therefore, Ziehl-Neelsen Sputum smear Microscopy image Database (ZNSM-iDB) has been developed and freely accessible at http://14.139.240.55/znsm. The seven categories of diverse datasets acquired from three different bright-field microscopes are included in this database. Autofocusing, autostitching and manually segmented bacilli datasets can be used for developing algorithms, while remaining four datasets can be used to improve the sensitivity and specificity of segmentation methods. The datasets were validated using different automated algorithms of autofocusing, autostitching and bacilli segmentation. This unified referral resource can also be used for the validation of robust algorithms as images available in this database have diverse imaging content with high noise and artifacts. The ZNSM-iDB may assists for the development of automated microscopy.

2.1. Introduction

Tuberculosis, alongside the human immunodeficiency virus (HIV) infection, is the primary cause of death from a single infectious agent [27]. Early and accurate diagnosis of tuberculosis is crucial to achieve better health outcomes [139]. Sputum smear microscopy is the widely used test and considered as a key factor in misdiagnosis of this disease, mainly in underdeveloped and developing countries [140]. This test is mainly performed using fluorescence microscopy (FM) or bright-field microscopy/conventional microscopy (CM). The latter is the most preferred and available test in low and middle-income countries due to its cost-effectiveness, minimal bio-safety standard and handling [120, 131]. CM is also used as the primary technique for tuberculosis screening in remote areas with limited resources [120, 131] .

The WHO guidelines emphasize that 100-300 view-fields of a CM smear should be observed within twenty-four hour of collection of sputum sample for efficient diagnosis [141]. It takes 40 minutes to 3 hours to analyze even 40-100 view-field images from a single slide as manual identification and counting of bacilli using CM is very time consuming and labor intensive task [116]. Therefore, the sensitivity of tuberculosis diagnosis depends on the experience and expertise of microbiologists, and it may compromise [97]. The effectiveness of diagnosis is largely comprised for extra-pulmonary, pediatric or HIV-patients co-infected tuberculosis due to the less bacterial load in sputum samples [117]. All of these issues can be overcome through an automated microscope, which will not only improve the accuracy but also faster the diagnostic process [28, 142]. Several methods were proposed to improve the sensitivity of this test by incorporating automated methods [113, 129], but the success rate is limited mainly due to the scantiness of data, and performance variation of automated methods on different image contents [100].

The automated microscopy for tuberculosis bacilli screening requires efficient algorithms in following domains:
(i) Autofocusing: An image with the best average focus over entire view-field is defined as the focused one in a stack of images captured from a single view-field with different focus points. The maximum value of the focus measure function (FMF) corresponds to the best-focused image, and value decreases as defocusing increases [28]. Algorithms from this domain would facilitate automated capturing of the best-focused image. Several autofocusing

algorithms have been proposed and implemented on microscopy images for diverse biological applications [28, 93, 98].

(ii) *Autostitching*: This method stitches multiple adjacent overlapping view-fields of a smear-slide to form a slide map or mosaic. Observation of 300 view-fields can be performed faster and efficiently by automated stitching of view-fields followed by detection of bacilli in a stitched-image by segmentation methods [107]. Bacilli segmentation algorithms use shape and size of tuberculosis bacilli as the potential features to segment the bacilli from other objects [113, 120]. Therefore, Autostitching also facilitates automatic detection of bacilli on the boundaries by joining half bacillus structures on the edges of different view-fields. Though several autostitching algorithms were developed [106, 107, 110, 111], they were not evaluated on diverse datasets.

(iii) *Automatic bacilli segmentation and grading*: It is a process of segmentation of bacilli either from view-field or mosaic, and classifying the image as TB positive or negative. Several techniques have been used to segment and classify the bacilli in images [59, 113, 116, 120, 130, 131], but these are not validated on a unified and diverse imaging datasets.

The better diagnosis of cancer and other diseases were already assisted through databases and automated tools development [59, 143]. Databases were used to validate the algorithms/methods of computer aided diagnosis (CAD) systems which provide the second opinion about a disease [144-146]. The databases and CADs are also facilitated the early diagnosis of diseases by accelerating the process. Keeping in view of these accomplishments of unified databases, the Ziehl-Neelsen Sputum smears Microscopy image Database (ZNSM-iDB) has been developed (http://14.139.240.55/znsm). ZNSM-iDB contains diverse categories of image datasets with different imaging contents and medium to high density backgrounds. It provides datasets for all three processes required for automated microscope development. Standard laboratory protocols were used to capture the images [141], and the datasets were also validated by algorithms to establish their robustness. This database can be used to develop and validate efficient and robust algorithms related to automated microscopy.

2. Material and methods

2.2.1. Data Collection

In total, 10 ZN-stained sputum smear slides of TB-positive patients were used to acquire the digital images of view-fields under the supervision of two microscopists. Three different microscopes were used to acquire the triplicate data for each category (Table 2.1 & Section

2.2.1 – 2.2.7). The objective lens with 100x magnification was used to capture the *Mycobacterium tuberculosis* (width and length are about 0.5µm and 2-4µm, respectively) . Images are in RGB (red, green and blue) color space with ".jpg" file-format. Detailed configurations of all the microscopes and acquired image properties are mentioned below:

(i)   Labomed Digi 3 digital microscope (MS-1) was used to acquire first datasets, which features Lx400 trinocular and an iVu 5100 digital camera with 5.0 megapixel CMOS sensor. The dimension, bit depth and resolution of acquired images were 800x600 pixels, 24 (eight per channel) and 120 DPI, respectively. The pixel pitch of each pixel is 2.2µm.

(ii)   Motic BA210 digital microscope (MS-2) was used to acquire second datasets, which features Siedentopf type Binocular head and Moticam 2500 digital camera with 5.0 megapixel CMOS sensor. The dimensions of acquired images were 1280x1024 and 2592x1944 pixels. Bit depth and resolution of each image were 24 and 96 DPI, respectively. The pixel pitch of each pixel is 2.2µm.

(iii)   Olympus CH20i digital microscope (MS-3) was used to acquire third datasets, which features trinocular and digital camera of Smartphone with 16-megapixel BSI-CMOS sensor. The Smartphone was attached to the microscope using microscope mobile phone interface. The dimensions of acquired images were 5312x2988 (16MP), 3984x2988(12MP) and 2048x1152(2.4MP) pixels with bit depth of 24 and resolution of 72 DPI. The physical size (pixel pitch) of a pixel is 1.12µm.

2.2.2. Smartphone Camera-enabled Microscope

The images from 3rd microscope were acquired using smartphone camera (Fig. 2.1). This setup for capturing digital microscopy images is very inexpensive as a smartphone camera was attached to the old microscope. Laboratories in remote areas of developing countries have very limited resource and generally digital microscopes are not available. Therefore, the basic bright-field microscope can be used to capture the digital images using smarpthone camera. These dataset will help research community to develop and validate automated microscopy algorithms for inexpensive digital microscope facility. Smartphone-based disease diagnosis has potential to be used in remote areas of TB-endemic countries where Smartphone is available extensively [88]. Additionally, the advantage of using Smartphone camera is that it can simultaneously be used for automatic bacilli detection using image processing methods, and maintaining electronic health records [88].
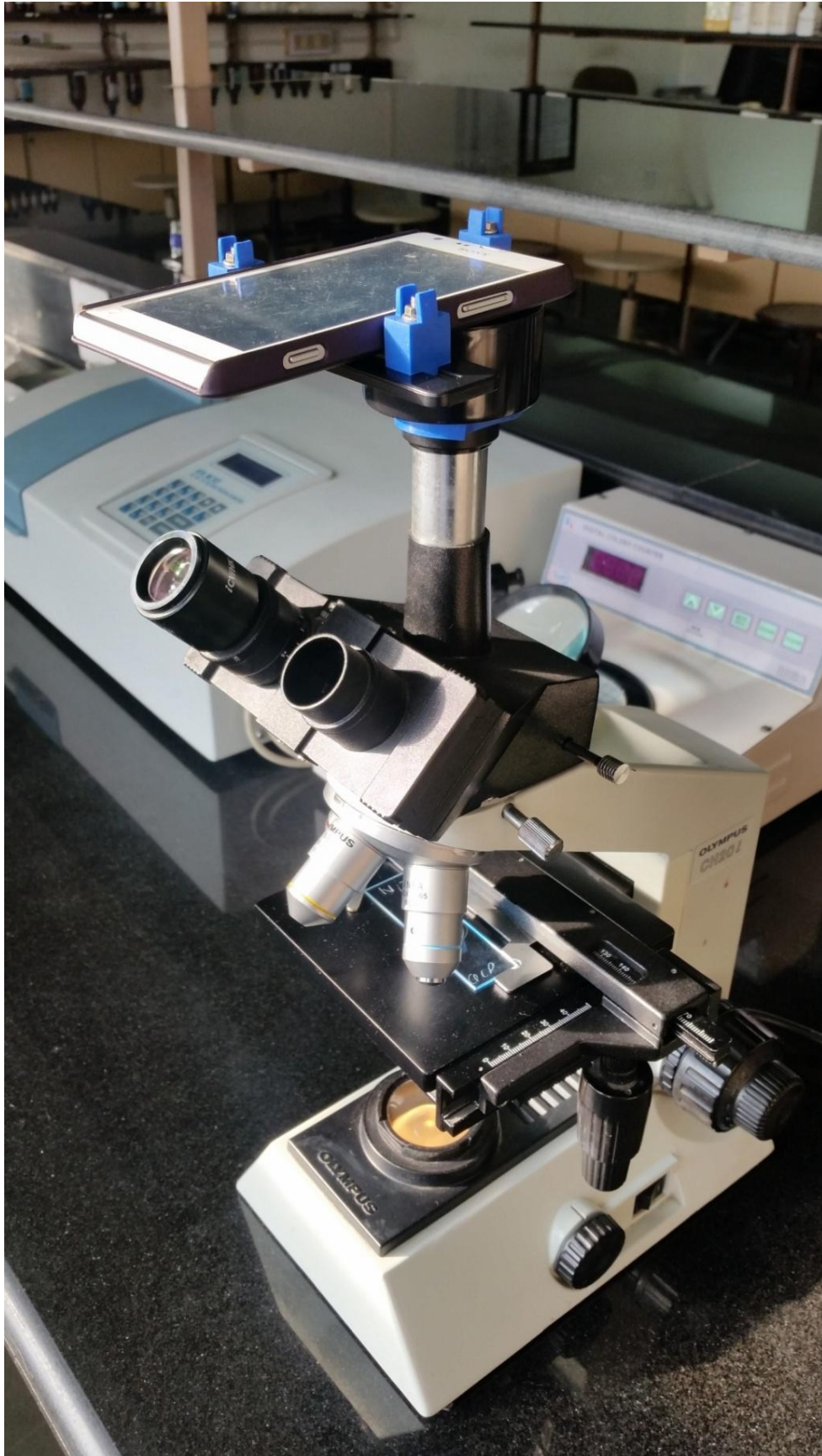
Fig. 2.1 Smartphone camera enabled microscope

2.2.3. Description of Datasets

The architecture and application of ZNSM-iDB is described in Fig.2.2. The ZNSM-iDB contains digital images in triplicates (one set from each microscope) for each of seven categories, which can be downloaded on local disk or visualize online for further processing and applications (Table 2.1). Multiple and diverse datasets in term of image contents were provided to develop the robust algorithms for automated microscopy.
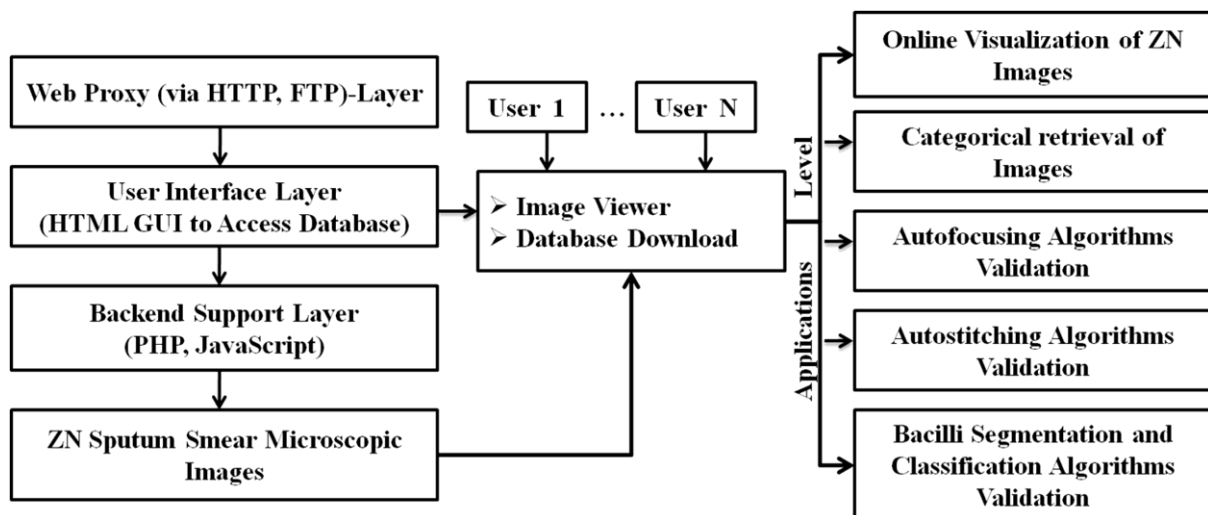
Fig. 2.2 Architecture and applications of ZNSM-iDB

Table 2.1 Category-wise presentation of datasets available in ZNSM-iDB

Group	Category of Data	No. of digital images from different Microscope (MS)		
		MS-1	MS-2	MS-3
1.	Autofocusing dataset*	9 stacks	10 stacks	30 stacks
2.	Overlapping view-fields for autostitching	7 Sets (50 to 90 Images/Set)	6 Sets (50 Images/ Set)	10 Sets (50 Images/Set)
3.	Manually segmented bacilli in a view-field	2 Sets (50 Images/Set)	2 Sets (50 Images/Set)	2 Sets (50 Images/Set)
4.	View-fields without bacilli	50	50	50
5.	Single or few bacilli	100	100	100
6.	Overlapping (occluded) bacilli	200	200	200
7.	Over-stained view-fields with bacilli and artifacts	250	250	250

* Each stack contains 20 images.

Detailed description for each category of data is given below:

(i) Autofocusing dataset

Every stack in this category contain at least 20 images captured at different focus point from a single view-field in which one is marked as focused one, while the others are defocused images to different extents. These images were taken in sequential manner for a given view-field from unfocused to focused and again unfocused. Mostly, The 10th image is the best focused one in each stack.

(ii) Overlapping view-fields for auto-stitching

Adjacent overlapping view-fields images can be stitched to make the slide map or mosaic using image processing methods. In this dataset, ten overlapping view-field images were acquired in a row and then the slide was moved left or right to take the images of next row (Fig. 2.3). Every row was also overlapped with its adjacent row.
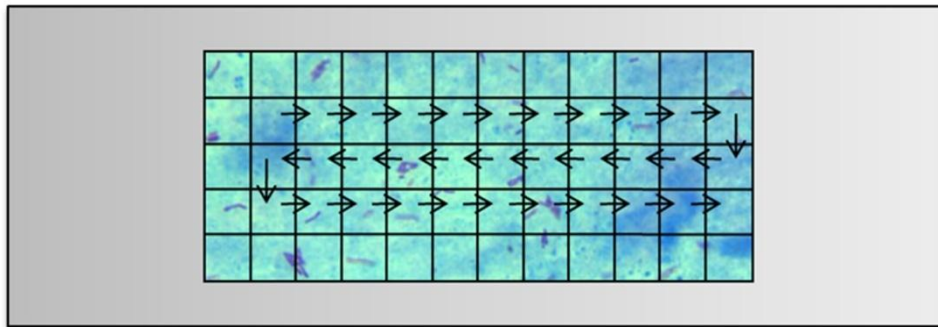
Fig. 2.3 A depiction of direction in which the images were acquired from a ZN-stained slide. Each square box corresponds to a view-field

(iii) Manually segmented bacilli in a view-field

View-fields images in this datasets were manually segmented or marked for bacilli and artifacts. Different shapes such as a circle or oval shape for single bacillus, square or rectangle for occluded bacilli, diamond for unclassified red structures and hexagon for the artifacts were used for marking (Fig. 2.4a).

(iv)View-fields without bacilli

Images in this group range from medium to very high-density background due to over-staining and artifacts, but view-fields images are bacilli negative (Fig. 2.4b).

(v) View-fields with a single or few bacilli

In this dataset, the number of bacilli in each view-field image varies from 1 to 10. This group also has medium to high-density backgrounds due to overstraining patches and artifacts (Fig. 2.4c).

(vi)View-fields with overlapping (occluded) bacilli

Several times, two or more tuberculosis bacilli are overlapped at the same position and form an occluded bacilli cluster. Generally, segmentation methods are unable to segment these bacilli effectively. Images in this category are diverse in terms of high and medium density backgrounds. The former images are noisy and over-stained, and bacilli are not clearly visible, while the bacilli are clearly visible in low density background images (Fig. 2.4d).

(vii) Over-stained view-fields with bacilli and artifacts

The overstaining during slide preparation and artifacts leads to the poor quality of ZN-stained CM images. Therefore, the bacilli detection in this slide is difficult using automatic segmentation method, and only robust methods can attain better success rate. In this group, >200 images from each microscope are included that posses over-stained (blue) regions with artifacts and/or bacilli (Fig. 2.4e).

2.2.3. Data Validation

ZNSM-iDB contains image datasets for autofocusing, autostitching, and bacilli segmentation and classification. Algorithms/methods reported in these three domains were also implemented on the datasets to validate the datasets.

In total, Twenty-four focus measure functions (FMFs) widely used in different application were implemented on autofocusing datasets to determine the best-focused image in each stack. Accuracy, focus error, false maximum and full width at half maximum were used to evaluate the performance of FMFs in classifying a stack. Various preprocessing steps (e.g. median filtering, noise addition, contrast reduction, saturation increment and non-uniform illumination addition) were also applied to check the robustness of FMFs to the different imaging conditions (see Chapter 3 for detail).

Autostitching was performed on the overlapping view-fields datasets of ZNSM-iDB and reported in other study [128]. The overlapping view-fields were stitched together using feature extraction and selection techniques called scale-invariant feature transform (SIFT) and random-sample-consensus (RANSAC), respectively. Images were converted to grayscale prior to feature extraction. SIFT features are present at scale space maxima or minima of a difference of Gaussian (DoG) function. These features are invariant to rotation and scale changes; therefore, they perform better on images with varying illumination and orientation as [128]. After feature extraction, RANSAC separate inliers (point of interest) from outliers.

This method remove the wrongly mapped points coming due to inaccuracies of the SIFT method. Finally, filtered features set were used to stitch the view-fields images. The faster stitching and mosaic formation were achieved using divide-and-conquer algorithm as linear stitching of is computationally intensive. Furthermore, the final stitched image were
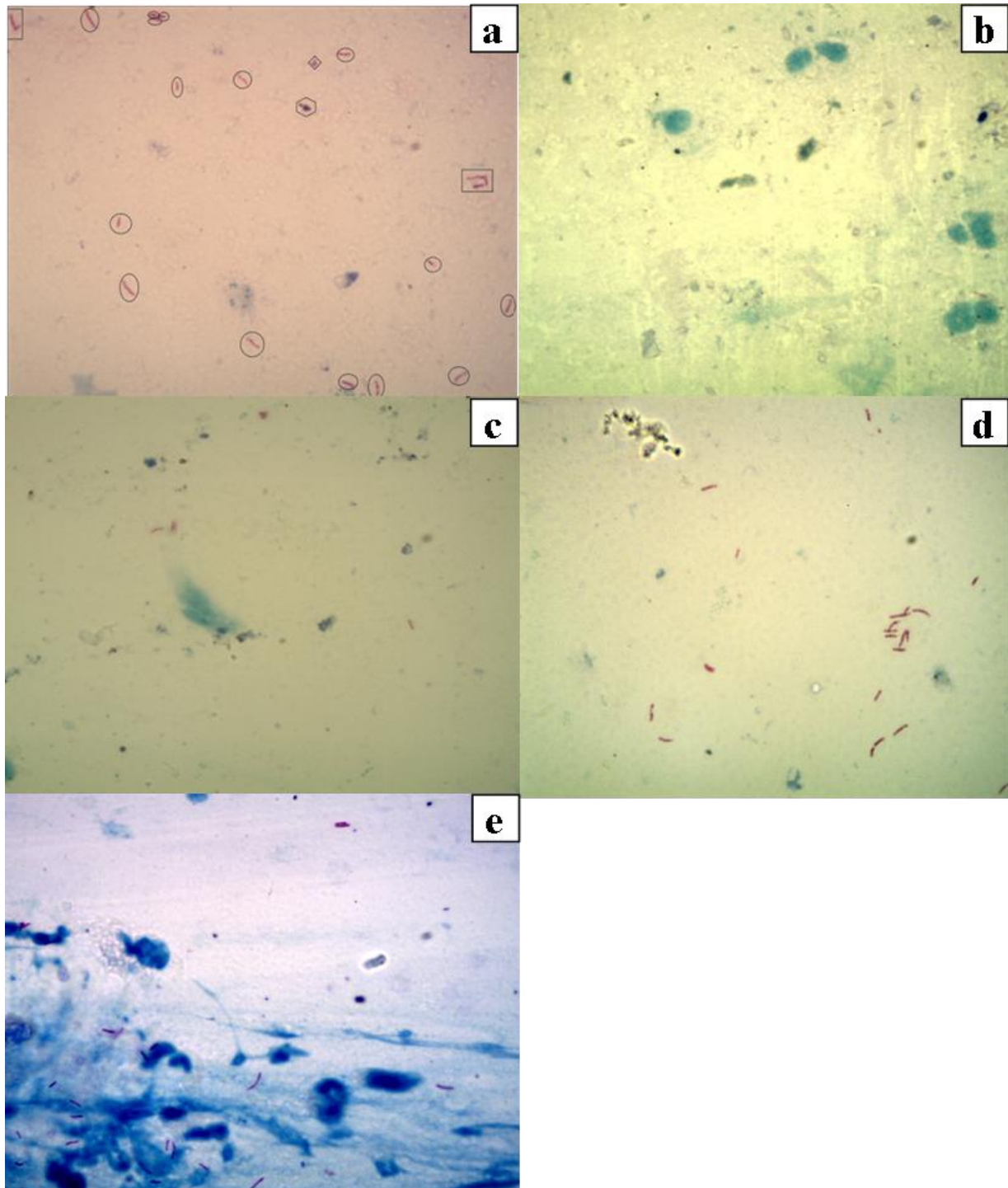
Fig. 2.4 Sample images of five different category datasets available in ZNSM-iDB. (a) Manually segmented view-field, (b) View-field without bacilli, (c) View-field with single or few bacilli, (d) View-field with occluded bacilli, and (e) Over-stained view-fields with bacilli and artifacts

to the original image using various similarity measures such as Correlation (COR), structural similarity (SSIM) and feature similarity (FSIM).

Watershed algorithm [147] was used for bacilli segmentation and classification on ZNSM-iDB database. In total, forty images were randomly extracted and grouped into medium- and high-density background datasets to check the performance in both the cases. Shape and size of the objects were used to filter the true bacilli. Similarly, the watershed algorithm was implemented separately on Smartphone enabled microscope (MS-3). In total, thirty images were randomly extracted from MS-3 datasets. The sensitivity and specificity of the segmentation method were calculated in both the studies. Furthermore, images from ZNSM-iDB were divided into four groups based on tuberculosis infection level or number of bacilli (Table 2.2) [148], and sensitivity and specificity of watershed segmentation method for classifying a view-field image as TB-positive or negative were determined for each group. Sensitivity and precision rate of this segmentation method for identifying true bacilli were also calculated. Furthermore, to evaluate the percent of pairs where the observation with TB-positive has a lower predicted probability than TB-negative, discordance rate was calculated for watershed segmentation method [149, 150]. Binary logistic regression model was used to calculate predicted probability [150]. Detailed analysis is presented in Chapter 5 of the thesis.

Table 2.2 Grading of view-fields on the basis of infection level.

Number of Bacilli	Number of View-Fields to be Examined	Grading
1-9 in 100 view-fields	100	Scanty[a]
10-99 in 100 view-fields	100	1+
1-10 in each view-field	50	2+
>10 in each view-field	20	3+

[a]Report exact number of bacilli present in the view-fields

2.3. Results and discussion

2.3.1. Applications of the data resource

Low- and middle-income countries contribute to around 95% TB cases and 98% deaths, and these poverty-stricken countries rely on sputum smear microscopy for the detection of disease [115]. The sensitivity of this test is poor due to time constraints and the high volume of patients. The performance is also grossly compromised when sputum sample contains *M. tuberculosis* bacterial load less than 10,000 bacilli/ml. The objective of developing ZN

sputum smear microscopy image database (ZNSM-iDB) is to provide a unified image resource that has the potential to facilitate the development of novel algorithms and tools related to automated grading (computer aided detection of bacilli) using image processing techniques. The database is available at *http://14.139.240.55/znsm* and contains seven different diverse datasets (Table 2.1). Users have opportunities to access the data online (Fig. 2.5) or download it through "Download" link (Fig. 2.5c). A tutorial is provided to assist the user with exploring this database. For conventional bright field microscopy (CM), the smear slides are prepared using either Kinyoun cold (KC) or Ziehl-Neelsen (ZN) staining. Though a Kinyoun-stained specimen images are provided for autofocusing and segmented bacilli view-field, bacilli in these images are less visible than those in ZN-stained images [138]. Most of the TB affected countries use ZN-staining instead of Kinyoun as it has low sensitivity [151]. Major usage and applications of the database in automated microscopy is provided in Fig. 2.6.

Manual screening of TB smears is a time consuming process and a microscopist needs to analyze 100-300 view-fields for accurate diagnosis [152]. The time required to analyzing one case varies from 40 minutes to 4 hours, depending on severity of infection [129]. As most of the TB diagnosis centers have high patient load, false negative rates resulting in poor sensitivity is the stark reality [116]. Sensitivity of the CM varies from 0.32 to 0.94, whereas for fluorescence microscopy it varies from 0.52 to 0.97 [153]. The specificity is approximately similar in both microscopes ranges from 0.94 to 1.0 [153]. Automation of microscopy to analyze view-field has the potential to overcome the variation of sensitivity arising from manual screening. Sensitivity and accuracy were found to be improved significantly by increasing the number of view-fields to be analyzed using automated (bacilli detection) methods [113].
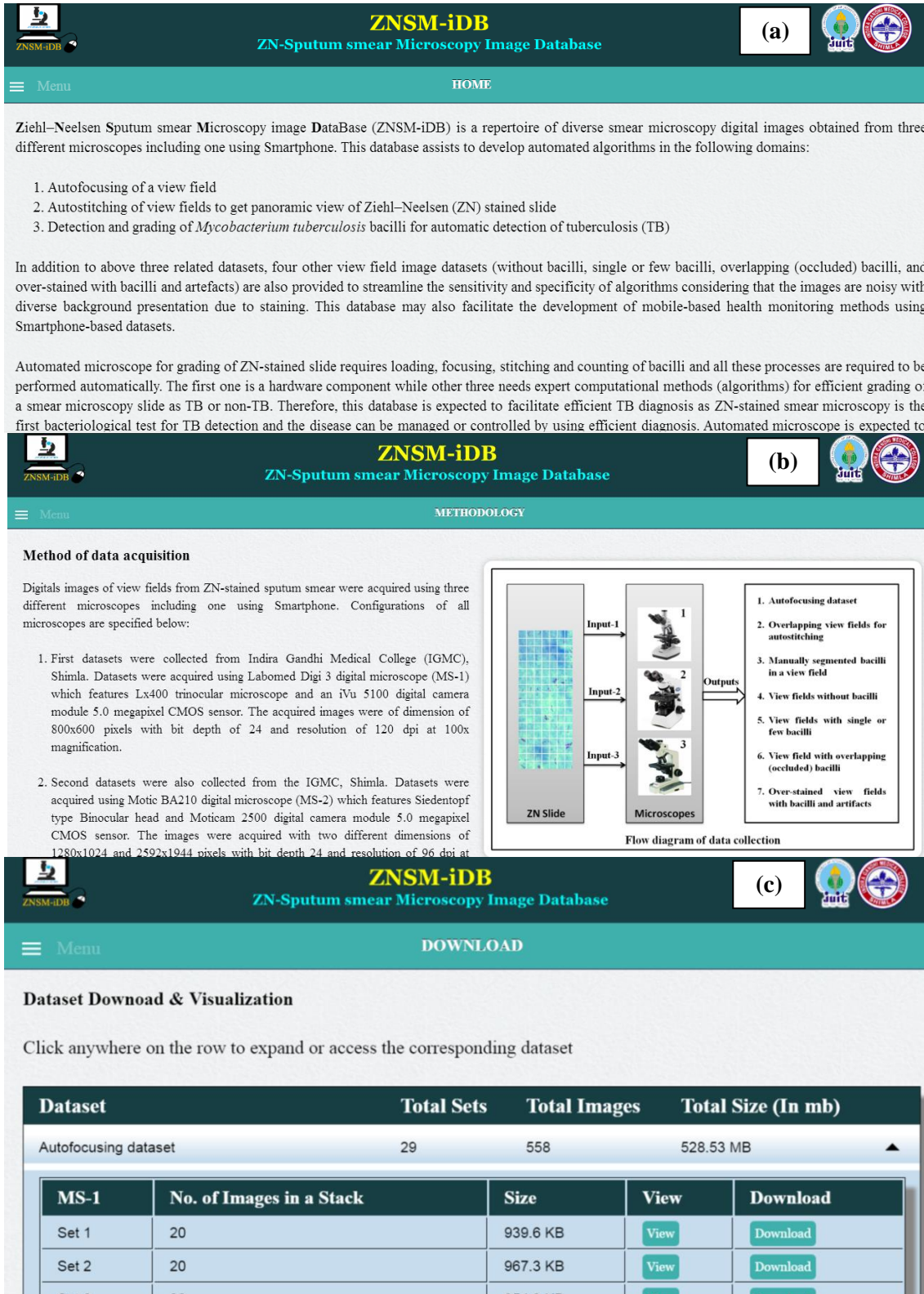
Fig. 2.5 Screenshots of ZNSM-iDB. (a) Home page, (b) Methodology page, and (c) Image visualization and data download page
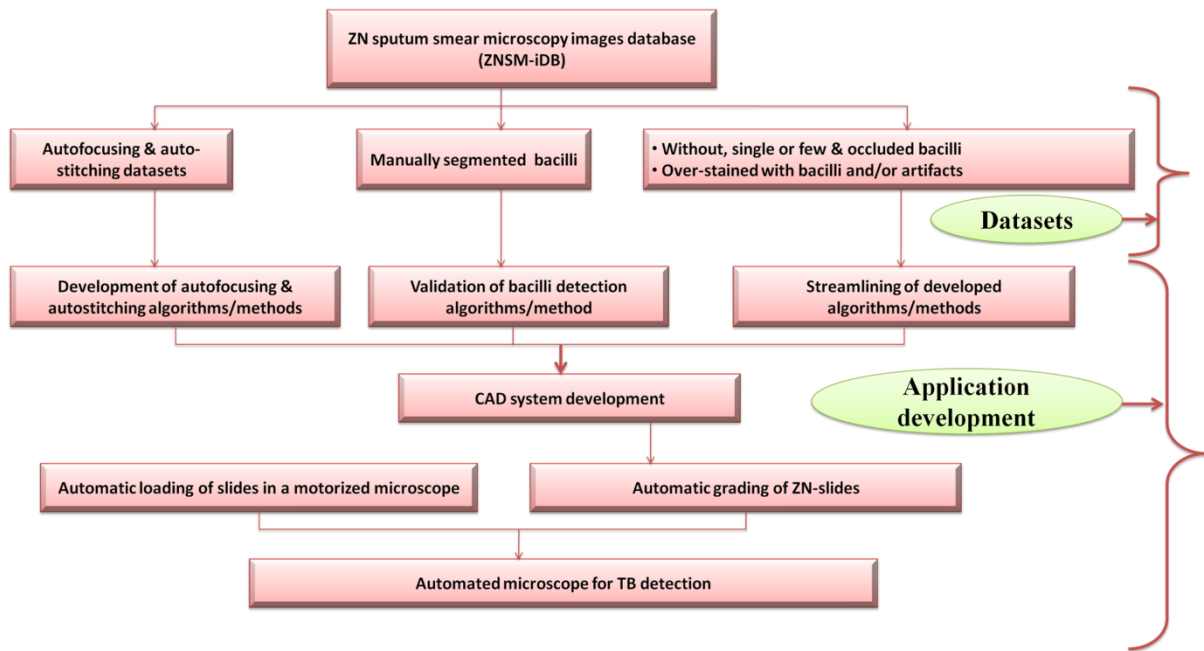
Fig. 2.6 Application of ZNSM-iDB database in automated microscopy

Autofocusing and autostitching datasets (Group 1 & 2) have been provided to complete the first two steps of automated microscopy. Though many autofocusing methods have been proposed [93, 98], the best method remains task-dependent [104]. According to WHO guideline, 300 view-fields should be analyzed before grading a smear as TB-negative [152]. This can be achieved faster and efficiently by automated stitching of overlapping view-fields to make a mosaic (virtual slide map), and number of bacilli may be determined by segmentation methods [107]. Autostitching also facilitates automatics detection of bacilli on the edge by joining half bacillus structures on the edges of two different view-fields. Datasets from different microscopes including Smartphone have been provided to evaluate available methods as well as development of more robust algorithms. Manually segmented view-fields (Group 3) can be used as a reference standard for the development and validation of bacilli grading algorithms.

The remaining four categories (Group 4, 5, 6 & 7) of datasets are provided to evaluate the performance of automatic and semiautomatic bacilli detection algorithms on highly noisy images. A patient is diagnosed as TB if 1-9 acid fast bacilli per 100 fields are presented [154]. So, datasets of single or very few bacilli in view-field images (Group 5) can be used to develop an algorithm with improved sensitivity. As most of the slides are over-stained, view-fields without bacilli can be utilized to evaluate the performance of algorithm in high noise images. View-field images without bacilli but containing artifacts in over-stained slide can

also be helpful for the development of algorithm with improved specificity. Group 6, images with two or more occluded bacilli (overlapped at the same position), and group 7, over-stained view-fields with bacilli and artifacts, datasets are expected to improve sensitivity, as these overlapping bacilli are difficult to detect using automated methods. These occluded bacilli are detected as artifacts by available algorithms [116]. These two related datasets assist to develop more efficient methods that discriminate between occluded bacilli and artifacts.

Automation of disease diagnosis provides second opinion and recognized as significant factor for efficient diagnosis of complicated diseases [155]. Interstitial lung disease (ILDs) database [143] was used to develop and validate an automated system which detects different texture patterns such as emphysema, ground glass, fibrosis, micronodules and healthy with the accuracy rate of 96%, 88%, 90%, 90% and 88% respectively [155]. Similarly, lung image database consortium (LIDC) database was used for automated/semi-automated segmentation of lung nodules and achieved an accuracy rate of 79%, 80.4% and 91.7% in three different studies [145, 156, 157]. Automated lung texture analysis on HRCT was used to identify nodules related to lung cancer with a multi-classification accuracy of 76.9%. Several automatics bacilli detection methods were proposed, but none of them evaluated on same datasets [113, 116, 120, 129-131]. Lewis et al. [118] have proposed an automatic TB screening system called "TBDx" for FM images. TBDx automatically loads the slide and capture the focused image, and classifies the slide as TB positive or negative. There is no automated system (like TBDx) is available for ZN sputum smear bright-field microscope.

The ZNSM-iDB database can serve as a referral resource for the development and validation of algorithms related to autofocusing, autostitching and detection of TB bacilli using ZN sputum smear bright-field microscope. Since these methods are necessary for automated microscope development, this resource works as a standard platform to compare existing methods as well as to develop new algorithms in the above mentioned three domains of automated microscopy (Fig. 2.6). The ZNSM-iDB is well diverse in terms of image acquisition technology and content of acquired images. To ensure that the data is diverse, images were acquired from three different microscopes with different configurations and scope. The images from 3rd microscope used a Smartphone camera and these datasets can be used to check the robustness of developed algorithms related to automated microscopy. Auto-focusing and auto-stitching algorithms were successfully implemented to images obtained using a Smartphone attached to a microscope. Smartphone-based disease diagnosis is

inexpensive and has potential to be used in remote areas of TB-endemic countries where Smartphones are widely available [88]. The advantage of using Smartphone camera is that it can simultaneously be used for automatic bacilli detection using image processing methods, and maintaining electronic health record [88]. Breslauer et al. have developed an inexpensive mobile phone based clinical microscopy system with automated image analysis [88] for CM and FM images. The Diverse data available in this resource can facilitate the development of algorithms/model on one microscope, while the validation of the method is done on another microscope(s). Performance of bacilli detection algorithms also varies due to the image quality such as high and low noise backgrounds, occluded bacilli, etc. [94] So diverse datasets were included to evaluate the robustness of existing and new algorithms.

2.3.2. Validation

Automated microscopy algorithms (i.e. autofocusing, autostitching, and bacilli segmentation and classification) were implemented and validated on ZNSM-iDB datasets.

(i) Performance of focus measure functions (FMFs)

A Comprehensive analysis of twenty-four FMFs in different imaging conditions is performed to determine the best focus image in CM stacks (see Chapter 3 for details). This study provided Gaussian derivative (GDR), Tenengrad gradient (TGR), steerable filters (SFB), and Hemli and Scherer's mean (HSM) as the most robust and accurate FMFs in all three microscopes. These four FMFs were robust to different imaging conditions such as median filtering, noise addition, saturation increment, contrast reduction and non-uniform illumination addition). An earlier study also agreed on the Tenengrad method as better FMF for CM images [28]. Detail analyses of these FMFs are presented in Chapter 3.

(ii) Autostitching of view-fields

The overlapping datasets of MS-1 (Microscope-1 of ZNSM-iDB) were used to evaluate different autostitching methods. To generate a mosaic, SIFT and RANSAC methods were used for feature extraction and selection, respectively [128]. COR, SSIM and FSIM similarity scores between the stitched and original images were 0.997, 0.988 and 0.98, respectively. These outcomes were considerably better than the Autostitch [106] and MicroMos [108] software (Fig. 2.7).
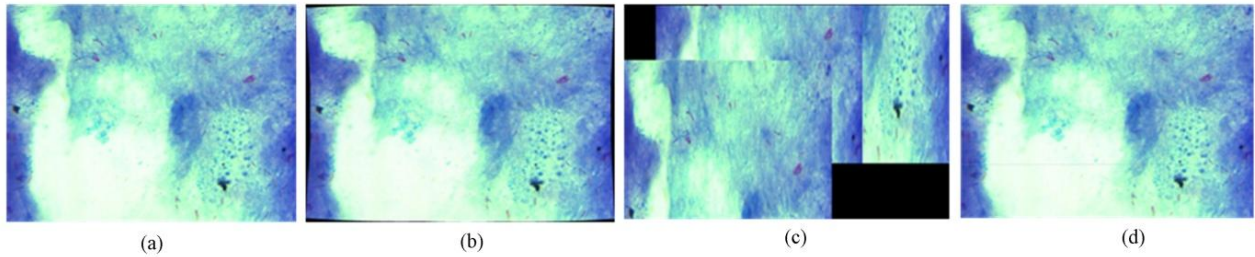
Fig. 2.7 Comparison between images of original view field with stitched mosaic. (a) Original image, (b) mosaic formed using Autostitch, (c) MicroMos and (d) divide-and-conquer.

(iii) Bacilli Segmentation and Classification

The watershed segmentation method was used to segment tuberculosis bacilli from ZNSM-iDB datasets (see Chapter 5 for details). The sensitivity and specificity of 100% and 93% were achieved for medium density background images, respectively, while sensitivity remained unchanged, but specificity was reduced to 72% in the high-density background images due to over-staining and artifacts. Likewise, the sensitivity and specificity of 93.3% and 87% were achieved for classifying a Smartphone enabled microscopic images (medium to high-density background), respectively. Performance of watershed method on different infection level was also evaluated and presented in Chapter 5 of the thesis.

2.4. Conclusion

The ZNSM-iDB is a unified and well diverse in terms of imaging contents and acquisition technology. Three microscopes with different configurations and scope were used to acquire images. This repository may facilitate a standard platform to compare existing algrithms as well as to develop new ones for automated microscopy (*i.e.* autofocusing, autostitching and automated grading) (Fig. 2.6). Computer-aided diagnosis (CAD) assists in better diagnosis of complicated diseases by improving sensitivity and specificity [155]. Although an established CAD system, "TBDx", is available for *mycobacterium tuberculosis* bacilli detection in FM images [118], most of low- and middle-income TB-endemic countries are using CM due to its easy handling, cost-effectiveness, accessibility and minimal bio-safety standard. Although Kinyoun-stained bright-field microscopic images are available for autofocusing and bacilli segmentation [138], it has poor sensitivity than ZN-stained images due to the poor visibility of bacilli [151].

Smartphone-based inexpensive disease diagnosis system can be develop and validated with the help fo MS-3 datasets of ZNSM-iDB, which can be used in the remote areas of TB-

endemic countries where laboratory resources are limited but Smartphones are widely available. Furthermore, Smartphone camera is also a portable computer which can be used simultaneously for automatic bacilli segmentation and grading using image processing techniques and maintaining electronic health record [88]. The ZNSM-iDB datasets were validated using autofocusing, autostitching, and bacilli segmentation and classification methods. Results of validation suggested that the datasets are robust and diverse, and can be used for the development and validation of automated microscopy. Development of algorithms/model can be performed on one microscope, while the validation of the same method can be done on another microscope(s) as resource contain diverse data from three microscopes. The ZNSM-iDB is expected to serve as a referral resource to the research groups working in the domains of automated microscopy algorithms development.

CHAPTER 3

IDENTIFICATION OF ROBUST FOCUS MEASURE FUNCTIONS FOR THE AUTOMATED CAPTURING OF FOCUSED IMAGES FROM ZIEHL-NEELSEN STAINED SPUTUM SMEAR MICROSCOPY SLIDE

Summary

Autofocusing for the capturing of the best-focused image using focus measure function (FMF) is a very important step in automated microscopy. Screening of bacilli from Ziehl-Neelsen (ZN) stained sputum smear conventional microscopy (CM) is a primary and widely used test for tuberculosis diagnosis. Generally, Performances of FMFs are sensitive to different imaging contents and noises. In this study, twenty-four FMFs were evaluated on CM's view-field images obtained from three different microscopes. In total, seven FMFs have shown the accuracy rate of >90% in determining the best focused image from a stack. Performance of each FMF was evaluated by assigning overall score and rank using three criteria namely, accuracy, focus error and false maxima. Robustness of every FMF was also checked in different imaging conditions (noise, contrast, saturation illumination, etc.). Gaussian derivative, steerable filters, Tenengrad, and Hemli and Scherer's FMFs were identified as the most robust and accurate functions with the accuracy >90%, and minimal focus error and false maxima. Rate of convergence to the best focus point was identified by computing full width at half maximum. These four FMFs can be used for the autofocusing of ZN-stained sputum smear CM images. Gaussian derivative FMF is effective in both CM and fluorescence microscopes.

3.1. Introduction

It is described in Chapter 2 that the manual screening of tuberculosis bacilli may misdiagnose 33 to 50% of active cases [29] due to patient load at the hospital [28, 116, 117]. Therefore, the increase in sensitivity of popular, cost-effective and non-invasive smear microscopy (CM) test can bring better health outcomes against tuberculosis. Incorporation of automated methods can improve the sensitivity and specificity of this test by examining a large number of view-fields for tuberculosis bacilli screening [89]. Automation prevents physical and mental fatigue, and faster the process of view-fields analysis [28]. Additionally, it allows sharing and storing of the images for future analysis. Autofocusing, auto-stitching, and bacilli segmentation and grading are the three sequential steps in automated microscopy for the tuberculosis diagnosis. Autofocusing of a view-field is very crucial in any automated microscopy as subsequent steps (autostitching and bacilli segmentation) rely on it [28].

An image with the best average focus over entire view-field is the focused one in a stack of images captured with different focus points. Focus measure function produces maximum value at best focus point and value decreases as defocusing increase [97]. Several FMFs were implemented on the commercial cameras and synthetically generated image sequences, and the Laplacian- and statistical-based FMFs were performed better [100]. Thirteen FMFs were evaluated on FM smear images where mid-frequency discrete cosine transform (96.67%), Vollath's autocorrelation (89%) and Tenengrad (89%) methods were efficient [98]. Costa et al., [94] had employed nine FMFs on Kinyoun stained sputum smear images which have lower sensitivity rate than CM images[151]. Osibote et al., [28] and Russell et al., [102] had separately evaluated six (GNV, BGR, MLP, ELP, VCR and TGR) and three (ELP, GDR and Variance of the log-histogram) FMFs on CM images, respectively. VCR and BGR were reported as the best FMFs in the former study, while ELP was the best in the latter study. These studies did not narrow down to a single or few FMFs for in CM images, and produced different outcomes. It is also noted that FMFs performed significantly better in fluorescence microscopy images [103, 158, 159], but produced average outcomes in CM images. Though several FMFs are available for auto-focusing, their performances are largely dependent on the image contents and instrument [29, 97, 98, 102, 160].

The performances of FMFs also vary due the background of an image which categorized as the lower, medium and higher density [93, 102]. Background of CM images have higher density than FM. Additionally, overstaining through ZN dye make focusing more challenging as FMFs consider these regions as significant factor for identifying the best-focused image.

These images also distinctive due to their shape, size, artifacts and debris which make autofocusing even more challenging [28]. In this study, 24 FMFs were selected on the basis of their performance in different auto-focusing applications. These FMFs were evaluated on diverse datasets from three different microscopes (Chapter 2) to identify efficient FMFs for CM images. These FMFs are grouped into five different categories based on their working principles. Robustness of FMFs was also checked after incorporation of median filtering and image distortion namely, noise addition, contrast reduction, saturation increment and uneven illumination. Comparisons of FMFS with earlier studies were also performed for better interpretation.

3.2. Material and Methods

In total, 31 autofocusing stacks were extracted from Ziehl-Neelsen Sputum smear Microscopy image Database (ZNSM-iDB) accessible at http://14.139.240.55/znsm/ (Chapter 2). Sputum smear slide of 10 TB-positive patients were used to acquire the images from three different microscopes. Each stack contains twenty view-field images captured at different focus points (Fig. 3.1). These images were diverse and ranges from medium density to high density background. Image contents vary due to the over-staining, under-staining and artifacts. Configuration of microscope and properties of images are described in detail in Chapter 2.

3.2.1 Focus Measure Functions

A wide range of FMFs was evaluated in this study to identify the best-focused image from a stack CM images. In total 24 most commonly used FMFs in various autofocusing applications have been implemented in this study. Value of an ideal FMF is maximum at the best focus position, and it decrease as defocusing. This function produces a Gaussian or bell-shaped curve when focus measure values are plotted against image series with different focus points (Fig. 3.2). The FMFs which have not produced the bell shape like curve were excluded in the first step of study as it is a preliminary criterion for a good FMF. The MATLAB is used to implement the FMFs from five major categories. Mean execution time of each focus measure function was calculated by Intel® Core™ i3-3220 CPU at 3.30 GHz with 8 GB RAM. Detail description of every category and function is presented below.
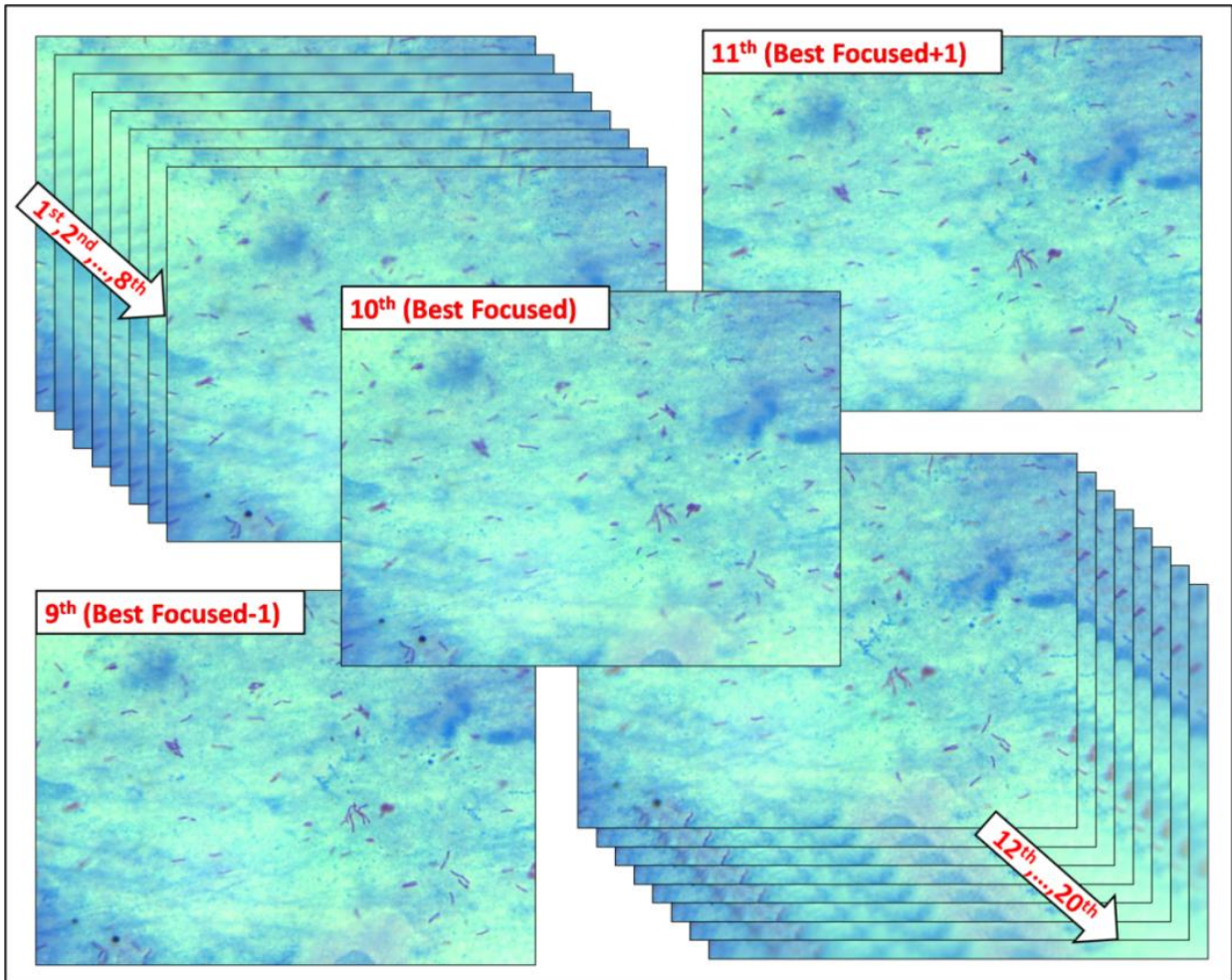
Fig. 3.1 A stack of 20 images were acquired on different focus distances. 10th image is the best focused while defocusing increases toward both ends (9th to 1st and 11th to 20th)
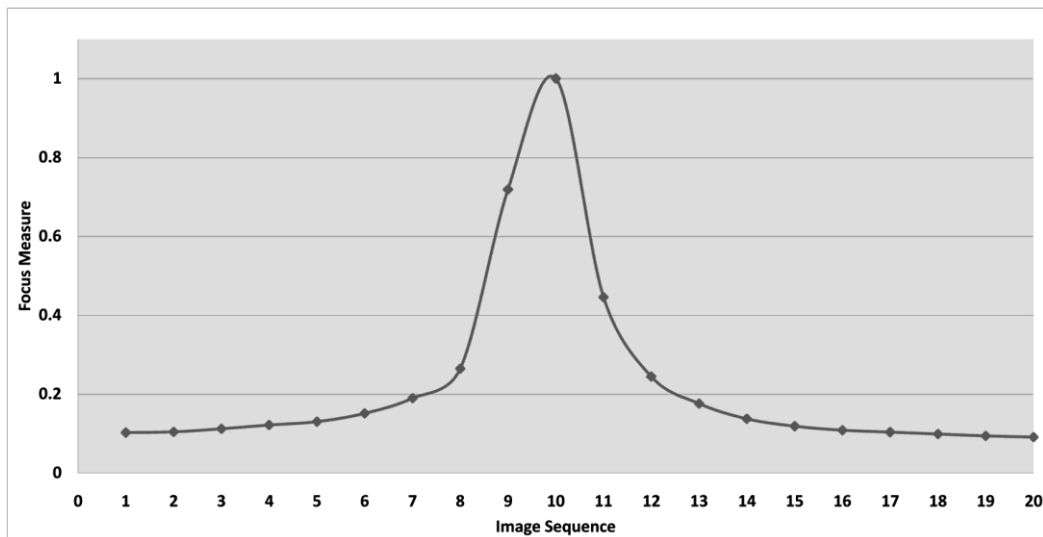
Fig. 3.2 A typical bell-shaped curve produced by a focus measure function (FMF). X-axis represents sequence of images acquired at different focus distances and Y-axis represents FMF value determined using Gaussian derivative method. In the data, tenth image of the stack is the best focused one.

(i). Gradient-based FMFs: These functions assume that well-focused image has more high-frequency content. Therefore, the large intensity difference between neighboring pixels leads to sharper edges. The higher gradient represents more sharp edges, hence these FMFs use the gradient or first order derivative of the image to find well-focused one.

(a). Brenner gradient (BGR) [161]: This focus measure computes the difference between two neighboring pixels with horizontal or vertical distance of two.

$$F_{BGR} = \sum_{(i,j)} |I(i,j) - I(i+2j)|^2 \tag{1}$$

$$\text{Where } |I(i,j) - I(i+2j)|^2 \geq \theta \tag{2}$$

(b). Energy gradient (EGR) [162]: The sum of squares of the first derivative in the x and y directions can be used as a focus measure

$$F_{EGR} = \sum_{(i,j) \in \Omega(x,y)} I_x(i,j)^2 + I_y(i,j)^2, \tag{3}$$

(c). Gaussian derivative (GDR): Geusebroek et al. used first order Gaussian derivative to compute the focus measure [91].

$$F_{GDR} = \sum_{(x,y)} (I * \Gamma_x)^2 + \left(I * \Gamma_y\right)^2, \tag{4}$$

Where Γ_x and Γ_y are the x and y partial derivatives of the Gaussian function $\Gamma(x, y, \sigma)$ respectively.

$$\Gamma(x, y, \sigma) = \frac{1}{2\pi\sigma^2} \exp\left(-\frac{x^2 + y^2}{2\sigma^2}\right) \tag{5}$$

In this study, the value of σ was selected such that total five $\sigma's$ were contained along W for the neighborhood of $W \times W$ size.

(d). Thresholded absolute gradient (THR) [100]: The first derivative of the image in horizontal dimension is used as a focus measure

$$F_{TGR} = \sum_{(i,j) \in \Omega(x,y)} |I_x(i,j)|, \qquad |I_x(i,j)| \geq T \tag{6}$$

This method is modified according to where maximum of vertical and horizontal image derivatives has been used as focus measure. For more generalized results, threshold T has not been used in this study.

(e). Squared gradient (SGR) [159]: Instead of (Eq.6), the first derivative is squared to increase the impact of larger gradient on focus measure.

$$F_{\text{SGR}} = \sum_{(i,j)\, \in\, \Omega\,(x,y)} I_x(i,j)^2 \tag{7}$$

(f). Tenengrad (TGR) [99, 159]: Magnitude of image gradient is used as focus measure. Image I is convolved with Sobel operators to obtain the image gradient.

$$F_{\text{TGR}} = \sum_{(i,j)\, \in\, I(x,y)} \left(G_x(i,j)^2 + G_y(i,j)^2\right), \tag{8}$$

Where G_x and G_y are the image gradients in x and y directions respectively.

(g). Tenengrad variance(VGR) [99]: Variance of the image gradient is used as a focus measure.

$$F_{\text{VGR}} = \sum_{(i,j)\, \in\, I\,(x,y)} \left(G(i,j) - \overline{G}\right)^2, \tag{9}$$

Where $\overline{G}$ is the mean gradient magnitude and computed as: $G = \sqrt{G_x^2 + G_y^2}$

(ii). Laplacian-based FMFs: These functions also measure the amount of sharp edges in images but use the second-order of derivatives or Laplacian.

(a). Energy of Laplacian (ELP) [102]: The image is convolved with Laplacian mask to compute the second derivative ΔI. Sum of the square of the image Laplacian is used as focus measure.

$$F_{\text{ELP}} = \sum_{(i,j)\, \in\, \Omega\,(x,y)} \Delta I(i,j)^2, \tag{10}$$

(b). Modified Laplacian (MLP) [163]: Nayar & Nakagawa proposed a new focus measure based on modified Laplacian $\Delta_m I$ of image I.

$$F_{\text{MLP}} = \sum_{(i,j)\, \in\, \Omega\,(x,y)} \Delta_m I(i,j), \tag{11}$$

Where,

$$\Delta_m I = |I * \mathcal{L}_X| + |I * \mathcal{L}_Y|. \tag{12}$$

The convolution masks $\mathcal{L}_X$ and $\mathcal{L}_y$ are

$$\mathcal{L}_X = [-1 \quad 2 \quad -1]$$

And $\mathcal{L}_Y = \mathcal{L}_X^T$

(c). Diagonal Laplacian (DLP) [164]: Thelen et al., have used two more Laplacian mask along with $\mathcal{L}_X$ and $\mathcal{L}_y$ defined in (Eq.12) to include vertical variations of the image *[164]*.

$$\Delta_m I = |I * \mathcal{L}_X| + |I * \mathcal{L}_Y| + |I * \mathcal{L}_{X1}| + |I * \mathcal{L}_{X2}|, \qquad (13)$$

where $\mathcal{L}_{X1}$ and $\mathcal{L}_{x2}$ are given by

$$\mathcal{L}_{X1} = \frac{1}{\sqrt{2}} \begin{bmatrix} 0 & 0 & 1 \\ 0 & -2 & 0 \\ 1 & 0 & 0 \end{bmatrix}, \qquad \mathcal{L}_{X2} = \frac{1}{\sqrt{2}} \begin{bmatrix} 1 & 0 & 0 \\ 0 & -2 & 0 \\ 0 & 0 & 1 \end{bmatrix}$$

(iii). Wavelet-based FMFs: These functions calculate the frequency and spatial contents of image using discrete wavelet transform coefficients.

(a). Sum of wavelet coefficients (SWC) [165]: Statistical properties of the discrete wavelet transform (DWT) coefficients are mostly used in wavelet-based focus measure. Firstly, Daubechies D6 wavelet filter is applied on an image than this image is further divided into four sub-images, where W_{LH1}, W_{HL1}, W_{HH1} and W_{LL1} refer to the three detail sub-bands and the coarse approximation sub-band, respectively. This information further used to calculate focus measure.

Yang and Nelson sums the absolute values in the W_{LH1}, W_{HL1}, W_{HH1} and W_{LL1} detail sub-band to compute focus measure *[165]*

$$F_{\text{SWC}} = \sum_{(i,j) \in I(x,y)} |W_{LH1}(i,j)| + |W_{HL1}(i,j)| \qquad (14)$$
$$+ |W_{HH1}(i,j)|,$$

(b). Variance of wavelet coefficients (VWC) [165]: This algorithm sums the variances of the wavelet coefficients to compute the focus measure.

$$F_{\text{VWC}} = \sum_{(i,j) \in \Omega_D} |W_{LH1}(i,j) - \mu LH1| + |W_{HL1}(i,j) - \mu HL1| \qquad (15)$$
$$+ |W_{HH1}(i,j) - \mu LL1|,$$

where μLH, μHL and μLL represent the mean values calculated in the respective detail sub-bands.

(c). Ratio of the wavelet coefficient (RWC) [166]: In this algorithm, the ratio between high frequency coefficients M_H and the low frequency coefficients M_L of the wavelet transform is used to compute focus measure *[166]*.

$$F_{\text{RWC}} = \frac{M_H^2}{M_L^2}, \tag{16}$$

where M_H and M_L are

$$M_H^2 = \sum_k \sum_{(i,j) \in \Omega_D} W_{LHk}(i,j)^2 + W_{HLk}(i,j)^2 + W_{HHk}(i,j)^2 \tag{17}$$

$$M_L^2 = \sum_k \sum_{(i,j) \in \Omega_D} W_{LLk}(i,j)^2. \tag{18}$$

k represent that the coefficients is calculated using k-th level wavelet. The coefficients of the first and third level DWT are used in (Eq.17) and (Eq.18) respectively.

(iv). Statistics-based FMFs: Functions in this group use various image statistics such as standard deviation, variance, autocorrelation, etc., to calculate the degree of focus of an image. In general, these functions are less sensitive to high-frequency noise as compared to derivative-based operators.

(a). Gray-level variance (GLV) [92]: Image gray-levels variance is a statistical measure which is used to compute the relative degree of focus of an image.

$$F_{\text{GLV}} = \frac{1}{xy} \sum_{(i,j) \in I(x,y)} (I(i,j) - \mu)^2, \tag{19}$$

where μ is the mean gray-level value of image $I(x,y)$.

(b). Gray-level local variance (LLV) [99]: Pech et al., proposed the local variance of gray-levels as a focus measure for autofocus of diatoms in bright-field microscopy *[99]*. Local variance of gray-levels is defined as

$$F_{\text{LLV}} = \sum_{(i,j) \in I(x,y)} \left(L_v(i,j) - \overline{L_v} \right)^2, \tag{20}$$

Where $L_v(i,j)$ is local variance of pixels within a neighborhood of $w_x \times w_y$ size with center at (i,j). $\overline{L_v}$ is the mean gray-level value of L_v.

(c). Normalized gray-level variance (GNV) [92]: Difference in image brightness among different images of same stack is compensated by mean gray-level μ of the image.

$$F_{\text{GNV}} = \frac{1}{xy\mu} \sum_{(i,j)\,\in\,\Omega\,(x,y)} (I(i,j) - \mu)^2,$$

(21)

(d). Standard deviation (SD) [94]: Image standard deviation is a statistical measure which is used to compute the relative degree of focus of an image.

$$F_{SD} = \sqrt{\frac{1}{N} \sum_{(i,j)\,\in\,\Omega\,(x,y)} (x_{ij} - \mu)^2}$$

(22)

(e). Vollath's autocorrelation (VCR) [151, 158]: Vollath's autocorrelation method for autofocus measure is based on image autocorrelation and can be given as

$$F_{\text{VCR}} = \sum_{(i,j)\,\in\,\Omega\,(x,y)} I(i,j) \cdot I(i+1,j)$$
$$- \sum_{(i,j)\,\in\,\Omega\,(x,y)} I(i,j) \cdot I(i+2,j)$$

(23)

(f). Histogram entropy (EHS) [90]: Entropy and range of the image histogram describes the higher information content of image and can be used as focus measure. Histogram entropy function is defined as

$$F_{\text{EHS}} = -\sum_{k=1}^{l} P_k \log(P_k),$$

(24)

Where P_k denotes the relative frequency of the k -th gray-level.

(g). Histogram Range (RHS) [90]: Histogram range function is defined as

$$F_{\text{RHS}} = \max(k|H > 0) - \min(k|H > 0)$$

(25)

Where the histogram H is computed for $I(x, y)$

(v). Other FMFs: Functions in this group are those which are not in above categories due to their working principles.

(a). *Image curvature (ICR) [167]:* Image surface can be employed for gray-levels interpolation, and the curvature of same surface may used as focus measure

$$F_{ICR} = |c_0| + |c_1| + |c_2| + |c_3|, \qquad (26)$$

Where $C = (c_0, c_1, c_2, c_3)^T$ is the coefficients vector use to interpolate a quadratic surface $f(x, y) = c_0 x + c_1 y + c_2 x^2 + c_3 y^2$. Following two convolution masks are applied to compute c using least square

$$c_0 = M_1 * I \qquad c_2 = \frac{3}{2} M_2 * I - M_2^T * I$$

$$c_1 = M_1^T * I \qquad c_3 = \frac{3}{2} M_2^T * I - M_2 * Irvex,$$

Where

$$M_1 = \frac{1}{6} \begin{pmatrix} -1 & 0 & 1 \\ -1 & 0 & 1 \\ -1 & 0 & 1 \end{pmatrix} \qquad M_2 = \frac{1}{5} \begin{pmatrix} 1 & 0 & 1 \\ 1 & 0 & 1 \\ 1 & 0 & 1 \end{pmatrix}$$

(b). *Hemli and Scherer's mean (HSM) [167]:* Local contrast is measured by computing the ratio, $R(x, y)$, between the intensity level of each pixel $I(x, y)$ and the mean intensity level of its neighborhood $\mu(x, y)$. Sum of this local contrast ratio is used as focus measure

$$R(x, y) = \begin{cases} \dfrac{\mu(x, y)}{I(x, y)}, & \mu(x, y) \geq I(x, y) \\ \dfrac{I(x, y)}{\mu(x, y)} & Otherwise, \end{cases} \qquad (27)$$

Ratio will be near to one if image is defocused due to low contrast. $\mu(x, y)$ is calculated by centering $M \times N$ neighborhood at (x, y).

(c). *Steerable filters-base (SFB) [168]:* Filtered version of the image (I_f) is used as focus measure by Minhas et al.

$$F_{SFB} = \sum_{(i,j) \in I(x,y)} I_f(i, j), \qquad (28)$$

$$\text{Where } I_f(i, j) = \max\left\{ R_{(i,j)}^{\theta_1}, R_{(i,j)}^{\theta_2}, \dots R_{(i,j)}^{\theta_N} \right\}, \qquad (29)$$

Where $R^{\theta_n}, n = 1, 2, \dots N$, is the response of image to the *n*-th steerable filter defined as:

$$R^{\theta_n} = \cos(\theta_n)(I * \Gamma_x) + \sin(\theta_n)(I * \Gamma_y), \qquad (30)$$

With Γ_x and Γ_y are the Gaussian derivatives described in (Eq.4)

(d). Spatial frequency measure (SFM) [96]: This function was proposed by Huang W et al., for multi-focal image fusion and can be defined as *[96]*

$$F_{SFM} = \sqrt{\sum_{(i,j)\,\in\,I\,(x,y)} I_x(i,j)^2 + \sum_{(i,j)\,\in\,I\,(x,y)} I_y(i,j)^2}, \qquad (31)$$

Where I_x and I_y are the first derivatives of an image in the horizontal and vertical direction, respectively.

3.2.2. Image Preprocessing

(i). Filtering

Median filtering is used to remove the noise for improving the quality of image. The median filter with 2x2, 4x4 and 8x8 mask sizes were used to see the effect on the performance of FMFs.

(ii). Image distortion

Poisson noise was incorporated to check the robustness of FMFs on noisy images. Poisson noise was generated from the image instead of adding artificial noise. Generally, FMFs performances compromise due to the higher level of noise [98].

Reduced contrast level smoothen the edges in images which affect the discrimination of the best focus image from defocused ones. The contrast was incorporated to check the robustness of FMFs to poor contrast. Generally, a robust FMF does not affect by low contrast [100]. The image pixels intensity values were mapped to the narrower range for reducing the contrast. Following MATLAB function were used for contrast reduction:

$$RC = \text{imadjust (I, [0\ 1], [0\ 0.8])}; \qquad (32)$$

Where I = input image and RC = contrast reduced output image.

The *saturation level* of an image can also perturbed the performance of FMFs [100]. Initially, The RGB (red, green and blue) images were converted to HSV (Hue, saturation and value). Furthermore, saturation of HSV images was increased to check the robustness of FMFs. Following MATLAB function was used to accomplish this task:

$$I\,(:,:,2) = I(:,:,2) * S; \qquad (33)$$

Where, I is the HSV input image and S is the multiplication factor used to increase the saturation level. The saturation level was increase by 25% and 50% using the S values of 1.25 and 1.50, respectively.

Uneven illumination was incorporated to images using a luminance gradient for evaluating the efficacy of FMFs in low signal-to-noise ratio. The quadratic polynomial function is used to represent luminance gradient as grey-scale image, and this gray-scale image is multiplied with original one to get resultant image. Different maximum intensity values (0.8, 0.9 and 1.0) and same minimum intensity value (0.0) were used to check the efficacy of FMFs.

3.2.3. Evaluation of FMFs

The following criteria were used to evaluate the FMFs.

Accuracy criterion: The accuracy score of 1, 0.5 or 0 was assigned if the best-focused image was correctly identified; if the second best-focused (with marginal difference) was identified as the best-focused; or if the FMF was failed, respectively. The accuracy in percent is calculated as follow:

$$\frac{\text{Sum of all score}}{\text{Total number of stacks}} \times 100 \hspace{2cm} (\,34\,)$$

The higher is the percent, better is the algorithm.

Focus error: The motor step difference between predicted and manually obtained best focus image was considered as the focus error [98]. Each motor step corresponds to a different focus distance. The difference between two neighboring motor steps is about 2-3 μm.

Number of false maxima: The number of false maxima produced by an FMF was computed. It is the total number of maxima without the global maxima.

Full width at half maximum (FWHM): This criterion was used to calculate the narrowness of the peak as narrower curve indicates rapid convergence rate of FMFs to the best focus point. The width of focus curve was determined at half of its height for the top FMFs to evaluate their efficacy. The DC offset was removed prior to calculate the FWHM. Finally, the FWHW values with and without DC offset removal were presented for better interpretation.

Ranking of FMFs: every FMF was ranked base on its accuracy, focus error and number of false maxima. These values were summed to get an overall score for each FMF. Overall score was calculated before and after each preprocessing step. The smaller is the score, better is the rank. Top five ranked FMFs were selected with minimal scores before

applying preprocessing techniques. The robustness of the FMFs was evaluated by analyzing their invariance to preprocessing techniques. It was evaluated through calculating the global score by summing all the overall ranks. Global rank is assigned to each FMF based on its global score. The smaller is the score, the better is the rank; therefore more robust is the FMF.

3.3. Results and Discussion

Accurate autofocusing helps in capturing of focused images that contribute significantly to automated microscopy development by performing better bacilli screening through segmentation methods on focused images [28]. Although several studies were performed to find out the effective FMFs for microscopic images, most of their results led to different conclusions [28, 29, 97, 98, 102]. Identification of the best focused images of CM using FMFs is challenging and difficult task due to the higher density background (overstaining) and artifacts. In this study, most commonly used 24 FMFs were evaluated to determine the robust focusing functions for CM images. These FMFs were implemented in MATLAB. Each FMF is evaluated on unbiased approach. FMFs were also evaluated on Smartphone camera-enabled microscope as these were not tested in the previous studies. Four focus measures (BGR, GLLV, RWC and RHS) were not producing a Gaussian curve which (a preliminary criterion for a good FMF); therefore, excluded from the study (Fig. 3.2) [94]. Every FMF was evaluated separately on different microscopes to check the effect of different configurations, and the overall performance was also evaluated (Table 3.1, Fig. 3.3 and Table 3.2). Mean execution time of every FMF is presented in Table 3.3. Most of the FMFs have time complexity of $O(XY)$, where X and Y are the dimensions of an image [29], which shows that the computation time is directly proportional to the size of the input image. Following sections provide the performance of FMFs in different imaging conditions.

Table 3.1 Performance of focus measures functions (FMFs) without pre-processing

Methods[*]	Accuracy	Focus Error	False Max	Overall Score	Overall Rank
GDR	96.77(1)	0.03(1)	0.07(1)	3	1
TGR	96.77(1)	0.03(2)	0.1(2)	5	2
HSM	95.16(2)	0.05(2)	0.28(5)	9	3
THR	95.16(2)	0.34(6)	0.1(2)	10	4
SFB	90.32(3)	0.39(7)	0.07(1)	11	5
GNV	88.71(4)	0.27(5)	0.17(3)	12	6
GLV	87.1(5)	0.16(3)	0.21(4)	12	6
ICR	95.16(2)	0.03(1)	0.69(11)	14	7
SD	88.71(4)	0.6(9)	0.17(3)	16	8
SFM	90.32(3)	0.39(7)	0.41(9)	19	9
VCR	85.48(6)	0.66(10)	0.21(4)	20	10
VGR	80.65(7)	0.23(4)	0.41(9)	20	10
EGR	75.81(8)	1.15(12)	0.34(7)	27	11
SGR	74.19(9)	0.52(8)	0.48(10)	27	11
MLP	75.81(8)	1.37(13)	0.34(7)	28	12
EHS	74.19(9)	0.68(11)	0.38(8)	28	12
DLP	72.58(10)	1.92(15)	0.31(6)	31	13
SWC	64.52(12)	1.94(16)	0.17(3)	31	13
ELP	67.74(11)	2.1(17)	0.76(12)	40	14
VWC	62.9(13)	1.66(14)	6.03(13)	40	14
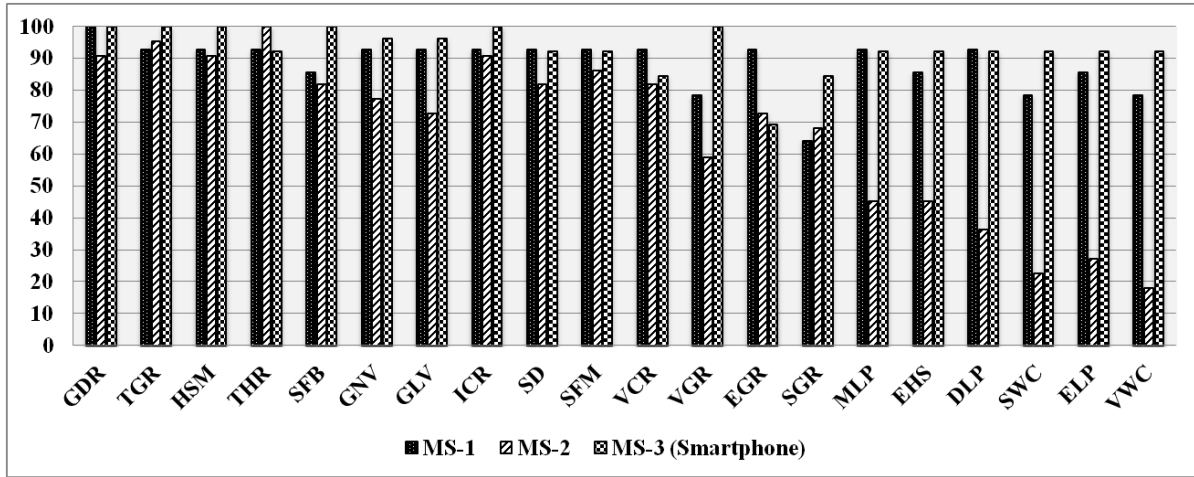
Fig. 3.3 Microscopes-wise accuracy and mean accuracy in percentage of FMFs without pre-processing

Table 3.2 Microscopes wise Performance of focus measure functions (without preprocessing)

Method	MS-1[b]	MS-2[b]	MS-3[b]	Mean Accuracy
			(Smartphone)	
GDR	100	90.91	100	96.97
TGR	92.86	95.45	100	96.1
HSM	92.86	90.91	100	94.59
THR	92.86	100	92.31	95.06
SFB	85.71	81.82	100	89.18
GNV	92.86	77.27	96.15	88.76
GLV	92.86	72.73	96.15	87.25
ICR	92.86	90.91	100	94.59
SD	92.86	81.82	92.31	89
SFM	92.86	86.36	92.31	90.51
VCR	92.86	81.82	84.62	86.43
VGR	78.57	59.09	100	79.22
EGR	92.86	72.73	69.23	78.27
SGR	64.29	68.18	84.62	72.36
MLP	92.86	45.45	92.31	76.87
EHS	85.71	45.45	92.31	74.49
DLP	92.86	36.36	92.31	73.84
SWC	78.57	22.73	92.31	64.54
ELP	85.71	27.27	92.31	68.43
VWC	78.57	18.18	92.31	63.02

[b]MS-1, MS-2 & MS-3 indicate Microscope 1, 2 & 3 respectively.

Table 3.3 Mean execution time of focus measure functions (FMFs) with standard deviation on overall datasets collected from three microscopes

Methods	Mean (Sec.)	SD (Sec.)	Methods	Mean (Sec.)	SD (Sec.)
GDR	4.43	1.96	VCR	2.46	1.11
TGR	2.41	1.11	VGR	3.23	1.49
HSM	5.21	2.35	SGR	0.79	0.35
THR	2.90	1.30	EGR	2.40	1.08
SFB	20.30	9.10	EHS	0.43	0.18
GNV	0.90	0.40	MLP	2.17	0.98
GLV	0.97	0.44	DLP	4.39	2.04
ICR	3.30	1.55	SWC	21.41	9.84
SD	0.88	0.40	ELP	1.30	0.59
SFM	2.71	1.21	VWC	24.31	11.14

3.3.1. Without image preprocessing

Average performances of 20 FMFs were determined on 31 datasets from three microscopes (Table 3.1). Performance of each individual microscope is also provided to show the consistent performance of FMFs w.r.t different instrument configurations (Fig. 3.3, Table 3.2). The Gaussian derivative (GDR), Tenengrad (TGR), Helmli's measure (HSM), thresholded gradient (THR) and steerable filter-based (SFB) focus measures were identified as top five FMFs based on their rank computed by accuracy (>90%), focus error and number

of false maxima (Fig. 3.3, Table 3.1). The performances of top five FMFs were almost invariant to three different microscopes with accuracy rate of >90%. Performances of The Laplacian and wavelet-based FMFs had varied significantly across the three microscopes (Fig. 3.3), which suggest that these FMFs might be sensitive to different brightness, illumination level, etc. Performance of top FMFs were better in Smartphone camera-enable microscope (MS-3) which encourages the use of this cost-effective facility for the automatic bacilli detection, especially in remote areas of TB-endemic countries. GDR and TGR performances were also better on FM images with the accuracy of 86.67% and 89%, respectively [98]. In this study, the GDR method outperformed and ranked 1st in all the criteria. Additionally, the HSM and SFB, which were not previously tested on microscopic data, ranked among top five FMFs on CM images (Table 3.1). ICR and SFM have achieved the accuracy >90% but not considered as robust FMFs due to the high rate of focus error and false maxima.

3.3.2. Image Preprocessing

(i). Robustness of focus measures w.r.t pre-processing filtering methods

Generally, The median filters are used to remove noise from the images as the performance of several FMFss were improved slightly after applying the filter with 2x2 mask size, whereas the accuracy was reduced by increased mask size of 8x8 [98]. In this study, median filters with 2x2, 4x4 and 8x8 mask size were used to determine their effects on the performance of FMFs (Fig. 3.4, and Table 3.4). The performance of top five FMFs were mostly invariant to all the median filters except in THR where performance was reduced considerably for 8x8 window size. The performance of GDR was independent to all the median filters; while VGR was failed drastically may be due to the less variation in the intensity levels due to the smoothening. Performances of modified Laplacian and diagonal Laplacian were improved significantly. Performances of other methods were inconsistent w.r.t. different window sizes.
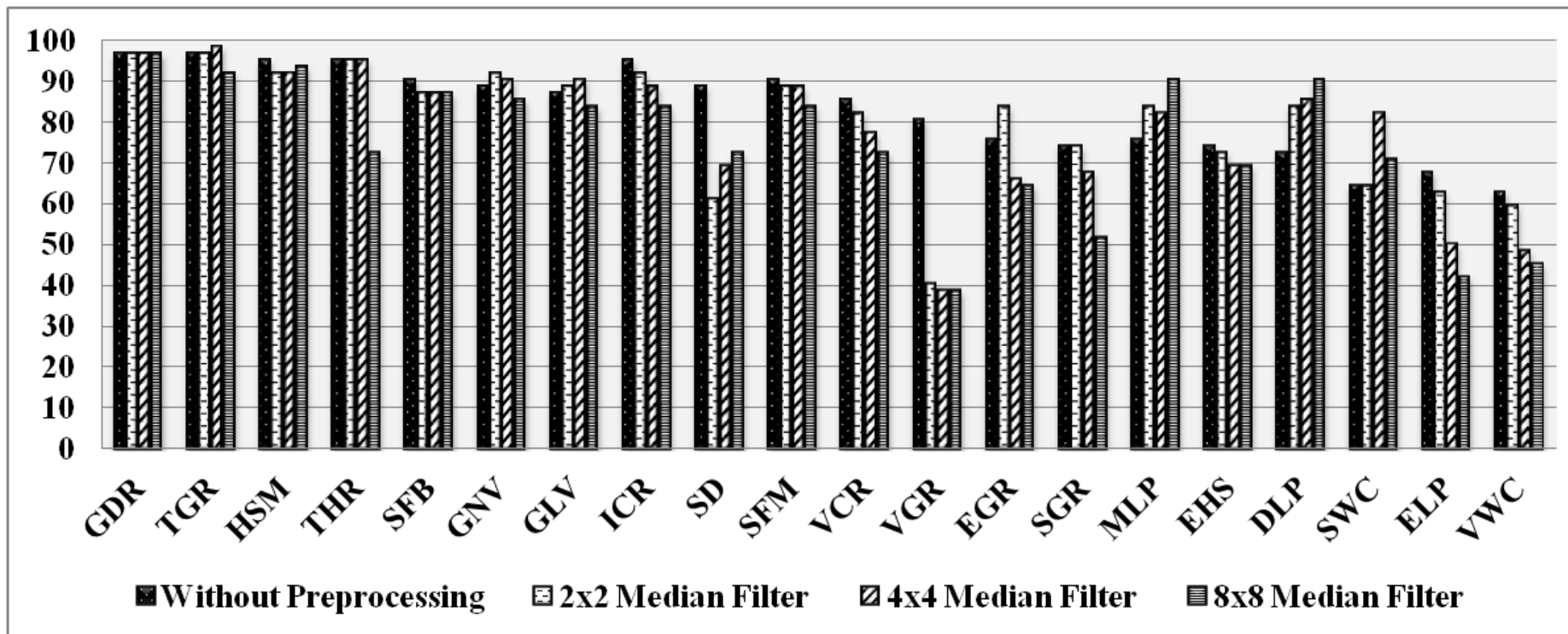
Fig. 3.4 Accuracies of focus measure functions (FMFs) in percent (without preprocessing vs. median filtering)

Methods	AC 2x2[a,b]	FE 2x2[a,b]	FM 2x2[a,b]	OS 2x2[a,b]	AC 4x4[a,b]	FE 4x4[a,b]	FM 4x4[a,b]	OS 4x4[a,b]	AC 8x8[a,b]	FE 8x8[a,b]	FM 8x8[a,b]	OS 8x8[a,b]
GDR	96.77(1)	0.03(1)	0.07(1)	3(1)	96.77(2)	0.03(2)	0.07(1)	5(2)	96.77(1)	0.03(1)	0.07(1)	3(1)
TGR	96.77(1)	0.03(1)	0.07(4)	6(2)	98.39(1)	0.02(1)	0.07(2)	4(1)	91.94(3)	0.63(8)	0.1(5)	16(4)
HSM	91.94(3)	0.05(2)	0.45(10)	15(5)	91.94(4)	0.08(3)	0.66(16)	23(7)	93.55(2)	0.06(2)	0.83(19)	23(8)
THR	95.16(2)	0.18(4)	0.07(3)	9(3)	95.16(3)	0.18(5)	0.07(3)	11(3)	72.58(8)	2.24(13)	0.31(10)	31(10)
SFB	87.1(5)	0.27(5)	0.1(2)	12(4)	87.1(7)	0.42(8)	0.1(4)	19(6)	87.1(5)	0.42(5)	0.1(4)	14(3)
GNV	91.94(3)	0.18(4)	0.17(5)	12(4)	90.32(5)	0.03(2)	0.14(5)	12(4)	85.48(6)	0.34(4)	0.21(7)	17(5)
GLV	88.71(4)	0.15(3)	0.21(8)	15(5)	90.32(5)	0.16(4)	0.17(7)	16(5)	83.87(7)	0.26(3)	0.21(8)	18(6)
ICR	91.94(3)	0.18(4)	0.24(19)	26(8)	88.71(6)	0.37(7)	0.34(11)	24(8)	83.87(7)	0.52(6)	0.28(9)	22(7)
SD	61.29(12)	3.06(15)	0.45(6)	33(12)	69.35(11)	2.66(15)	0.34(12)	38(12)	72.58(8)	2.08(11)	0.38(12)	31(10)
SFM	88.71(4)	0.27(5)	0.45(16)	25(7)	88.71(6)	0.31(6)	0.66(17)	29(10)	83.87(7)	0.52(6)	0.86(20)	33(12)
VCR	82.26(7)	0.95(9)	0.38(9)	25(7)	77.42(10)	1.65(14)	0.76(20)	44(14)	72.58(8)	1.82(10)	0.52(15)	33(12)
VGR	40.32(15)	3.85(16)	0.66(15)	46(16)	38.71(16)	4.39(19)	0.66(18)	53(16)	38.71(16)	4.1(17)	0.66(18)	51(15)
EGR	83.87(6)	1.03(10)	0.38(12)	28(9)	66.13(13)	3.02(17)	0.55(14)	44(14)	64.52(11)	3.03(14)	0.55(17)	42(14)
SGR	74.19(8)	1(10)	0.45(17)	35(13)	67.74(12)	1.42(13)	1.14(24)	49(15)	51.61(12)	3.39(15)	2.48(24)	51(15)
MLP	83.87(6)	0.77(6)	0.21(13)	25(7)	82.26(9)	0.79(11)	0.21(9)	29(10)	90.32(4)	0.58(7)	0.1(3)	14(3)
EHS	72.58(9)	0.89(8)	0.38(14)	31(11)	69.35(11)	0.85(12)	0.41(13)	36(11)	69.35(10)	0.95(9)	0.41(13)	32(11)
DLP	83.87(6)	0.77(6)	0.21(11)	23(6)	85.48(8)	0.69(9)	0.17(6)	23(7)	90.32(4)	0.58(7)	0.1(2)	13(2)
SWC	64.52(10)	1.07(12)	0.45(7)	29(10)	82.26(9)	0.73(10)	0.17(8)	27(9)	70.97(9)	2.13(12)	0.1(6)	27(9)
VWC	59.68(13)	0.83(7)	0.31(24)	44(14)	48.39(15)	2.74(16)	0.24(10)	41(13)	45.16(14)	3.45(16)	0.31(11)	41(13)
ELP	62.9(11)	1.79(14)	0.86(20)	45(15)	50(14)	3.37(18)	0.83(21)	53(16)	41.94(15)	4.48(19)	1(21)	55(16)

[a]AC, FE, FM and OS indicate accuracy, focus error, false maximum and overall score after median filtering with window size of 2x2, 4x4 and 8x8. Overall score for a FMF is calculated by summing individual ranking of three criterions. Values in parenthesis denotes anks in three different criterion (accuracy, Focus error and false maximum).

[b]Values in parentheses values indicate ranking of that parameter.

(ii). Robustness to image distortion

The robustness of FMFs in various types of noises is very important, especially for CM images with relatively higher noise and density than FM images. Poisson noise, reduced contrast, increased saturation and uneven illumination were incorporated to determine the effect of image distortion on FMFs performance.

In the 1st step, Poisson noise was incorporated in all the images. The performance of most of FMFs was reduced marginally or drastically after noise addition (Fig. 3.5, and Table 3.5). The performances of top five FMFs were relatively invariant except for THR where accuracy was reduced drastically. GLV, ICR, standard deviation (SD) and GNV were the other FMFs which were invariant to the Poisson noise. FMFs such as THR, SFM, EGR, SGR, Laplacian and wavelet based FMFs were failed in noisy condition. TGR and GDR were also invariant to noise addition in a previous study [100], while GNV was the most robust FMF [105].
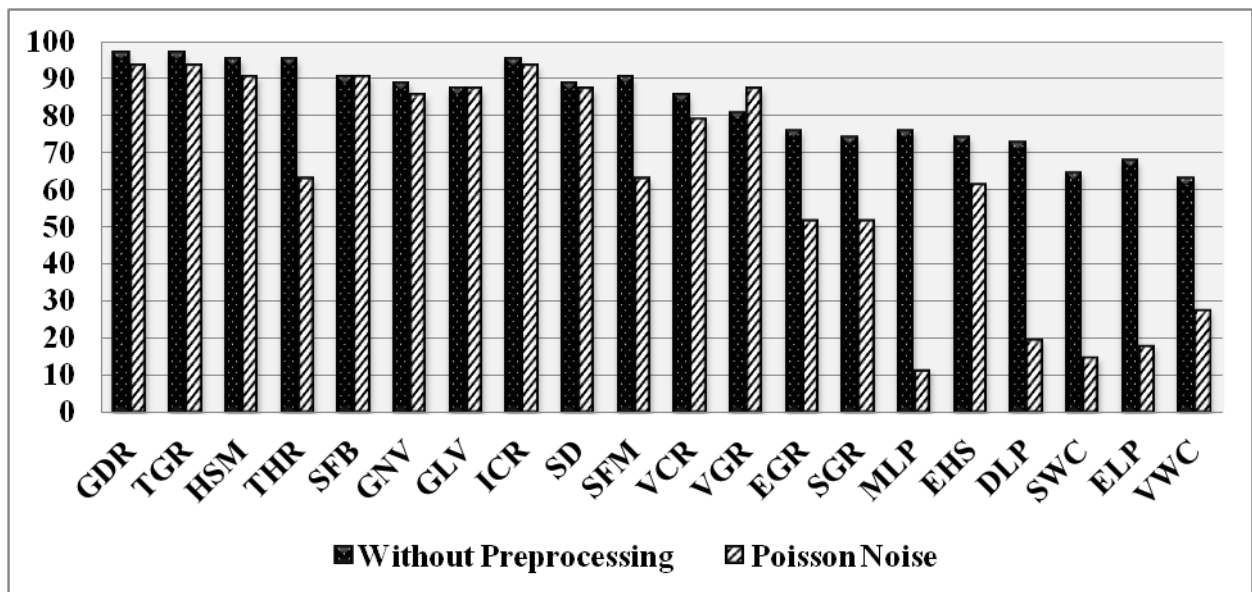
Fig. 3.5 Accuracy comparison (Without preprocessing vs. noise addition) of focus measures functions (FMFs)

Table 3.5 Performance of focus measure functions (FMFs) after noise addition

Methods	Average accuracy[b]	Focus Error[b]	False Maximum[b]	Overall Score[a, b]
GDR	93.55(1)	0.06(1)	0.07(1)	3(1)
TGR	93.55(1)	0.06(1)	0.1(2)	4(2)
HSM	90.32(2)	0.1(2)	0.17(3)	7(3)
THR	62.90(6)	1.34(9)	0.24(5)	20(9)
SFB	90.32(2)	0.29(5)	0.07(1)	8(4)
GNV	85.48(4)	0.31(6)	0.17(3)	13(7)
GLV	87.1(3)	0.19(4)	0.21(4)	11(5)
ICR	93.55(1)	0.06(1)	0.07(1)	3(1)
SD	87.1(3)	0.19(4)	0.21(4)	11(5)
SFM	62.9(6)	1.4(10)	0.24(5)	21(10)
VCR	79.03(5)	0.76(7)	0.21(4)	16(8)
VGR	87.1(3)	0.13(3)	0.38(6)	12(6)
EGR	51.61(8)	2.97(12)	0.41(7)	27(12)
SGR	51.61(8)	1.58(11)	0.45(8)	27(12)
MLP	11.29(13)	5.53(16)	0.45(8)	37(14)
EHS	61.29(7)	1.23(8)	0.48(9)	24(11)
DLP	19.35(10)	5(14)	0.45(8)	32(13)
SWC	14.52(12)	5.31(15)	0.59(10)	37(14)
ELP	17.74(11)	5.79(17)	0.86(12)	40(15)
VWC	27.42(9)	4.05(13)	0.69(11)	33(13)

[a]Overall score for a FMF is calculated by summing individual ranking of three criterions.

[b]Values in parentheses values indicate ranking of that parameter.

In the 2nd step, image contrast was reduced using "imadjust" function of MATLAB. Generally, minor change in contrast does not have any effects on FMFs performance [91, 100]. In this study, the performances of all the FMFs were affected marginally by reduced contrast (Fig. 3.6). Performances of most of the FMFs were remained relatively similar after contrast reduction (Table 3.6).
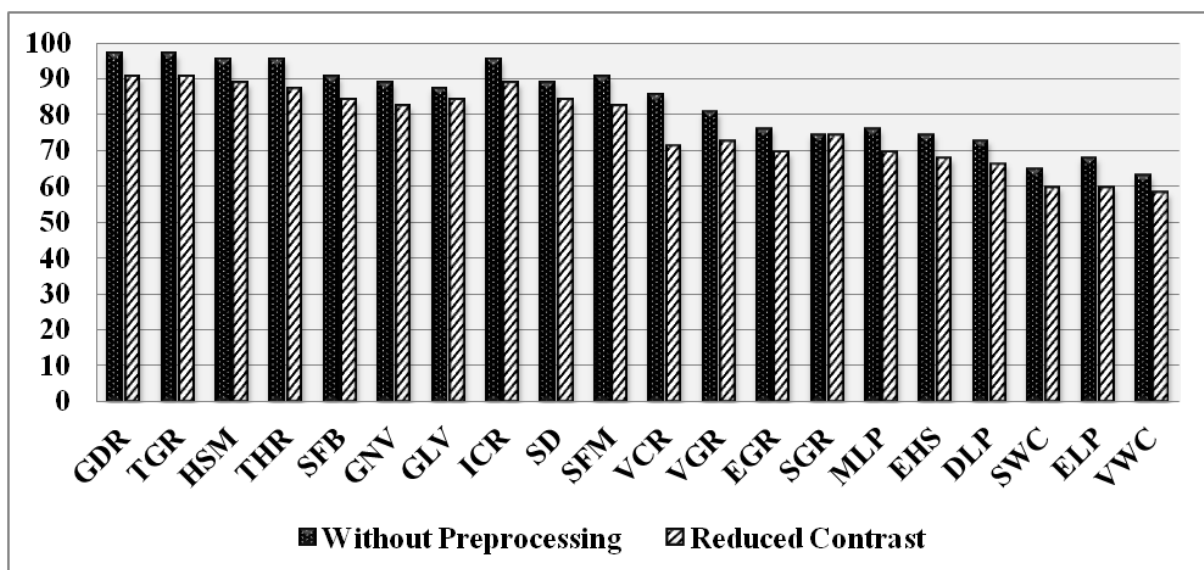
Fig. 3.6 Performance of focus measure functions (FMFs) after contrast reduction (%)

Table 3.6 Performance of focus measure functions (FMFs) after contrast reduction.

Methods[a]	Average accuracy[c]	Focus Error[c]	False Maximum[c]	Overall Score[b, c]
GDR	90.32(1)	0.1(1)	0.1(1)	3(1)
TGR	90.32(1)	0.27(3)	0.14(2)	6(2)
HSM	88.71(2)	0.18(2)	0.17(3)	7(3)
THR	88.71(2)	0.44(5)	0.1(1)	8(4)
TGR	87.1(3)	0.58(8)	0.14(2)	13(6)
SFM	82.26(5)	0.73(10)	0.24(5)	20(8)
SFB	83.87(4)	0.48(6)	0.1(1)	11(5)
GNV	82.26(5)	0.37(4)	0.21(4)	13(6)
SD	83.87(4)	0.48(6)	0.24(5)	15(7)
GLV	83.87(4)	0.48(6)	0.24(5)	15(7)
VCR	70.97(8)	1.39(12)	0.62(11)	31(13)
VGR	72.58(7)	0.5(7)	0.52(9)	23(9)
EGR	69.35(9)	1.37(11)	0.45(8)	28(11)
MLP	69.35(9)	2.11(13)	0.38(7)	29(12)
EHS	67.74(10)	1.39(12)	0.38(7)	29(12)
SGR	74.19(6)	0.65(9)	0.52(9)	24(10)
DLP	66.13(11)	2.31(14)	0.34(6)	31(13)
ELP	59.68(12)	2.37(15)	1.59(12)	39(15)
SWC	59.68(12)	2.5(16)	0.52(9)	37(14)
VWC	58.06(13)	2.87(17)	0.59(10)	40(16)

[b]Overall score for a FMF is calculated by summing individual ranking of three criterions
[c]Parentheses values indicate ranking of that parameter.

In the 3rd step, saturation levels of all the images were increased by 25% and 50%. Generally, increased saturation level affects the performance of FMFs [100]. The performance of top five FMFs was dropped slightly with increase in saturation by 25% and 50% (Fig. 3.7).
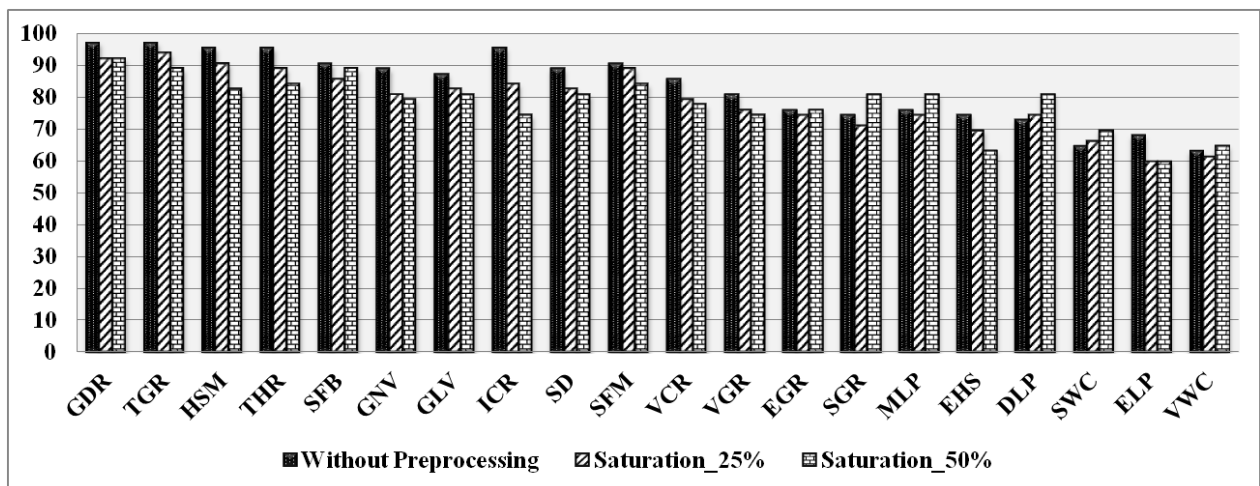
Fig. 3.7 Accuracy in percent of focus measures (Without preprocessing vs. increase saturation level)

Performances of top five FMFs were relatively remained similar (Table 3.7). Pertuz et al. [100] checked the effect of saturation level on the images acquired from the commercial camera and synthetically generated sequences. Laplacian-based operators were sensitive to

increased saturation, whereas in this study, wavelet-based methods were also inconsistent to saturation level.

Table 3.7 Performance of focus measure functions after increased saturation level (25% and 50%)

Methods	AC 25%[b,c]	FE 25% [b,c]	FM 25%[b,c]	OS 25%	AC 50%	FE 50%	FM 50%	OS 50%
GDR	91.94(2)	0.11(3)	0.07(1)	6(2)	91.94(1)	0.15(1)	0.07(1)	3(1)
TGR	93.55(1)	0.03(1)	0.07(1)	3(1)	88.71(2)	0.18(2)	0.14(3)	7(2)
HSM	90.32(3)	0.06(2)	0.14(3)	8(3)	82.26(4)	0.56(8)	0.17(4)	16(5)
THR	88.71(4)	0.56(9)	0.1(2)	15(5)	83.87(3)	0.65(10)	0.17(6)	19(6)
SFB	85.48(5)	0.53(8)	0.1(2)	15(5)	88.71(2)	0.37(6)	0.07(2)	10(3)
GNV	80.65(8)	0.32(6)	0.24(5)	19(7)	79.03(6)	0.37(6)	0.28(11)	23(9)
GLV	82.26(7)	0.18(4)	0.28(6)	17(6)	80.65(5)	0.29(3)	0.31(13)	21(7)
ICR	83.87(6)	0.77(11)	0.17(4)	21(8)	74.19(9)	1.68(15)	0.24(9)	33(14)
SD	82.26(7)	0.18(4)	0.28(6)	17(6)	80.65(5)	0.29(3)	0.31(14)	22(8)
SFM	88.71(4)	0.24(5)	0.1(2)	11(4)	83.87(3)	0.35(5)	0.17(5)	13(4)
VCR	79.03(9)	0.98(13)	0.38(8)	30(10)	77.42(7)	1(12)	0.28(12)	31(13)
VGR	75.81(10)	0.34(7)	0.41(9)	26(9)	74.19(9)	0.32(4)	0.38(16)	29(12)
EGR	74.19(11)	0.87(12)	0.31(7)	30(10)	75.81(8)	0.6(9)	0.28(10)	27(11)
SGR	70.97(12)	0.61(10)	0.45(10)	32(11)	80.65(5)	0.43(7)	0.34(15)	27(11)
MLP	74.19(11)	1.87(16)	0.28(6)	33(12)	80.65(5)	0.94(11)	0.21(8)	24(10)
EHS	69.35(13)	1.27(14)	0.38(8)	35(14)	62.9(12)	1.66(14)	0.45(18)	44(16)
DLP	74.19(11)	1.94(17)	0.28(6)	34(13)	80.65(5)	0.94(11)	0.21(7)	23(9)
SWC	66.13(14)	1.76(15)	0.45(10)	39(15)	69.35(10)	1.45(13)	0.41(17)	40(15)
ELP	59.68(16)	2.37(18)	0.83(12)	46(17)	59.68(13)	1.92(18)	0.83(21)	52(19)
VWC	61.29(15)	2.71(19)	0.66(11)	45(16)	64.52(11)	1.9(17)	0.48(19)	47(17)

[b]AC, FE and FM denote accuracy, focus error, false maximum and overall score for 25% and 50% saturation levels increment.
[c]Parentheses values indicate ranking of that parameter

In the 4th step, uneven illumination was added in all the images with different maximum intensity if 1, 0.9 and 0.8. Mateos-Pérez et al. have tested it on FM images but did not find any negative effect on the performance of FMFs [98]. In this study, Performance of FMFs were significantly changed after incorporating illumination, but the top five FMFs were mostly invariant to different uneven illumination conditions. (Fig. 3.8, and Table 3.8).
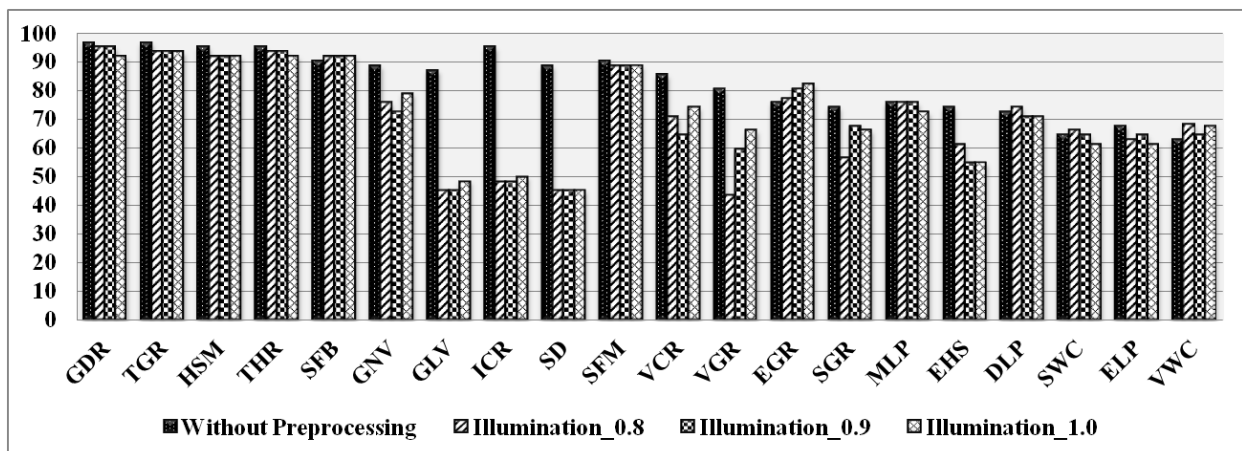
Fig. 3.8 Accuracy in percent of focus measure functions (Without preprocessing vs. uneven illumination)

3.3.3. Discussion

The main goal of this study was to discover the most accurate and robust FMFs implementable to sputum smear CM images acquired at 100x magnification. From the earlier studies, it is concluded that the effectiveness of FMFs rely on different imaging contents. Comprehensive and comparative analysis of 24 FMFs have been carried out to identify the most robust FMFs. The effectiveness of these FMFs in various imaging conditions (*e.g.* noise, saturation level, uneven illumination, etc.) was evaluated to check their robustness. Seven FMFs namely, GDR, TGR, HSM, THR, ICR, SFB and SFM have achieved the accuracy >90% (Table 3.1 and Fig. 3.2). Top five FMFs *i.e.* GDR, TGR, HSM, THR and SFB were determined based on overall ranks calculated by accuracy, focus error and number of false maxima. Four out of five FMFs *i.e.* GDR, TGR, SFB and HSM were identified as the most robust as these FMFs were invariant to the filtering and image distortions conditions *i.e.* noise, contrast, saturation and uneven illumination (Fig. 3.2, Table 3.1). These four FMFs alongside THR were also tested on a single (MS-1) microscope with different imaging conditions (Table S9). Performance was similar to the combined results of three microscopes (Fig. 3.4, Fig.4, Fig.5, Fig.6, Fig.7).

To further verify our results, the global ranking (Table 3.9, and Table S10) and the differences in FMFs performances before and after preprocessing (Table 3.10, 3.11 and 3.12) were computed. Outcomes of this analysis also support our previous findings that GDR (1st), TGR (2nd), SFB (3rd) and HSM (4th) are the most robust and accurate FMFs, and have minor differences in accuracy, focus error and false maxima rate of before and after preprocessing results. However, THR and GNV along with other FMFs were less robust and differences in performance were high. GDR (86.67%) and TGR (89%) FMFs can be used in FM images as they showed better performances in both modalities. The Laplacian and Wavelet-based operators have shown better performances in commercial camera and synthetically generated images, but these FMFs had shown poor accuracy in CM images due to the higher sensitivity to noise [100]. SFB and HSM are the significant finding of this study as their performances were not evaluated on microscopic images, and their accuracies were not good in real image of scenes [100]. SFB and HSM were also evaluated on FM images, but both have produced poor accuracies of 20% and 61.4% respectively.

Table 3.8 Performance of focus measure functions after addition of uneven illumination.

Methods	AC 0.8[a,c]	FE 0.8[a,c]	FM 0.8[a,c]	OS 0.8[a,c]	AC 0.8	FE 0.9	FM 0.9	OS 0.9	AC 1.0	FE 1.0	FM 1.0	OS 1.0
GDR	95.16(1)	0.02(1)	0.03(1)	3(1)	95.16(1)	0.02(1)	0.03(1)	3(1)	91.94(2)	0.02(1)	0.03(1)	4(1)
TGR	93.55(2)	0.03(2)	0.07(2)	6(2)	93.55(2)	0.03(2)	0.07(2)	6(2)	93.55(1)	0.03(2)	0.07(2)	5(2)
HSM	91.94(3)	0.05(3)	0.1(3)	9(4)	91.94(3)	0.21(4)	0.1(3)	10(4)	91.94(2)	0.05(3)	0.1(3)	8(4)
THR	93.55(2)	0.03(2)	0.07(2)	6(2)	93.55(2)	0.03(2)	0.1(3)	7(3)	91.94(2)	0.03(2)	0.1(3)	7(3)
SFB	91.94(3)	0.15(4)	0.03(1)	8(3)	91.94(3)	0.15(3)	0.03(1)	7(3)	91.94(2)	0.15(4)	0.03(1)	7(3)
GNV	75.81(6)	1.24(10)	0.28(4)	20(7)	72.58(7)	1.5(10)	0.31(6)	23(8)	79.03(5)	0.73(7)	0.31(5)	17(7)
GLV	45.16(14)	3.16(17)	0.62(11)	42(17)	45.16(14)	3.48(17)	0.62(11)	42(16)	48.39(14)	2.61(17)	0.62(8)	39(16)
ICR	48.39(13)	4.06(18)	0.55(10)	41(16)	48.39(13)	4.16(19)	0.55(10)	42(16)	50(13)	3.52(19)	0.55(7)	39(16)
SD	45.16(14)	3.16(17)	0.62(11)	42(17)	45.16(14)	3.61(18)	0.62(11)	43(17)	45.16(15)	3.16(18)	0.62(8)	41(18)
SFM	88.71(4)	0.21(5)	0.1(3)	12(5)	88.71(4)	0.24(5)	0.14(4)	13(5)	88.71(3)	0.21(5)	0.14(4)	12(5)
VGR	43.55(16)	2.6(16)	4.79(15)	47(18)	59.68(11)	0.95(8)	1.45(13)	32(12)	66.13(10)	0.94(10)	1.21(11)	31(13)
VCR	70.97(8)	1.13(8)	1.59(12)	28(10)	64.52(10)	1.52(11)	2.48(15)	36(13)	74.19(6)	0.87(8)	1.24(12)	26(10)
EGR	77.42(5)	0.42(6)	0.55(10)	21(8)	80.65(5)	0.39(6)	0.45(8)	19(6)	82.26(4)	0.37(6)	0.31(5)	15(6)
SGR	56.45(13)	1.55(13)	2.93(14)	40(15)	67.74(9)	0.84(7)	1.31(12)	28(10)	66.13(10)	0.9(9)	0.83(10)	29(12)
EHS	61.29(12)	1.74(14)	0.41(7)	33(13)	54.84(12)	2.61(16)	0.48(9)	37(14)	54.84(12)	1.52(15)	0.48(6)	33(14)
MLP	75.81(6)	0.98(7)	0.31(5)	18(6)	75.81(6)	1.15(9)	0.28(5)	20(7)	72.58(7)	0.98(11)	0.31(5)	23(8)
DLP	74.19(7)	1.16(9)	0.34(6)	22(9)	70.97(8)	1.81(12)	0.34(7)	27(9)	70.97(8)	1.16(12)	0.31(5)	25(9)
SWC	66.13(10)	1.47(11)	0.48(9)	30(12)	64.52(10)	2.03(13)	0.45(8)	31(11)	61.29(11)	1.47(14)	0.76(9)	34(15)
ELP	62.9(11)	2.4(15)	2.38(13)	39(14)	64.52(10)	2.32(14)	1.86(14)	38(15)	61.29(11)	2.42(16)	2.17(13)	40(17)
VWC	68.33(9)	1.5(12)	0.45(8)	29(11)	64.58(10)	2.44(15)	0.34(7)	32(12)	67.74(9)	1.42(13)	0.48(6)	28(11)

[b]AC, FE and FM denote accuracy, focus error, false maximum and overall score for uneven illumination with maximum intensity rate of 0.8, 0.9 and 1.0

[c]Parentheses values indicate ranking of that parameter

Table 3.9 "Global Score" and "Global Ranking" of focus measure functions (FMFs) based on overall ranking of FMFs without preprocessing and post preprocessing. Parenthesis values denote rankings.

Methods	WPP[b]	2x2[b]	4x4[b]	8x8[b]	Noise	Cont	SAT 25[b]	SAT 50[b]	ILU 0.8[b]	ILU 0.9[b]	ILU 1.0[b]	GS[b]
GDR	3(1)	3(1)	5(2)	3(1)	3(1)	3(1)	6(2)	3(1)	3(1)	3(1)	4(1)	13(1)
TGR	5(2)	6(2)	4(1)	16(4)	4(2)	6(2)	3(1)	7(2)	6(2)	6(2)	5(2)	22(2)
HSM	9(3)	15(5)	23(7)	23(8)	7(3)	7(3)	8(3)	16(5)	9(4)	10(4)	8(4)	49(4)
THR	10(4)	9(3)	11(3)	31(10)	20(9)	13(6)	15(5)	19(6)	6(2)	7(3)	7(3)	54(5)
SFB	11(5)	12(4)	19(6)	14(3)	8(4)	11(5)	15(5)	10(3)	8(3)	7(3)	7(3)	44(3)
GNV	12(6)	12(4)	12(4)	17(5)	13(7)	13(6)	19(7)	23(9)	20(7)	23(8)	17(7)	70(6)
GLV	12(6)	15(5)	16(5)	18(6)	11(5)	15(7)	17(6)	21(7)	42(17)	42(16)	39(16)	96(8)
ICR	14(7)	26(8)	24(8)	22(7)	3(1)	8(4)	21(8)	33(14)	41(16)	42(16)	39(16)	105(10)
SD	16(8)	33(12)	38(12)	31(10)	11(5)	15(7)	17(6)	22(8)	42(17)	43(17)	41(18)	120(13)
SFM	19(9)	25(7)	29(10)	33(12)	21(10)	20(8)	11(4)	13(4)	12(5)	13(5)	12(5)	79(7)
VCR	20(10)	25(7)	44(14)	33(12)	16(8)	31(13)	30(10)	31(13)	47(18)	32(12)	31(13)	126(15)
VGR	20(10)	46(16)	53(16)	51(15)	12(6)	23(9)	26(9)	29(12)	28(10)	36(13)	26(10)	130(16)
EGR	27(11)	28(9)	44(14)	42(14)	27(12)	28(11)	30(10)	27(11)	21(8)	19(6)	15(6)	112(11)
SGR	27(11)	35(13)	49(15)	51(15)	27(12)	24(10)	32(11)	27(11)	40(15)	28(10)	29(12)	135(17)
MLP	28(12)	25(7)	29(10)	14(3)	37(14)	29(12)	33(12)	24(10)	33(13)	37(14)	33(14)	119(12)
EHS	28(12)	31(11)	36(11)	32(11)	24(11)	29(12)	35(14)	44(16)	18(6)	20(7)	23(8)	121(14)
DLP	31(13)	23(6)	23(7)	13(2)	32(13)	31(13)	34(13)	23(9)	22(9)	27(9)	25(9)	103(9)
SWC	31(13)	29(10)	27(9)	27(9)	37(14)	37(14)	39(15)	40(15)	30(12)	31(11)	34(15)	137(18)
ELP	40(14)	44(14)	41(13)	41(13)	40(15)	39(15)	46(17)	52(19)	39(14)	38(15)	40(17)	166(19)
VWC	40(14)	45(15)	53(16)	55(16)	33(13)	40(16)	45(16)	47(17)	29(11)	32(12)	28(11)	157(18)

[b]WPP denote performance without preprocessing. 2x2, 4x4 and 8x8 denote performance after median filtering with window size of 2x2, 4x4 and 8x8 respectively. SAT 25 and SAT 50 denotes the accuracy after increased saturation level of 25% and 50% respectively. ILU denote the performance after uneven illumination addition with maximum intensity value of 0.8, 0.9 and 1.0. GS denote global score computed by summing the ranking in every imaging condition.

Table 3.10 Accuracy difference of each focus measure function (FMF) without preprocessing and post-processing. Mean and standard deviation of these differences are provided in last two columns

Methods	2x2[b]	4x4[b]	8x8[b]	Noise	Cont	SAT 25[b]	SAT 50[b]	ILU 0.8[b]	ILU 0.9[b]	ILU 1.0[b]	Mean	SD[b]
GDR	0.00	0.00	0.00	3.23	6.45	4.84	4.84	1.61	1.61	4.84	2.74	2.29
TGR	0.00	1.61	4.84	3.23	6.45	3.23	8.06	3.23	3.23	3.23	3.71	2.17
HSM	3.23	3.23	1.61	4.84	6.45	4.84	12.90	3.23	3.23	3.23	4.68	3.01
THR	0.00	0.00	22.5	32.26	8.06	6.45	11.29	1.61	1.61	3.23	8.71	10.21
SFB	3.23	3.23	3.23	0.00	6.45	4.84	1.61	1.61	1.61	1.61	2.74	1.77
GNV	3.23	1.61	3.23	3.23	6.45	8.06	9.68	12.90	16.13	9.68	7.42	4.52
GLV	1.61	3.23	3.23	0.00	3.23	4.84	6.45	41.94	41.94	38.71	14.52	17.34
ICR	3.23	6.45	11.2	1.61	6.45	11.29	20.97	46.77	46.77	45.16	20.00	17.91
SD	27.4	19.35	16.1	1.61	4.84	6.45	8.06	43.55	43.55	43.55	21.45	16.15
SFM	1.61	1.61	6.45	27.42	8.06	1.61	6.45	1.61	1.61	1.61	5.81	7.61
VCR	3.23	8.06	12.9	6.45	14.5	6.45	8.06	14.52	20.97	11.29	10.65	4.96
VGR	40.3	41.94	41.9	6.45	8.06	4.84	6.45	37.10	20.97	14.52	22.26	15.45
EGR	8.06	9.68	11.2	24.19	6.45	1.61	0.00	1.61	4.84	6.45	7.42	6.58
SGR	0.00	6.45	22.5	22.58	0.00	3.23	6.45	17.74	6.45	8.06	9.35	8.12
EHS	1.61	4.84	4.84	12.90	6.45	4.84	11.29	12.90	19.35	19.35	9.84	5.97
MLP	8.06	6.45	14.5	64.52	6.45	1.61	4.84	0.00	0.00	3.23	10.97	18.32
SWC	0.00	17.74	6.45	50.00	4.84	1.61	4.84	1.61	0.00	3.23	9.03	14.5
DLP	11.2	12.90	17.7	53.23	6.45	1.61	8.06	1.61	1.61	1.61	11.61	14.87
VWC	3.23	14.52	17.7	35.48	4.84	1.61	1.61	5.43	1.68	4.84	9.10	10.25
ELP	4.84	17.74	25.8	50.00	8.06	8.06	8.06	4.84	3.23	6.45	13.71	13.77

[b]WPP denote accuracy without preprocessing. 2x2, 4x4 and 8x8 denote accuracy after median filtering with window size of 2x2, 4x4 and 8x8 respectively. SAT 25 and SAT 50 denotes the accuracy after increased saturation level of 25% and 50% respectively. ILU denote the performance after uneven illumination addition with maximum intensity value of 0.8, 0.9 and 1.0. SD denotes standard deviation in accuracies.

Table 3.11 Focus error differences of each focus measure function (FMF) without pre-processing and post-processing. Mean and standard deviation of these differences are provided in last two columns.

Methods[a]	2x2[b]	4x4[b]	8x8[b]	Noise	Cont	SAT 25[b]	SAT 50[b]	ILU 0.8[b]	ILU 0.9[b]	ILU 1.0[b]	Mean	SD[b]
GDR	0.00	0.00	0.00	0.03	0.06	0.08	0.11	0.02	0.02	0.02	0.03	0.04
TGR	0.00	0.02	0.60	0.03	0.24	0.00	0.15	0.00	0.00	0.00	0.10	0.18
HSM	0.00	0.03	0.02	0.05	0.13	0.02	0.52	0.00	0.16	0.00	0.09	0.15
THR	0.16	0.16	1.90	1.00	0.24	0.23	0.31	0.31	0.31	0.31	0.49	0.52
SFB	0.12	0.03	0.03	0.10	0.10	0.15	0.02	0.24	0.24	0.24	0.13	0.08
GNV	0.10	0.24	0.06	0.03	0.10	0.05	0.10	0.97	1.23	0.45	0.33	0.40
GLV	0.02	0.00	0.10	0.03	0.32	0.02	0.13	3.00	3.32	2.45	0.94	1.32
ICR	0.15	0.34	0.48	0.03	0.40	0.74	1.65	4.03	4.13	3.48	1.54	1.59
SD	2.47	2.06	1.48	0.40	0.11	0.42	0.31	2.56	3.02	2.56	1.54	1.07
SFM	0.11	0.08	0.13	1.02	0.34	0.15	0.03	0.18	0.15	0.18	0.24	0.27
VCR	0.29	0.98	1.16	0.10	0.73	0.32	0.34	0.47	0.85	0.21	0.55	0.34
VGR	3.63	4.16	3.87	0.10	0.27	0.11	0.10	2.37	0.73	0.71	1.60	1.63
EGR	0.48	0.90	2.87	1.06	0.13	0.10	0.08	1.03	0.32	0.39	0.74	0.80
SGR	0.11	1.87	1.89	1.82	0.23	0.27	0.55	0.73	0.76	0.77	0.90	0.67
EHS	0.21	0.18	0.27	0.55	0.71	0.60	0.98	1.06	1.94	0.84	0.73	0.50
MLP	0.60	0.58	0.79	4.16	0.74	0.50	0.44	0.39	0.23	0.39	0.88	1.11
SWC	0.29	0.98	1.16	0.10	0.73	0.32	0.34	0.47	0.85	0.21	0.55	0.34
DLP	1.15	1.23	1.34	3.08	0.39	0.02	0.98	0.76	0.11	0.76	0.98	0.82
VWC	0.87	1.21	0.19	3.37	0.56	0.18	0.49	0.47	0.10	0.47	0.79	0.92
ELP	0.31	1.27	2.39	3.69	0.27	0.27	0.18	0.31	0.23	0.32	0.92	1.14

[b]WPP denote accuracy without preprocessing. 2x2, 4x4 and 8x8 denote accuracy after median filtering with window size of 2x2, 4x4 and 8x8 respectively. SAT 25 and SAT 50 denotes the accuracy after increased saturation level of 25% and 50% respectively. ILU denote the performance after uneven illumination addition with maximum intensity value of 0.8, 0.9 and 1.0. SD denotes standard deviation in accuracies.

Table 3.12 False maximum (FM) differences of each focus measure function (FMF) without pre-processing and post-processing. Mean and standard deviation of these differences are provided in last two columns.

Methods[a]	2x2[b]	4x4[b]	8x8[b]	Noise	Cont	SAT 25[b]	SAT 50[b]	ILU 0.8[b]	ILU 0.9[b]	ILU 1.0[b]	Mean	SD[b]
GDR	0.00	0.00	0.00	0.00	0.03	0.00	0.00	0.03	0.03	0.03	0.01	0.02
TGR	0.03	0.03	0.00	0.00	0.03	0.03	0.03	0.03	0.03	0.03	0.03	0.01
HSM	0.17	0.38	0.55	0.10	0.10	0.14	0.10	0.17	0.17	0.17	0.21	0.14
THR	0.03	0.03	0.21	0.14	0.03	0.00	0.07	0.03	0.00	0.00	0.06	0.06
SFB	0.03	0.03	0.03	0.00	0.03	0.03	0.00	0.03	0.03	0.03	0.03	0.01
GNV	0.00	0.03	0.03	0.00	0.03	0.07	0.10	0.10	0.14	0.14	0.07	0.05
GLV	0.00	0.03	0.00	0.00	0.03	0.07	0.10	0.41	0.41	0.41	0.15	0.18
ICR	0.45	0.34	0.41	0.62	0.59	0.52	0.45	0.14	0.14	0.14	0.38	0.18
SD	0.28	0.17	0.21	0.03	0.07	0.10	0.14	0.45	0.45	0.45	0.23	0.15
SFM	0.03	0.24	0.45	0.17	0.17	0.31	0.24	0.31	0.28	0.28	0.25	0.10
VCR	0.17	0.55	0.31	0.00	0.41	0.17	0.07	1.38	2.28	1.03	0.64	0.69
VGR	0.24	0.24	0.24	0.03	0.10	0.00	0.03	4.38	1.03	0.79	0.71	1.27
EGR	0.03	0.21	0.21	0.07	0.10	0.03	0.07	0.21	0.10	0.03	0.11	0.07
SGR	0.03	0.66	2.00	0.03	0.03	0.03	0.14	2.45	0.83	0.34	0.66	0.83
EHS	0.00	0.03	0.03	0.10	0.00	0.00	0.07	0.03	0.10	0.10	0.05	0.04
MLP	0.14	0.14	0.24	0.10	0.03	0.07	0.14	0.03	0.07	0.03	0.10	0.06
SWC	0.10	0.14	0.21	0.14	0.03	0.03	0.10	0.03	0.03	0.00	0.08	0.06
DLP	0.17	0.55	0.31	0.00	0.41	0.17	0.07	1.38	2.28	1.03	0.64	0.69
VWC	0.28	0.00	0.07	0.41	0.34	0.28	0.24	0.31	0.28	0.59	0.28	0.16
ELP	0.10	0.07	0.24	0.10	0.83	0.07	0.07	1.62	1.10	1.41	0.56	0.59

[b]WPP denote accuracy without preprocessing. 2x2, 4x4 and 8x8 denote accuracy after median filtering with window size of 2x2, 4x4 and 8x8 respectively. SAT 25 and SAT 50 denotes the accuracy after increased saturation level of 25% and 50% respectively. ILU denote the performance after uneven illumination addition with maximum intensity value of 0.8, 0.9 and 1.0. SD denotes standard deviation in accuracies.

Finally, the full width at half maximum (FWHM) was calculated for top four FMFs (GDR, TGR, SFB and HSM) to find out their convergence rate to the best focus point (Fig. 3.9). In this study, GDR and SFB were rapidly converged to the best focus position, while HSM was slowest due to the marginal difference between the highest and the lowest focus measure values. An FMF is efficient for implementation in a real system when the manual intervention and the effect of different imaging conditions are minimal. Therefore, GDR, TGR, SFB and HSM are the most robust FMFs for high density (noisy) bright-field CM images, and these methods may be implemented in CM microscopes for automated capturing of images.
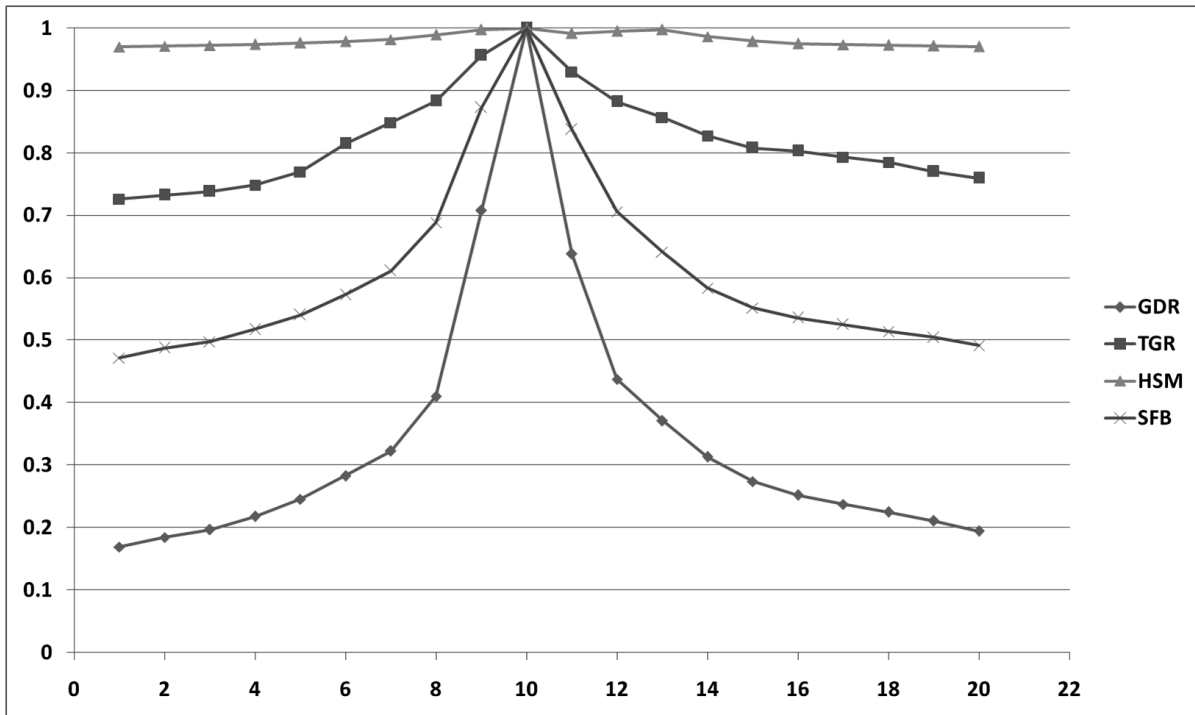
Fig. 3.9 Mean full width at half maximum (FWHM) of top four focus measure functions. FWHM values before and after DC offset removal: GDR = (2.68 (before DC removal), 2.53 (after DC Removal)), TGR = (5.35, 3.30), HSM = (6.72, 3.35) and SFB = (3.52, 3.27). Lesser DC offset value indicates the significance of an FMF. Lesser the FWHM value, better is the focus measure function.

3.4. Conclusion

Autfocusing using focus measure functions (FMFs) assists segmentation methods in segmenting bacilli more effectively. Studies have revealed that the performance of FMFs is sensitive to different imaging contents [100]. Therefore, the identification of robust and accurate FMFs for a particular imaging system assumes lots of significance for the development of auto-focusing instrument. A comprehensive analyses of 24 FMFs on diverse bright-field CM images provided GDR, TGR, SFB and HSM as the most robust and accurate FMFs. These FMFs can be used for the development of new automated conventional microscopy system which can capture an image directly from ZN stained sputum smear slide.

ESTABLISHMENT OF HYBRIDIZED FOCUS MEASURE FUNCTIONS AS UNIVERSAL METHOD FOR AUTO-FOCUSING

Summary

Exact focusing is essential for any automatic image capturing system. Performances of focus measure functions (FMFs) used for autofocusing are sensitive to image contents and imaging systems. Therefore, identification of universal FMF assumes a lot of significance. In this study, eight FMFs were hybridized in a pair of two and implemented simultaneously on a single stack to calculate the hybrid focus measure. In total, 28 hybrid FMFs (HFMFs) and eight FMFs were implemented on stacks of images from three different imaging modalities such as Ziehl-Neelsen stained sputum smear conventional microscope images (CM), Auramine-O stained fluorescent microscope images and multispectral images. Performance of FMFs was found to be the best at 50% region-sampling. Accuracy, focus error and false maximum were calculated to evaluate the performance of each FMFs. Nineteen HFMFs provided more than 90% accuracy. Image distortion (noise addition, contrast reduction, saturation increment and uneven illumination) were performed to evaluate robustness of HFMFs. Hybrid of Tenengrad variance and steerable filter based (VGRnSFB) HFMFs was identified as the most robust and accurate function with the accuracy of $\geq 90\%$ and relatively less focus error and false maximum rate. Sharpness of focus curve of the VGRnSFB along with eight individual FMFs was also computed for determining the efficacy of HFMF for optimization process. VGRnSFB HFMF can be implemented for automated capturing of an image for any imaging system.

4.1 Introduction

Automated focusing techniques were widely implemented in various optical imaging systems such as microscopes, industrial inspection tools and cameras [28, 98, 168, 169]. This technique determines the best focused image by analyzing the content of sequenced image of same view field acquired on different focal position. A focused image is defined as the best average focus over an entire view-field on a stack of images acquired at different focuses from a single view-field. The maximum value of the focus measure function (FMF) generally corresponds to the best focused image [97]. Studies have indicated that the performance of FMFs depend on image content which is broadly classified as higher, medium and lower density background [93, 102]. General images have low density background whereas images captured from different experiments such as conventional bright-field microscope (CM) have higher density background due to the presence of artifacts, dye to stain the bacteria, etc. Similarly, fluorescent microscope (FM) images have medium density background. Most of the FMFs efficiently work on visible optical system like commercial cameras, and have a higher accuracy rate due to the high resolution and sharp edges of visible image. However, it is difficult to obtain high accuracy rate for the infrared optical system (near infrared, thermal, etc.) due to the poor resolution, low contrast and blur edges in infrared images [95]. Studies have also indicated that the significantly better performing FMFs in fluorescence microscopy images produced average outcome in CM [103, 158, 159] and vice versa [29].

Several studies were performed to determine the efficient FMFs on microscopic (CM & FM) data, but most of their outcomes led to different conclusions [28, 29, 97, 98, 102]. Mateos-Pérez et al. found that mid-frequency discrete cosine transform (96.67%), Vollath's autocorrelation (VCR) (89%) and Tenengrad (TGR) (89%) were the efficient FMFs in FM images [98]. Six (Normalized gray-level variance (GNV), Brenner gradient (BGR), modified Laplacian (MLP), energy of Laplacian (ELP), VCR and TGR) and three (ELP, Gaussian derivative (GDR) and Variance of the log-histogram) were the most commonly used FMFs on Ziehl-Neelsen (ZN) stained sputum smear CM images [98, 102]. VCR and BGR were reported as the best FMFs in first study, while ELP was the best in the second. GNV, gray-level variance (GLV) and VCR were reported as the most efficient FMFs in bright-field pathological images [101]. Studies were also performed to determine the efficient FMFs on visible [98, 169-171] and infrared optical system [95, 172, 173]. Energy of Laplacian operator was the best FMF for visible and near-infrared images, while fast Hessian detector based FMF was the best in thermal spectrum [173].

72

Incorporation of automated methods in microscopy can increase the sensitivity and specificity by analyzing large number of view-fields [89]. Exact focusing is very crucial in any automatic microscopy system as performance of successive steps such as automatic object segmentation and classification depend on it [28]. Autofocusing is also very significant in developing consumer-level user friendly digital cameras which can capture high quality images with minimal user intervention [174].

To overcome inconsistent performances of FMFs, this study evaluated the performance of hybrid FMFs across the different modalities as well as to different imaging conditions (noise, saturation, etc.). Eight most common autofocus algorithms were hybridized by simultaneously implementing two FMFs on well versed datasets from three different modalities, namely CM, FM and multispectral (MS) images to identify the efficient hybrid FMFs for any imaging system. MS datasets contain diverse images from visible, near-infrared and thermal spectrum, and these datasets can be helpful to determine a robust and global hybrid FMF. The FMF algorithms incorporated in this study belong to three different categories according to their working principle. The changes in performances of hybrid FMFs were also analyzed after image distortion using noise addition, saturation increment, contrast reduction and uneven illumination to evaluate their effectiveness of this approach. The performance of every hybrid FMF is also compared with individual FMFs for better interpretation.

4.2 Material and Methods

4.2.1 Datasets

Three different image modalities containing 87 stacks of images were used to evaluate the performance of individual and hybrid focus measure functions. Three diverse data types covering ZN (CM), FM and multi-spectral (MS) images were used to evaluate hybrid FMFs. Detailed description for each imaging modalities are given below (Fig. 3.1).

(i). ZN Sputum Smear Microscopy

In total, thirty-one autofocusing stacks were extracted from Ziehl-Neelsen Sputum smear Microscopy image Database from http://14.139.240.55/znsm/index.php [175]. These stacks were prepared from ten different ZN-stained sputum smear slides of tuberculosis patient using three different microscopes. Each stack contains 20 images captured at different focus points over the same view-field (Fig. 4.1a). Acquired images were diverse as image contents

ranges from medium to high noisy background. Image contents also vary due to improper use of staining dye (over- and under-staining).

(ii). Fluorescent Sputum Smear Microscopy

In total, thirty-five autofocusing datasets, prepared from slides of 10 patients, were randomly extracted from http:// biig.uc3m.es/autofocus_stacks/ [98]. Every stack has 20 images that were acquired at different focus points over the same view-field (Fig. 4.1b).

(iii). Multi-Spectral (MS) Dataset

In total, twenty-one autofocusing datasets in visible, near-infrared and thermal spectrum were retrieved from http://splab.cz/en/download/databaze/multispec [173]. The images acquired in visible spectrum (VS) were divided into 7 sets where each set contains a stack of 12 images (Fig. 4.1c). Acquired objects in the VS include headphones, keyboard, keys, loudspeaker, mixer, sunglasses and guitar. The images acquired in near-infrared spectrum (IS) were divided into 7 sets where each set contains a stack of 21 images (Fig. 4.1d). Acquired objects in IS include building, car, corridor, head, keyboard, office desk and pens. The images acquired in thermal spectrum (TS) were divided into 7 sets where each set contains a stack of 27 images (Fig. 4.1e). Acquired objects in TS include building, circuit breaker, circuit, car engine, printer, server and tube.

4.2.2 Focus Measure Functions (FMFs)

Eight most common FMFs were included in this study as their performances in ZN (CM) and FM images were good [28, 98, 176]. Other FMFs such as Laplacian based operator, wavelet based operator, etc. were drastically failed on CM images; therefore, not included in the current study. These eight FMFs were hybridized and their performances were evaluated in this study to identify the best focused images from ZN, FM and MS images (Table 4.1). An FMF has highest value at the best focus position, and values reduce sequentially in both directions as focusing decreases (Fig. 3.2). These three major categories FMFs and their HFMFs were implemented in MATLAB (Table 4.1).

(i). Gradient-based FMFs

These functions assume that a well focused image have more high frequency content. Therefore, large intensity difference between neighboring pixels leading to sharper edges. Higher gradient represents more sharp edges; therefore, these FMFs use the gradient (first-order derivative) of the image to find the best focused image.

(ii). Statistics-based FMFs

These FMFs use various statistical measures like standard deviation, variance, autocorrelation, etc., to identify the best focused image. Generally, these FMFs are more consistent in high frequency noise as compared to derivative-based functions.

(iii). Other FMFs

This group contains the functions which are not in above two categories due to their working principles.
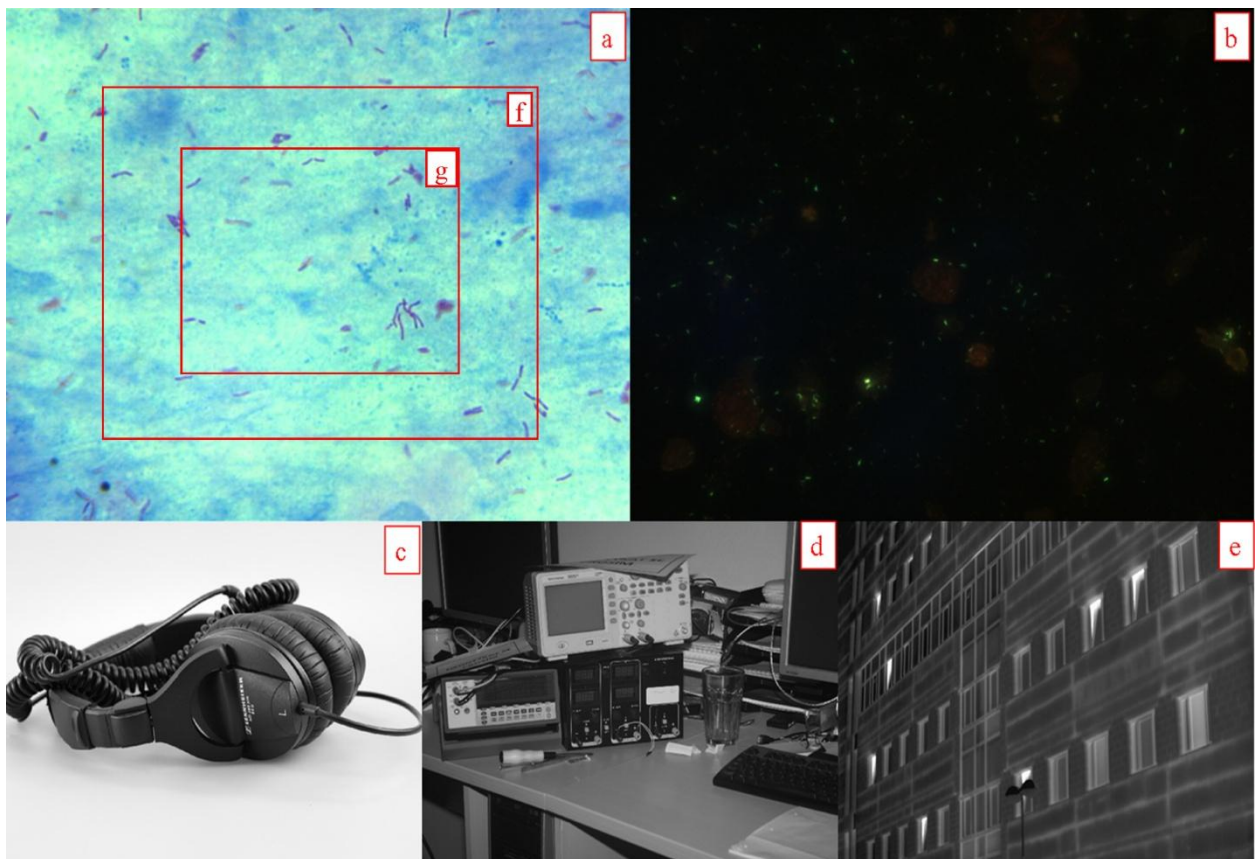
Fig. 4.1 Image modalities used to evaluate HFMFs. (a) Image acquired from ZN sputum smear conventional microscopy (CM), (b) Image acquired from sputum smear fluorescent microscopy (FM), (c) Image acquired in visible spectrum (VS), (d) Image acquired in near-infrared spectrum, (e) Image acquired in thermal spectrum (TS), (f) Depiction of the 50% region-sampled area, and (g) Depiction of the 25% region-sampled area used to evaluate focus measure functions

Table 4.1 Focus measure functions (FMFs) and their category used to form hybrid-FMF for identifying the best-focused images.

S. No.	Category	Focus Measure Function (FMF)	Reference
1.		Gaussian derivative (GDR)	[91]
2.	Gradient-based	Tenengrad (TGR)	[103]
3.		Tenengrad variance(VGR)	[99]
4.		Normalized gray-level variance (GNV)	[92]
5.	Statistics-based	Vollath's autocorrelation (VCR)	[103, 159]
6.		Hemli and Scherer's mean (HELM)	[167]
7.	Other	Steerable filters-based (SFB)	[168]
8.		Spatial frequency measure (SFM)	[96]

4.2.3 Hybridization

The above eight FMFs used in this study were hybridized in the pair of two, and a total of 28 combinations were obtained. Hybridization of FMFs means two FMFs are implemented simultaneously on a single stack to calculate the hybrid focus measure using following formula.

$$Hybrid\ FMF\ (HFMF) = \frac{FMF1 + FMF2}{2} \qquad (1)$$

Where, FMF1 and FMF2 are two focus measure functions which were used simultaneously. Hybrid focus measure is the average of two FMFs.

4.2.4 Region-sampling

Region-sampling was performed to implement FMFs on 25%, 50% and 75% parts of whole image. For 25% region-sampling, a total of 25% pixels from the central part of original image were retained. For example, with a 100x100 size (10000 pixels) image, 25 pixels from each end of rows and columns were removed to get the image of 50x50 dimensions (2500 pixels). The resultant image was sampled to 25% as the total numbers of pixels were reduced to the 1/4th of original image (Fig. 4.1g). Similarly, region-sampling of 50% (Fig. 1f) and 75% was performed. Region-sampling was performed to achieve better accuracy as well as to reduce computation time [93, 158].

4.2.5 Image Preprocessing

Poisson noise was added to check the robustness of HFMFs to noise. A MATLAB function 'immoise' is used to add Poisson noise generated from the image itself. Scaling factor 1e -10 is used for the significant effect of noise on image. In general, FMFs are more sensitive to the higher level of noise [98].

Saturation level of an image also alters the performance of FMFs . To check the efficacy of HFMFs with respect to increase in saturation level, ZN and FM images were converted to HSV (Hue, saturation and value) color space. Furthermore, saturation of HSV images was increased by 25% using MATLAB.

Reduced contrast level leads to smoothening of edges in images which reduces differentiation of the best focus image from defocused one. Contrast was reduced in preprocessing step to check the effectiveness of HFMF at low contrast level. Generally, better focused methods are not perturbed by low contrast which was reduced for every stack by mapping the image pixel values to a narrow range [100].

Uneven illumination was incorporated in images using a luminance gradient to test the effectiveness of HFMFs in low signal-to-noise ratio (SNR) condition due to poor illumination. Gray-scale image is used to represent luminance gradient using quadratic polynomial function, and it is multiplied to the original images to get resultant images.

4.2.6 Evaluation of focus measures

The following three criteria were used to evaluate the performance of FMFs and HFMFs [105].

Accuracy criterion: The accuracy value was assigned a score of 1, 0.5 or 0 if a stack was correctly classified; if the second best focus was classified as the best focus when the difference between the best and second best image differ marginally; or if the stack was misclassified respectively. Finally, the accuracy rate in percent was calculated using the following formula [28]:

$$\frac{\text{Sum of all score}}{\text{Total number of stacks}} \times 100 \qquad (2)$$

Higher score represents more accurate FMF/HFMF.

Focus error: It determines the difference between manually obtained and predicted best-focused image [98].

Number of false maxima: This criterion was used to calculate the number of false maximum produced by a HFMF or FMF. Number of maxima present in a sharpness curve of the FMF or HFMF excluding global maximum was determined [98].

4.2.7 Convergence rate of FMFs

Finally, *sharpness of focus curve* is used to identify the FMF and HFMFs with better convergence rate. It is used to calculate the narrowness of the peak. Narrower peak of FMF represents rapid convergence to the best focus point; hence, FMF would be implementable in the real system [173].

4.3 Results and Discussion

The ZN, FM and MS (VS, IS and TS) datasets are diverse in terms of image contents, and performances of FMFs were not consistent in these modalities [29, 173]. Therefore, this study proposed an autofocus system using hybrid focus measure function (HFMF) and assumed that some HFMFs could be robust across diverse image modalities as well as different imaging conditions (noise, saturation, etc.). The eight most commonly used FMFs that performed better in highly noisy ZN and FM images were hybridized and implemented.

4.3.1 Region-sampling and Hybridization of FMFs

Different parameters and configuration were checked prior to evaluate the performance of HFMFs. Images regions were sampled to 25%, 50% and 75% to check the accuracy of FMFs on different region-sampling rate in comparison to original images. Overall accuracy of most of the FMFs was reduced by 1-11% at 25% region-sampling, while it is increased by 1-4% at 50% and 75% region-sampled images (Fig. 4.2 and Table 4.2). HFMFs analyses were performed only on 50% region-sampled images as the result was optimal and mean computation time was minimal at this level. Improved performance of FMFs on 50% and 75% region-sampling might be due to better focusing on central part of the image than boundaries. Hybridization of two and three FMFs implemented on separate locations of the same view-field was evaluated, but performance of most of these FMFs was inconsistent and poor due to the different imaging contents. Therefore, the FMFs were superimposed on the same location of view field image to calculate the unbiased focus measure. Combination of three FMFs yields the poor accuracy in most of the
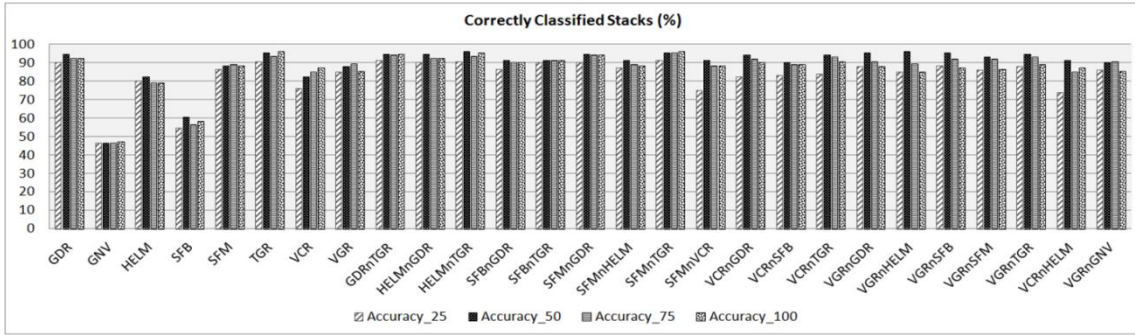
Fig. 4.2 Accuracy of focus measure functions (FMFs) in percent with different region-sampling data *i.e.* 25%, 50%, 75% and original imag

Table 4.2 Overall accuracy of focus measure function in percent with different sub-sampling data such as 25%, 50%, 75% and original image

Method[a]	Accuracy 25[b]	Accuracy 50[b]	Accuracy 75[b]	Accuracy 100[b]
GDR	90.1	94.8	92.4	92.4
GNV	46.5	46.5	46.5	47.1
HELM	80.2	82.6	79.1	79.1
SFB	54.7	60.5	56.4	58.1
SFM	86.6	88.4	89.0	88.4
TGR	90.7	95.3	93.6	95.9
VCR	76.2	82.6	84.9	87.2
VGR	84.9	87.8	89.5	85.5
GDRnTGR	91.3	94.8	94.2	94.8
HELMnGDR	90.1	94.8	92.4	92.4
HELMnTGR	90.7	95.9	93.6	95.3
SFBnGDR	86.6	91.3	90.1	90.1
SFBnTGR	90.1	91.3	91.3	91.3
SFMnGDR	90.1	94.8	94.2	94.2
SFMnHELM	87.2	91.3	89.0	88.4
SFMnTGR	91.3	95.3	95.3	95.9
SFMnVCR	75.0	91.3	88.4	88.4
VCRnGDR	82.6	94.2	91.9	90.1
VCRnSFB	83.1	90.1	89.0	89.0
VCRnTGR	83.7	94.2	93.0	90.7
VGRnGDR	87.8	95.3	90.7	87.8
VGRnHELM	84.9	95.9	89.5	84.9
VGRnSFB	88.4	95.3	91.9	87.2
VGRnSFM	86.0	93.0	91.9	86.6
VGRnTGR	87.8	94.8	93.0	89.0
VCRnHELM	73.8	91.3	84.9	87.2
VGRnGNV	86.0	90.1	90.7	85.5
GNVnGDR	81.4	88.4	86.6	88.4
GNVnTGR	81.4	87.8	89.5	90.1
VGRnVCR	82.0	86.6	91.9	88.4
GNVnVCR	74.4	80.2	84.9	83.7
SFMnSFB	72.1	73.3	71.5	72.1
SFMnGNV	64.0	65.7	62.2	62.8
SFBnHELM	59.9	63.4	59.9	58.1
GNVnSFB	59.3	61.6	57.6	55.8
GNVnHELM	50.6	51.7	48.3	48.3

[b]25, 50, 75 and 100 are image sub-sampling rates in percent.

HFMFs, while combinations of two FMFs have provided a better accuracy rate. Therefore, only two FMFs were superimposed and used as final configuration. Performances of HFMFs were evaluated on overall datasets as well as separately on three types of datasets (ZN, FM & MS) to determine the effect of different imaging modalities on HFMFs. ZN datasets also contain microscopic images captured from Smartphone camera to evaluate the performance of HFMFs. All the FMFs used in this study were implemented on MATLAB and evaluated on unbiased approach. Mean computational time taken by each autofocus function was determined on Intel® Core™ i3-3220 CPU at 3.30 GHz with eight GB RAM (Table 4.3). The performance of HFMFs before and after preprocessing is provided in the following sections.

Table 4.3 Mean computation time (in second) per stack of eight focus measure functions at 50% region-sampling. Original Images were of 1600x1200 dimensions.

FMFs[a]	Mean Time (Sec.)
GDR	0.76
GNV	0.17
HELM	0.97
SFB	3.37
SFM	0.49
TGR	0.41
VCR	0.4
VGR	0.58

4.3.2 Without image preprocessing

Average performances of thirty-six (eight individual and twenty-eight HFMFs) FMFs were computed separately on each datasets at different region-sampling rate (Fig. 4.2). More than 90% overall accuracy at 50% region-sampling was obtained using nineteen HFMFs which indicated that HFMFs were consistent w.r.t different imaging modalities (Fig. 4.3a, Table 4.4). Focus error and false maximum rate of these twenty-seven FMFs (eight individual and nineteen HFMFs) were also computed to validate the analysis. Most of these HFMFs performed accurately, and had less focus errors (Fig. 4.3b, Table 4.4) and false maximums (Fig. 4.3c, Table 4.4) whereas most of the individual FMFs provided the accuracy < 90%, with higher focus error and false maximum (except GDR & TGR). HELMnTGR, SFMnTGR, VGRnGDR, VGRnHELM and VGRnSFB hybrid FMFs obtained more than 95% accuracy and outperformed most of the individual FMFs.
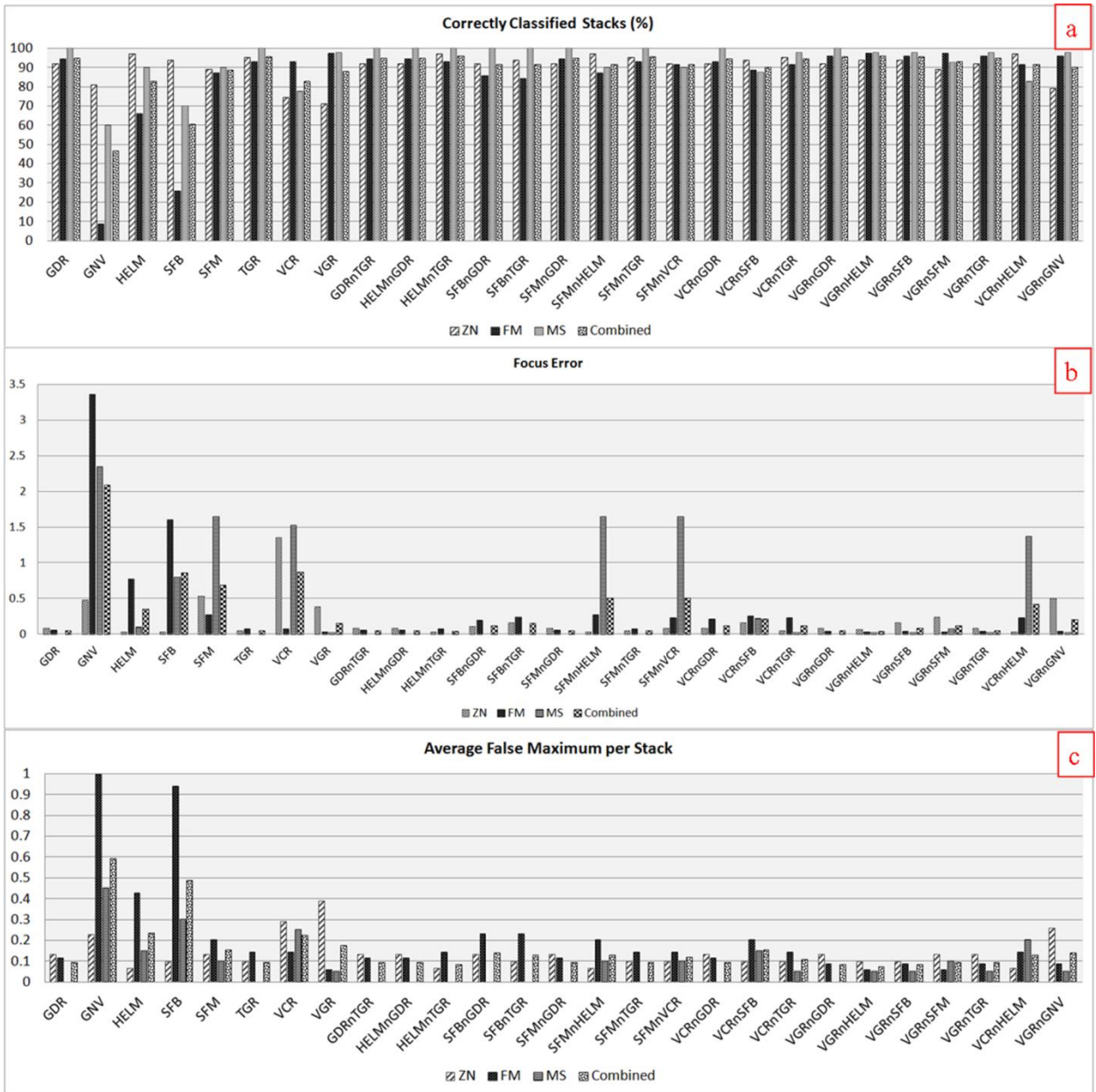
Fig. 4.3 Performances of FMFs and HFMFs without image preprocessing in 50% region-sampling data. (a) Accuracy in percent, (b) Focus error, and (c) False maximum

Table 4.4 Accuracy in percent, focus error and false maximums of focus measure function without preprocessing at 50% sub-sampling

Method[a]	Accuracy				Focus Error				False Maximum			
	ZN[b]	FM[b]	MS[b]	Combined	ZN	FM	MS	Combined	ZN	FM	MS	Combined
GDR	91.9	94.3	100.0	94.8	0.08	0.06	0.00	0.05	0.13	0.11	0.00	0.09
GNV	80.6	8.6	60.0	46.5	0.48	3.36	2.35	2.09	0.23	1.00	0.45	0.59
HELM	96.8	65.7	90.0	82.6	0.03	0.77	0.10	0.35	0.06	0.43	0.15	0.23
SFB	93.5	25.7	70.0	60.5	0.03	1.60	0.80	0.86	0.10	0.94	0.30	0.49
SFM	88.7	87.1	90.0	88.4	0.53	0.27	1.65	0.69	0.13	0.20	0.10	0.15
TGR	95.2	92.9	100.0	95.3	0.05	0.07	0.00	0.05	0.10	0.14	0.00	0.09
VCR	74.2	92.9	77.5	82.6	1.35	0.07	1.53	0.87	0.29	0.14	0.25	0.22
VGR	71.0	97.1	97.5	87.8	0.39	0.03	0.03	0.16	0.39	0.06	0.05	0.17
GDRnTGR	91.9	94.3	100.0	94.8	0.08	0.06	0.00	0.05	0.13	0.11	0.00	0.09
HELMnGDR	91.9	94.3	100.0	94.8	0.08	0.06	0.00	0.05	0.13	0.11	0.00	0.09
HELMnTGR	96.8	92.9	100.0	95.9	0.03	0.07	0.00	0.04	0.06	0.14	0.00	0.08
SFBnGDR	91.9	85.7	100.0	91.3	0.11	0.20	0.00	0.12	0.13	0.23	0.00	0.14
SFBnTGR	93.5	84.3	100.0	91.3	0.16	0.24	0.00	0.16	0.10	0.23	0.00	0.13
SFMnGDR	91.9	94.3	100.0	94.8	0.08	0.06	0.00	0.05	0.13	0.11	0.00	0.09
SFMnHELM	96.8	87.1	90.0	91.3	0.03	0.27	1.65	0.51	0.06	0.20	0.10	0.13
SFMnTGR	95.2	92.9	100.0	95.3	0.05	0.07	0.00	0.05	0.10	0.14	0.00	0.09
SFMnVCR	91.9	91.4	90.0	91.3	0.08	0.23	1.65	0.51	0.10	0.14	0.10	0.12
VCRnGDR	91.9	92.9	100.0	94.2	0.08	0.21	0.00	0.12	0.13	0.11	0.00	0.09
VCRnSFB	93.5	88.6	87.5	90.1	0.16	0.26	0.23	0.22	0.10	0.20	0.15	0.15
VCRnTGR	95.2	91.4	97.5	94.2	0.05	0.23	0.03	0.12	0.10	0.14	0.05	0.10
VGRnGDR	91.9	95.7	100.0	95.3	0.08	0.04	0.00	0.05	0.13	0.09	0.00	0.08
VGRnHELM	93.5	97.1	97.5	95.9	0.06	0.03	0.03	0.04	0.10	0.06	0.05	0.07
VGRnSFB	93.5	95.7	97.5	95.3	0.16	0.04	0.03	0.08	0.10	0.09	0.05	0.08
VGRnSFM	88.7	97.1	92.5	93.0	0.24	0.03	0.08	0.12	0.13	0.06	0.10	0.09
VGRnTGR	91.9	95.7	97.5	94.8	0.08	0.04	0.03	0.05	0.13	0.09	0.05	0.09
VCRnHELM	96.8	91.4	82.5	91.3	0.03	0.23	1.38	0.42	0.06	0.14	0.20	0.13
VGRnGNV	79.0	95.7	97.5	90.1	0.50	0.04	0.03	0.20	0.26	0.09	0.05	0.14

[b]ZN (Ziehl-Neelsen sputum smear conventional microscope), FM (fluorescent microscope) and MS (multispectral datasets). 25, 50, 75 and 100 are image sub-sampling rates in percent.

4.3.3 Image preprocessing

Effectiveness of HFMFs to different imaging conditions is very important because the occurrence of noise, poor contrast, illumination, etc. may affect its performance. Poisson noise addition, saturation level increment, contrast reduction and uneven illumination were incorporated to find out the effect of image distortion on FMFs and HFMFs performance.

In the first step, Poisson noise was added to all the images. Generally, higher level of noise in an image significantly affects the performance [98, 100]. Most of the HFMFs were more robust than individual FMFs after noise addition (Fig. 4.4, Table 4.5). GDR and TGR

FMFs produced higher accuracies in focused image identification but failed drastically after noise addition (Fig. 4.4a). GDR FMF accuracies were dropped to 25.8, 67.1 and 65 percent for ZN, FM and MS datasets, respectively. Similarly, the TGR accuracies were dropped to 90, 30 and 80 percent for the above datasets after noise addition. Focus error (Fig. 4.4b) and false maximums (Fig. 4.4c) rate were also increased in above two individual FMFs. VGRnSFB HFMF was least affected by noise addition and outperformed all the individual FMFs in terms of accuracy, focus error and false maxima, whereas VGRnGNV HFMF was ranked 2nd after noise addition (Fig. 4.4a).
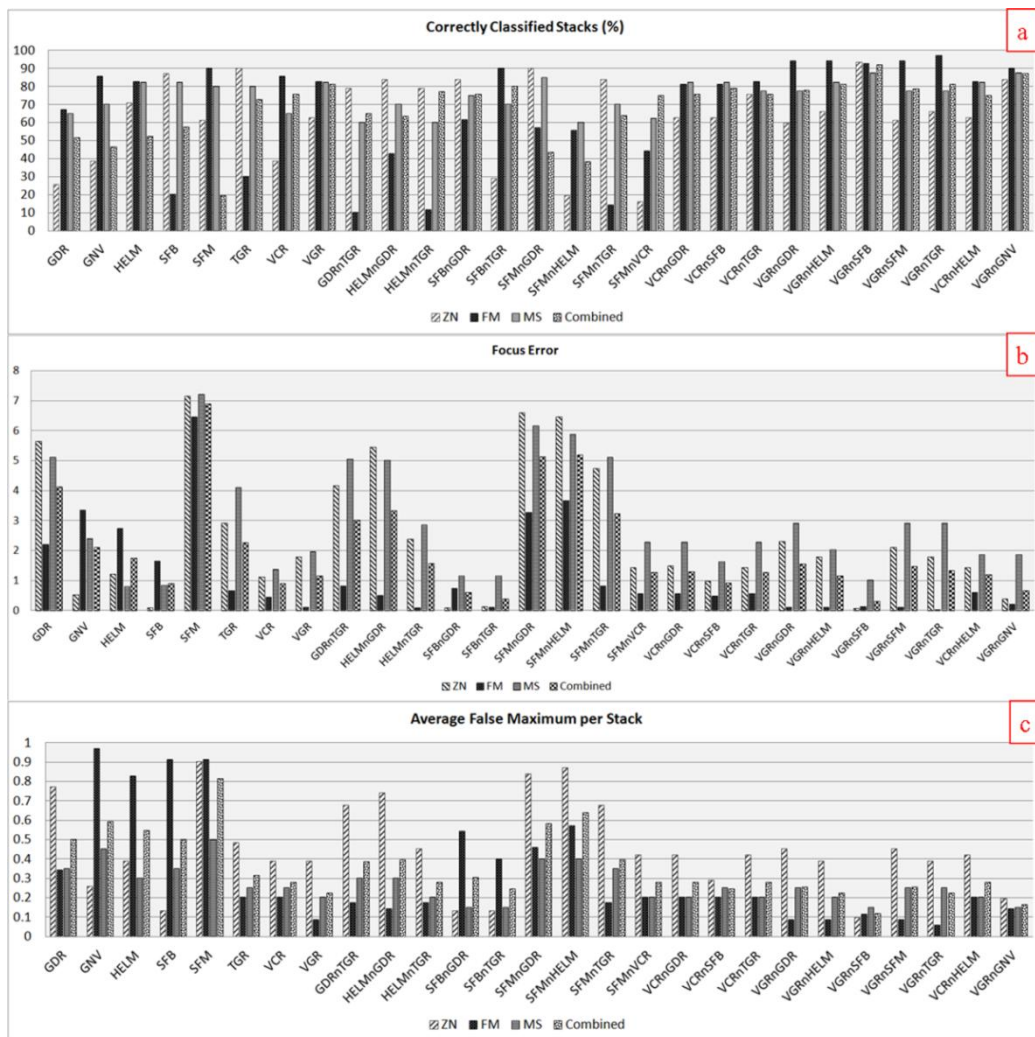
Fig. 4.4 Performances of FMFs and HFMFs after noise addition in 50% region-sampling data. (a) Accuracy in percent, (b) Focus error and (c) False maximum

Table 4.5 Accuracy in percent, focus error and false maximums of focus measure function after noise addition in 50% sub-sampling image data

Method[a]	Accuracy				Focus Error				False Maximum			
	ZN[b]	FM[b]	MS[b]	Combined	ZN	FM	MS	Combined	ZN	FM	MS	Combined
GDR	25.8	67.1	65.0	51.7	5.65	2.21	5.10	4.12	0.13	0.11	0.35	0.17
GNV	38.7	85.7	70.0	46.5	0.53	3.36	2.40	2.12	0.19	1.00	0.50	0.59
HELM	71.0	82.9	82.5	52.3	1.23	2.74	0.80	1.74	0.10	0.54	0.35	0.34
SFB	87.1	20.0	82.5	57.6	0.10	1.66	0.84	0.90	0.13	0.94	0.30	0.50
SFM	61.3	90.0	80.0	19.2	7.15	6.46	7.20	6.88	0.13	0.14	0.50	0.22
TGR	90.3	30.0	80.0	72.7	2.92	0.66	4.10	2.27	0.10	0.11	0.25	0.14
VCR	38.7	85.7	65.0	75.6	1.11	0.46	1.38	0.91	0.16	0.14	0.30	0.19
VGR	62.9	82.9	82.5	81.4	1.79	0.11	1.98	1.15	0.32	0.06	0.20	0.19
GDRnTGR	79.0	10.0	60.0	65.1	4.16	0.83	5.05	3.01	0.13	0.11	0.30	0.16
HELMnGDR	83.9	42.9	70.0	63.4	5.45	0.50	5.00	3.33	0.13	0.11	0.30	0.16
HELMnTGR	79.0	11.4	60.0	77.3	2.39	0.10	2.85	1.56	0.10	0.11	0.20	0.13
SFBnGDR	83.9	61.4	75.0	75.6	0.10	0.74	1.15	0.60	0.13	0.29	0.15	0.20
SFBnTGR	29.0	90.0	70.0	80.2	0.13	0.11	1.15	0.38	0.06	0.26	0.15	0.16
SFMnGDR	90.3	57.1	85.0	43.6	6.58	3.27	6.15	5.13	0.13	0.11	0.35	0.17
SFMnHELM	19.4	55.7	60.0	38.4	6.45	3.67	5.88	5.19	0.10	0.23	0.35	0.21
SFMnTGR	83.9	14.3	70.0	64.0	4.74	0.83	5.10	3.23	0.10	0.11	0.35	0.16
SFMnVCR	16.1	44.3	62.5	75.0	1.44	0.56	2.28	1.27	0.16	0.11	0.25	0.16
VCRnGDR	62.9	81.4	82.5	75.6	1.50	0.57	2.28	1.30	0.23	0.11	0.15	0.16
VCRnSFB	62.9	81.4	82.5	79.1	0.98	0.49	1.63	0.93	0.13	0.23	0.25	0.20
VCRnTGR	75.8	82.9	77.5	75.6	1.44	0.57	2.28	1.28	0.19	0.11	0.20	0.16
VGRnGDR	59.7	94.3	77.5	77.9	2.31	0.11	2.93	1.56	0.23	0.06	0.25	0.16
VGRnHELM	66.1	94.3	82.5	81.4	1.79	0.11	2.03	1.16	0.32	0.06	0.20	0.19
VGRnSFB	93.5	92.9	87.5	91.9	0.06	0.13	1.03	0.31	0.19	0.06	0.10	0.12
VGRnSFM	61.3	94.3	77.5	78.5	2.10	0.11	2.93	1.48	0.32	0.06	0.25	0.20
VGRnTGR	66.1	97.1	77.5	81.4	1.79	0.03	2.93	1.34	0.19	0.06	0.25	0.15
VCRnHELM	62.9	82.9	82.5	75.0	1.44	0.61	1.88	1.20	0.19	0.14	0.25	0.19
VGRnGNV	83.9	90.0	87.5	87.2	0.39	0.21	1.88	0.66	0.32	0.09	0.20	0.20

[b]ZN (Ziehl-Neelsen sputum smear conventional microscope), FM (fluorescent microscope) and MS (multispectral datasets).

In the second step, the saturation was increased by 25% in all images. Generally, performance of all FMFs decreases as the saturation level increases [100]. On MS datasets, GDR and TGR have shown the poor accuracy rate of 65% and 75%, respectively. The performances of most of the HFMFs were better than individual FMFs after increased saturation level. The performance of VGRnSFB HFMF was altered slightly and shown highest accuracy rate with less focus error and false maxima (Fig. 4.5, Table 4.6).
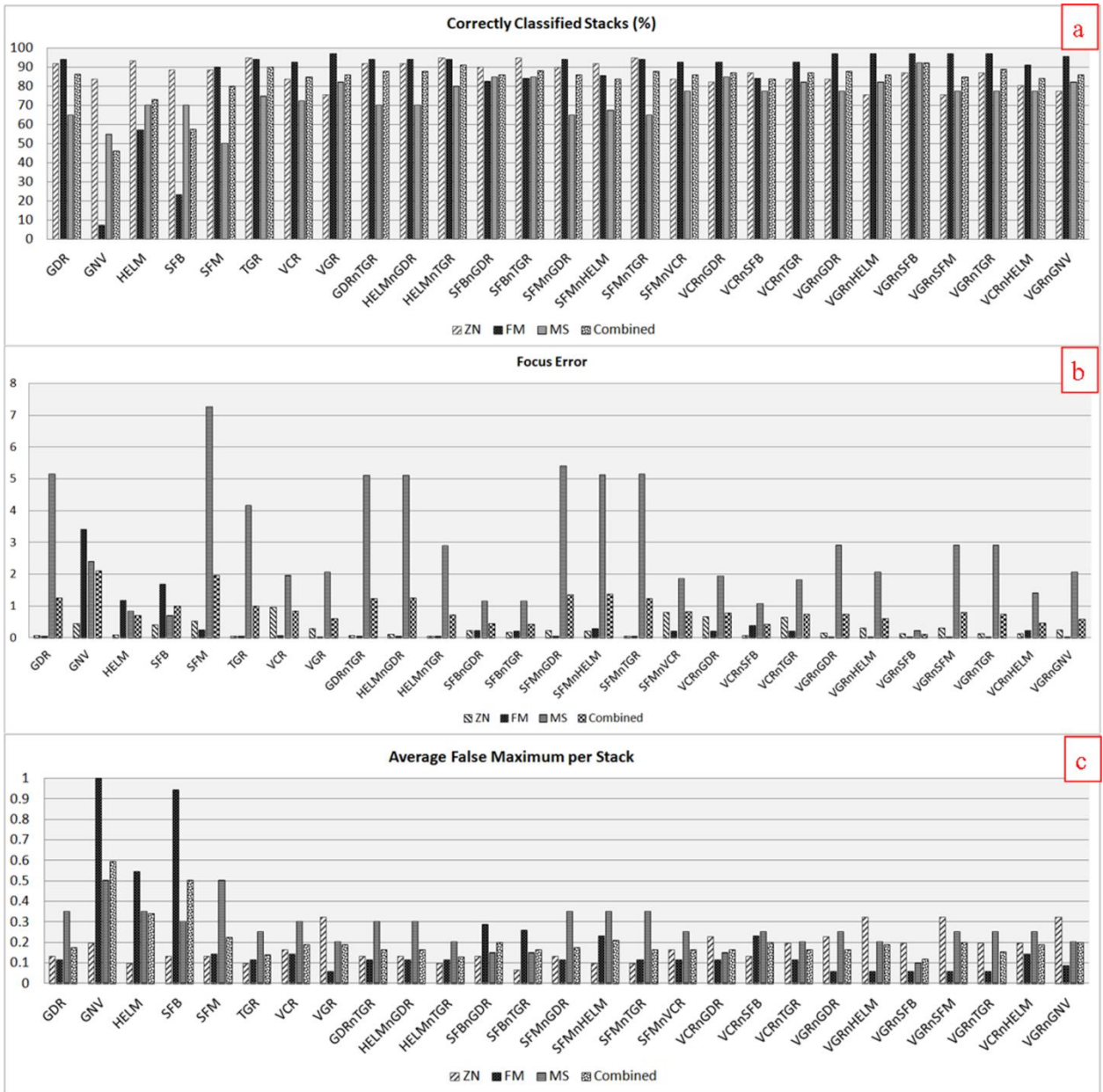
Fig. 4.5 Performances of FMFs and HFMFs after 25% saturation increment in 50% region-sampling data. (a) Accuracy in percent, (b) Focus error and (c) False maximum

Table 4.6 Accuracy in percent, focus error and false maximums of focus measure function after increased saturation in 50% sub-sampling data.

Method[a]	Accuracy				Focus Error				False Maximum			
	ZN[b]	FM[b]	MS[b]	Combined	ZN	FM	MS	Combined	ZN	FM	MS	Combined
GDR	91.9	94.3	65.0	86.6	0.08	0.06	5.15	1.25	0.13	0.11	0.35	0.17
GNV	83.9	7.1	55.0	45.9	0.45	3.41	2.40	2.11	0.19	1.00	0.50	0.59
HELM	93.5	57.1	70.0	73.3	0.10	1.17	0.85	0.71	0.10	0.54	0.35	0.34
SFB	88.7	22.9	70.0	57.6	0.40	1.69	0.70	0.99	0.13	0.94	0.30	0.50
SFM	88.7	90.0	50.0	80.2	0.53	0.24	7.25	1.98	0.13	0.14	0.50	0.22
TGR	95.2	94.3	75.0	90.1	0.05	0.06	4.15	1.01	0.10	0.11	0.25	0.14
VCR	83.9	92.9	72.5	84.9	0.97	0.07	1.98	0.84	0.16	0.14	0.30	0.19
VGR	75.8	97.1	82.5	86.0	0.29	0.03	2.08	0.60	0.32	0.06	0.20	0.19
GDRnTGR	91.9	94.3	70.0	87.8	0.08	0.06	5.10	1.24	0.13	0.11	0.30	0.16
HELMnGDR	91.9	94.3	70.0	87.8	0.11	0.06	5.10	1.25	0.13	0.11	0.30	0.16
HELMnTGR	95.2	94.3	80.0	91.3	0.05	0.06	2.90	0.72	0.10	0.11	0.20	0.13
SFBnGDR	90.3	82.9	85.0	86.0	0.23	0.23	1.15	0.44	0.13	0.29	0.15	0.20
SFBnTGR	95.2	84.3	85.0	88.4	0.18	0.21	1.15	0.42	0.06	0.26	0.15	0.16
SFMnGDR	90.3	94.3	65.0	86.0	0.23	0.06	5.40	1.36	0.13	0.11	0.35	0.17
SFMnHELM	91.9	85.7	67.5	83.7	0.21	0.29	5.13	1.38	0.10	0.23	0.35	0.21
SFMnTGR	95.2	94.3	65.0	87.8	0.05	0.06	5.15	1.24	0.10	0.11	0.35	0.16
SFMnVCR	83.9	92.9	77.5	86.0	0.81	0.21	1.88	0.81	0.16	0.11	0.25	0.16
VCRnGDR	82.3	92.9	85.0	87.2	0.66	0.21	1.95	0.78	0.23	0.11	0.15	0.16
VCRnSFB	87.1	84.3	77.5	83.7	0.08	0.39	1.08	0.44	0.13	0.23	0.25	0.20
VCRnTGR	83.9	92.9	82.5	87.2	0.65	0.21	1.83	0.74	0.19	0.11	0.20	0.16
VGRnGDR	83.9	97.1	77.5	87.8	0.16	0.03	2.93	0.75	0.23	0.06	0.25	0.16
VGRnHELM	75.8	97.1	82.5	86.0	0.31	0.03	2.08	0.60	0.32	0.06	0.20	0.19
VGRnSFB	87.1	97.1	92.5	92.4	0.13	0.03	0.23	0.11	0.19	0.06	0.10	0.12
VGRnSFM	75.8	97.1	77.5	84.9	0.31	0.03	2.93	0.80	0.32	0.06	0.25	0.20
VGRnTGR	87.1	97.1	77.5	89.0	0.13	0.03	2.93	0.74	0.19	0.06	0.25	0.15
VCRnHELM	80.6	91.4	77.5	84.3	0.13	0.23	1.43	0.47	0.19	0.14	0.25	0.19
VGRnGNV	77.4	95.7	82.5	86.0	0.26	0.04	2.08	0.59	0.32	0.09	0.20	0.20

[b]ZN (Ziehl-Neelsen sputum smear conventional microscope), FM (fluorescent microscope) and MS (multispectral datasets).

In third step, the contrasts of all images were reduced using "*imadjust*" function of MATLAB. Generally, marginal reduction of contrast has no effects on FMFs performance [91, 100]. Performance of all the HFMFs were affected marginally and accuracies were slightly dropped by contrast reduction (Fig. 4.6, Table 4.7). GDRnTGR, HELMnGDR, HELMnTGR, SFMnGDR and SFMnTGR methods achieved >94% overall accuracy. VGRnSFB remained consistent to reduced contrast level and obtained an overall accuracy of 91.3%.
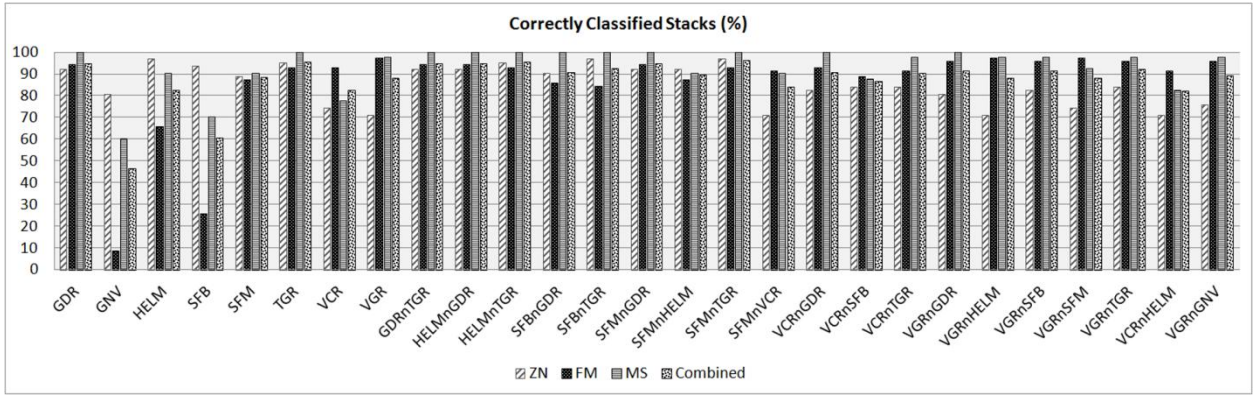
Fig. 4.6 Accuracy of FMFs and HFMFs in percent after contrast reduction in 50% region-sampling data.

Table 4.7 Accuracy in percent of focus measure function after contrast reduction in 50% sub-sampling

Method[a]	ZN[b]	FM[b]	MS[b]	Combined
GDR	91.9	94.3	100.0	94.8
GNV	80.6	8.6	60.0	46.5
HELM	96.8	65.7	90.0	82.6
SFB	93.5	25.7	70.0	60.5
SFM	88.7	87.1	90.0	88.4
TGR	95.2	92.9	100.0	95.3
VCR	74.2	92.9	77.5	82.6
VGR	71.0	97.1	97.5	87.8
GDRnTGR	91.9	94.3	100.0	94.8
HELMnGDR	91.9	94.3	100.0	94.8
HELMnTGR	95.2	92.9	100.0	95.3
SFBnGDR	90.3	85.7	100.0	90.7
SFBnTGR	96.8	84.3	100.0	92.4
SFMnGDR	91.9	94.3	100.0	94.8
SFMnHELM	91.9	87.1	90.0	89.5
SFMnTGR	96.8	92.9	100.0	95.9
SFMnVCR	71.0	91.4	90.0	83.7
VCRnGDR	82.3	92.9	100.0	90.7
VCRnSFB	83.9	88.6	87.5	86.6
VCRnTGR	83.9	91.4	97.5	90.1
VGRnGDR	80.6	95.7	100.0	91.3
VGRnHELM	71.0	97.1	97.5	87.8
VGRnSFB	82.3	95.7	97.5	91.3
VGRnSFM	74.2	97.1	92.5	87.8
VGRnTGR	83.9	95.7	97.5	91.9
VCRnHELM	71.0	91.4	82.5	82.0
VGRnGNV	75.8	95.7	97.5	89.0

[b]ZN (Ziehl-Neelsen sputum smear conventional microscope), FM (fluorescent microscope) and MS (multispectral datasets).

Uneven illumination has very little effect on performance of FMFs in FM images, while in some cases performance has been improved [98]. Uneven illumination was incorporated in all the images. Most of the HFMFs have shown relatively consistent performance and have marginal changes in accuracy (Fig. 4.7, Table 4.8).
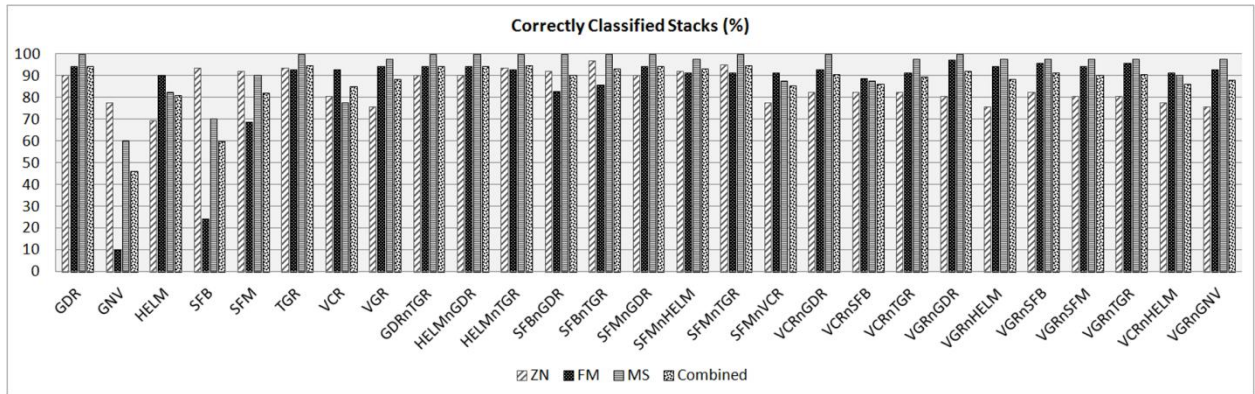
Fig. 4.7 Accuracy of FMFs and HFMFs in percent after uneven illumination in 50% region-sampling data.

Evaluation of FMFs and HFMFS in various imaging conditions (such as without preprocessing, noise addition, saturation increment, etc.) shows that VGRnSFB HFMF was the most robust and accurate focus function with overall accuracy >90%, less focus error and false maxima.

Table 4.8 Accuracy in percent of focus measure function after uneven illumination at 50% sub-sampling data.

Method[a]	ZN[b]	FM[b]	MS[b]	Combined
GDR	90.3	94.3	100.0	94.2
GNV	77.4	10.0	60.0	45.9
HELM	69.4	90.0	82.5	80.8
SFB	93.5	24.3	70.0	59.9
SFM	91.9	68.6	90.0	82.0
TGR	93.5	92.9	100.0	94.8
VCR	80.6	92.9	77.5	84.9
VGR	75.8	94.3	97.5	88.4
GDRnTGR	90.3	94.3	100.0	94.2
HELMnGDR	90.3	94.3	100.0	94.2
HELMnTGR	93.5	92.9	100.0	94.8
SFBnGDR	91.9	82.9	100.0	90.1
SFBnTGR	96.8	85.7	100.0	93.0
SFMnGDR	90.3	94.3	100.0	94.2
SFMnHELM	91.9	91.4	97.5	93.0
SFMnTGR	95.2	91.4	100.0	94.8
SFMnVCR	77.4	91.4	87.5	85.5
VCRnGDR	82.3	92.9	100.0	90.7
VCRnSFB	82.3	88.6	87.5	86.0
VCRnTGR	82.3	91.4	97.5	89.5
VGRnGDR	80.6	97.1	100.0	91.9
VGRnHELM	75.8	94.3	97.5	88.4
VGRnSFB	82.3	95.7	97.5	91.3
VGRnSFM	80.6	94.3	97.5	90.1
VGRnTGR	80.6	95.7	97.5	90.7
VCRnHELM	77.4	91.4	90.0	86.0
VGRnGNV	75.8	92.9	97.5	87.8

[b]ZN (Ziehl-Neelsen sputum smear conventional microscope), FM (fluorescent microscope) and MS (multispectral datasets).

4.3.4 Discussion

Main objective of this study was to propose the most accurate robust hybrid focus measure function (HFMF) applicable to all the imaging modalities. Eight FMFs were earlier implemented in different applications such as shape-from-focus on images of commercial cameras and synthetic image sequences with clear edges and patters [100]. Pertuz et al. found that Laplacian based operators were outperformed when preprocessing was not applied [100]. Mateos-Pérez et al. established that mid-frequency discrete cosine transform (96.67%), VCR (89%) and TGR (89%) FMFs were performed better in FM images [98]. VCR, BGR and ELP were reported as the best FMFs in CM [28]. None of the previously reported FMFs were consistent to diverse imaging modalities such as ZN, FM and MS images. These

inconsistencies of results have emphasized the importance of robust HFMFs that may capture focused images automatically irrespective of imaging system.

The performances of thirty-six (twenty-eight hybrid and eight individual) HFMFs were evaluated on the datasets covering almost all diverse image contents with high, medium and low density backgrounds and lack of sharp edges in images. Initially, nineteen HFMFs have provided overall accuracy rate ≥90%. VGRnSFB HFMF has been identified as the most robust and consistent after evaluating performance in different imaging conditions such as noise addition, contrast reduction, saturation increment and uneven illumination. An efficient HFMF has lots of application potential as it is easier to implement when intervention of preprocessing and other requirements are minimal. Better performance of VGRnSFB is significant as there was no HFMF reported earlier robust to ZN, FM and MS images simultaneously.

Finally, the sharpness of focus curve was evaluated for eight individual FMFs (GDR, GNV, HELM, SFB, SFM, TGR, VCR and VGR) and a HFMF (VGRnSFB). In this study, VGRnSFB, VGR and SFB were rapidly converged to the best focus position (Fig. 4.8). Though sharpness curve of VGR was better, VGRnSFB HFMF curve was comparable to it and found to be suitable for implementation in real systems. This HFMF has also produced comparable sharpness curve in MS images (Fig. 4.9).
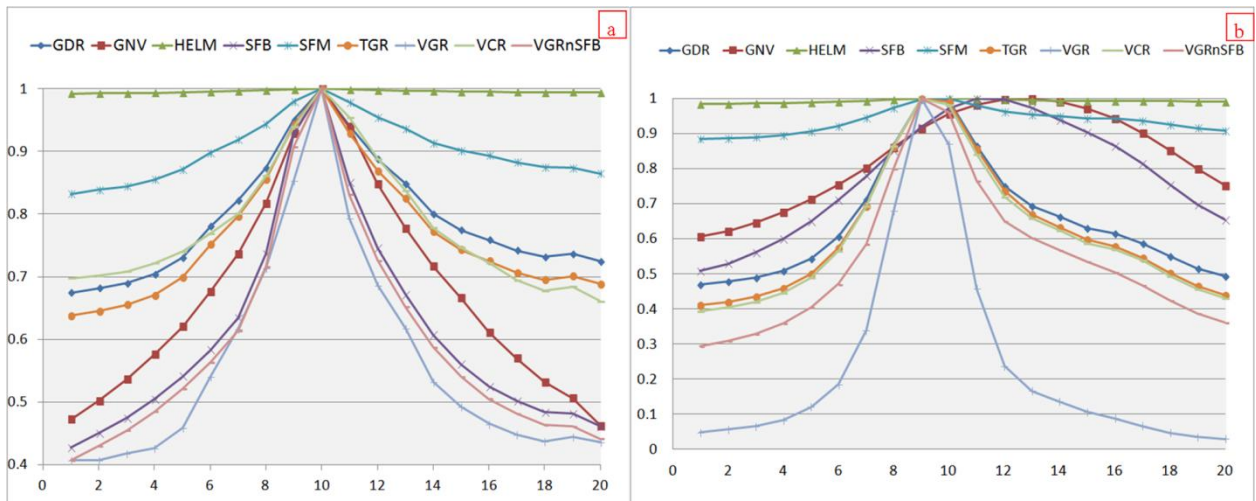
Fig. 4.8 Sharpness curve of nine focus measure functions including hybrid FMF (VGRnSFB). Narrow peak represents rapid convergence of focus measure function. (a) VGRnSFB (HFMF), VGR and SFB were rapidly converged to the best focus position in ZN (CM) images, and (b) VGRnSFB and VGR were rapidly converged to the best focus position in FM images.

90
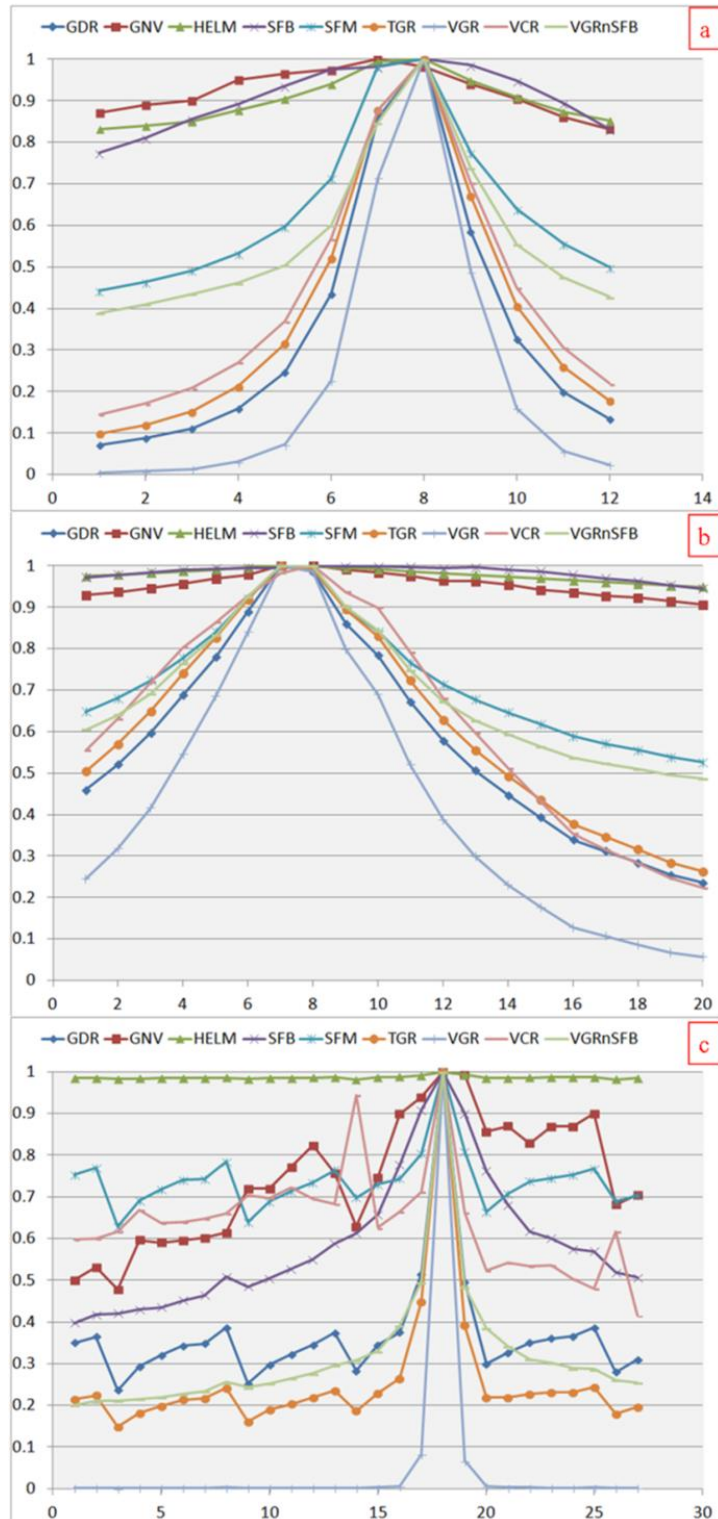
Fig. 4.9 Sharpness curve of nine focus measure functions including VGRnSFB HFMF on MS datasets. Narrow peak represents rapid convergence of focus measure function. (a) Sharpness curve on headphones images of visible spectrum, (b) Sharpness curve on headphones building images of near-infrared spectrum, and (c) Sharpness curve on breaker images of thermal spectrum.

4.4 Conclusion

Exact autofocusing using focus measure functions (FMFs) is very crucial step of any imaging system. Studies have reported that the performance of FMFs is sensitive to image contents [100]. Therefore, efficient and robust FMFs are significant in any imaging system for the development of automated instrument. A comprehensive analysis of twenty-eight hybrid FMFs on diverse datasets, spanning almost all image categories, provided nineteen hybrid methods with accuracy >90%. Effectiveness of these HFMFs was tested under different imaging conditions such as noise addition, saturation increment, contrast reduction and uneven illumination. VGRnSFB was found to be the most robust and accurate HFMF as it showed the best overall accuracy and robustness as the performances were independent to different image distortions. This HFMF may be implemented in any imaging system which can capture the best focused image automatically.

AUTOMATIC DETECTION AND CLASSIFICATION OF *MYCOBACTERIUM TUBERCULOSIS* BACILLI FROM ZN-STAINED SPUTUM SMEAR IMAGES USING WATERSHED SEGMENTATION

Summary

Manual identification and counting of bacilli using sputum smear microscopy (CM) is very time consuming, labor intensive and tedious work. As a result, the sensitivity of TB detection varies and relies on experience of microbiologists which leads to misdiagnosis 33–50% of active cases. These issues can be addressed using automated method which reported to increase the sensitivity and specificity of TB detection. In this Chapter, an automated method for detection and classification of bacilli using watershed segmentation is presented. The efficacy of this algorithm to detect distinct bacilli from overlapping/occluded ones was also evaluated. Several preprocessing techniques were implemented prior to watershed segmentation for removal of artifacts and objects larger or smaller than bacilli. Performance of this segmentation on different infection levels were tested and discussed in this chapter. This method has achieved the better sensitivity and specificity on higher infection level for classifying an image as TB positive or negative. The proposed method is very significant in detecting bacilli even for challenging images with unclear and overlapped bacilli.

5.1 Introduction

According to world health organization (WHO), tuberculosis (TB) is one of the primary causes of death worldwide by an infectious agent [27]. Conventional sputum smear microscopy (CM) method (Figure 5.1) is the most widely used test for TB screening especially in lower and middle income countries due to its low cost and minimal bio-safety standards [27]. However, manual identification and counting of bacilli using CM is very time consuming, labor intensive and tedious work. According to the WHO guidelines, examination of 300 view fields should be performed within 24 hours of collection of specimen for accurate diagnosis [141]. It takes 40 minutes to 3 hours to analyze 40-100 view-field images from a single slide [116]. As a result, the sensitivity of TB detection varies and relies on experience of microbiologists [97]. It has been reported that the manual screening may misdiagnose 33–50% of active cases [97]. All these issues can be addressed using automated methods which increase the sensitivity and specificity of TB screening [29].

Several methods have previously been proposed for bacilli detection in fluorescence [89, 177-179] and conventional [136, 180, 181] microscopic images. Detection of bacilli from CM is more challenging than fluorescence microscopy due to artifacts, over-staining and lack of clear separation of bacilli from background. CostaFilho *et al.*, have developed a neural network based approach [180] which initially determine the density of background using the Hue component in image. Set of color features were used for bacilli segmentation. Color ratio was used as an additional parameter to overcome the misclassification due to high density background. Zhai *et al.* [181] converted RGB images into HSV and Lab color space to perform coarse and fine segmentation of bacilli the CM images. In 2011, Osman *et al.* [136] used a single-layer feed-forward neural network technique for tuberculosis bacilli detection. Most of the reported methods have not segmented overlapped bacilli and ignored them during performance evaluation.

In this Chapter, watershed segmentation, a gray level segmentation method, along with several preprocessing techniques was used to segment the bacilli from ZN-staining images. This segmentation method is a simple, fast and accurate technique which can also segment the overlapping bacilli. These images were grouped into different categories to check the robustness of this segmentation method on different infection level, image contents and microscope configurations.
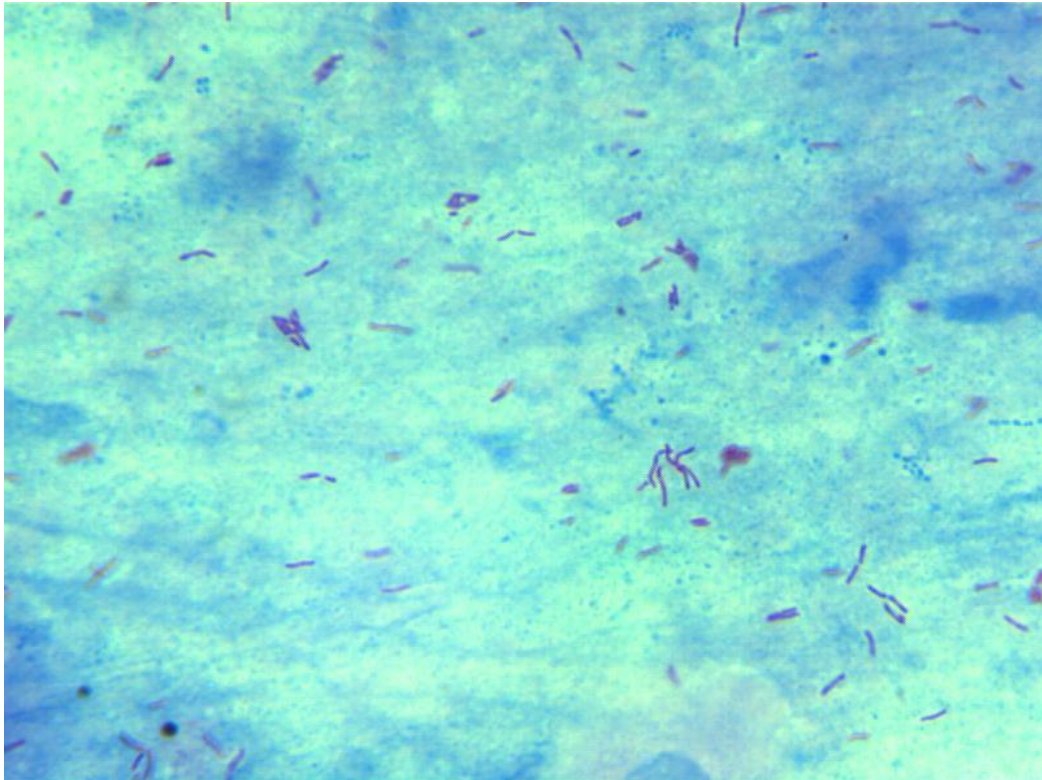
Figure 5.1 A sample ZN stained sputum smear microscopy image. The rod-shaped object is the *M. tuberculosis* bacilli.

5.2 Material and Methods

5.2.1 Datasets

Performance of watershed segmentation was evaluated on following datasets:

i.   In total, 40 images were randomly extracted from Ziehl-Neelsen Sputum smear Microscopy image Database (ZNSM-iDB) [175]. These images were acquired using three different conventional microscopes (CM) including Smartphone enabled microscope. These images were grouped into medium and higher density background images.

ii. In total, 30 images were randomly extracted from Smartphone enabled microscope (Microscope -3 (MS-3)) of ZNSM-iDB. These images were acquired using Smartphone enabled conventional microscope. In (i) & (ii) datasets, sensitivity and specificity of the watershed algorithm were calculated.

iii. Images were extracted from ZNSM-iDB and grouped into four categories based on the infection level (Table 5.1) [148]. Sensitivity and specificity of watershed segmentation method for classifying an image as TB positive or negative were determined for each category. Sensitivity and precision rate of this segmentation method for identifying true bacilli were also determined for each category. Furthermore, discordance rate was calculated for watershed segmentation method to evaluate the percent of pairs where the

observation with TB-positive has a lower predicted probability than TB-negative [149, 150]. Predicted probability was calculated in binary logistic regression model [150].

Table 5.1 View-field Images' grading on the basis of infection level

# of Bacilli	# of View-Fields to be Examined	Grading
1-9 in 100 view-fields	100	Scanty[a]
10-99 in 100 view-fields	100	1+
1-10 in each view-field	50	2+
>10 in each view-field	20	3+

[a]Report exact number of bacilli present in the view-fields. Based on "National Tuberculosis Control Programme, India [148]"

5.2.2 Watershed Transform

The watershed transform is a popular segmentation method of mathematical morphology field. Beucher and Lantue ´joul had introduced it first time in image analysis [182]. The basic concept of watershed is based on visualizing a gray level image into its topographic representation (Figure 5.2), where the height of every pixel is directly related to its gray level, and considers rain gradually falling on the terrain or land relief (the vertical and horizontal dimension of land surface). Then the watersheds lines separate the catchment basins (area of land where all surface water from rain converges to a single point at a lower elevation). In order to locate catchment basin boundaries at high gradient points, the gradient of image is generally used to compute the watershed transform [183].
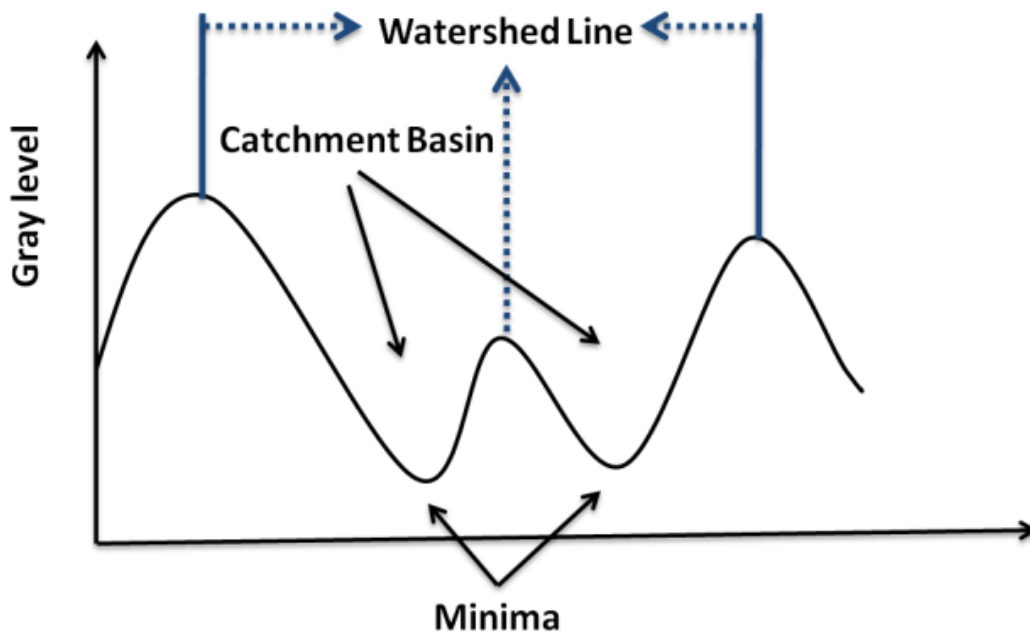
Figure 5.2 Topographical representation of a gray level image using Watershed method.

5.2.3 Methods

Bacilli detection and classification were performed in six different steps which are presented as flowchart in Figure 5.3. In the first step, the collected images were converted to grayscale for further processing and implementation of watershed segmentation. Grayscale conversion was performed by eliminating the Hue and saturation information while retaining the luminance in original image. Second step is used to enhance the contrast of grayscale image for better and clear visibility of bacilli. Contrast was enhanced by saturating 1% of data at low and high intensities of grayscale image. Binary conversion of image through thresholding was performed in third step to separate bacilli from the background. The thresholding was unable to produce better results thus image contains artifacts other than true bacilli. To overcome this problem, Step four was opted where foreground objects were labeled using connected component. After labelling of objects, only bacilli were filtered out by removing objects which were smaller or larger than bacilli and not in rod shaped objects. Pixels of connected components (objects) were used for calculating the size of object while the perimeter of objects was used in Eq. 5.1 for calculating the circularity of objects. In final step, the watershed algorithm was implemented for segmentation and separation of overlapping (touching) bacilli.
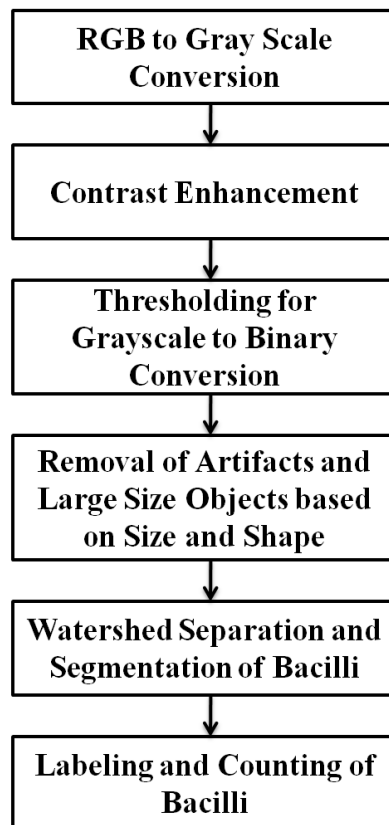
Figure 5.3 Flowchart of proposed method

$$\text{Circularity} = \frac{4*\pi*\text{area}}{\text{Perimeter}^2} \qquad (5.2)$$

5.3 Results and Discussion

Presented method has been evaluated on three different categories of data mentioned in "Material and Method" section.

In the first category, 40 images were used in which 15 and 25 images were TB positive and TB negative, respectively. Figure 5.4 (a-f) shows that the proposed segmentation technique is able to extract most of the bacilli and eliminate unwanted objects from ZN stained images. In most of the negative images, all objects were eliminated which showed the better specificity of proposed technique. The accuracy of method is presented in the form of sensitivity and specificity. The former is the probability to detect image as TB positive (when it belongs to TB positive category) while the specificity is complement of sensitivity that is the probability to detect image as TB negative when the image did not contain any bacilli. Achieved sensitivity and specificity of watershed segmentation were 100% and 93% respectively (Table 5.2). When density of image background is very high, the specificity was reduced to 72% due to presence of excessive artifacts and staining (Table 5.2). Apart from sensitivity and specificity for the classification of image as TB positive or negative, sensitivity and precision rate for bacilli detection for all TB positive images were also calculated. In this case, sensitivity is a true positive rate of detecting bacillus when in fact it is a bacillus while precision or positive predictive value (PPV) is defined as the ratio of correctly classified bacilli and number of objects classified as bacilli. These values were calculated to check the efficacy of our approach in classifying/detecting the bacilli over artifacts. Achieved average sensitivity and average precision for bacilli detection are 90.3% and 77% respectively (Table 5.3).

In the second category, 30 set of camera-enabled Smartphone microscopic images were used in which 15 images were TB positive while other 15 were TB negative. The proposed segmentation technique is able to extract most of the bacilli and eliminate unwanted objects from ZN stained images. Watershed segmentation has achieved the overall sensitivity and specificity of 93.3% and 87%, respectively for classifying the images as TB positive or negative.

(a)

(b)

(c)

(d)

(e)
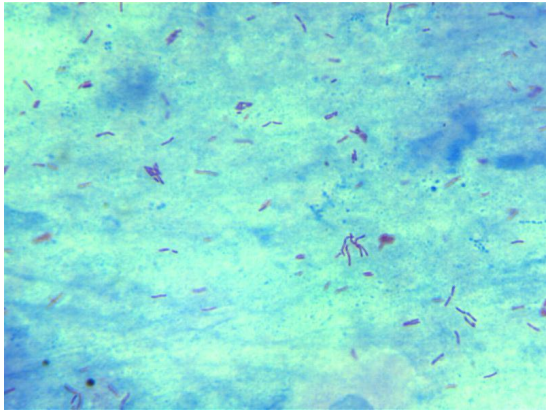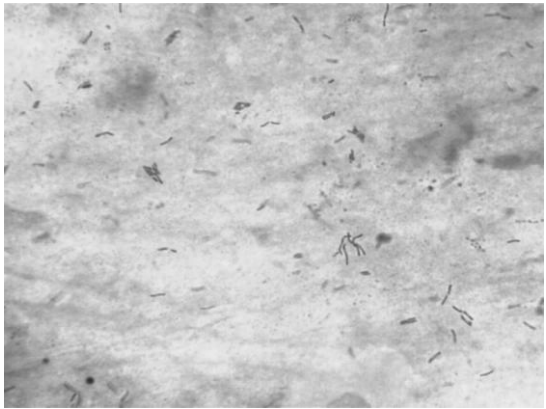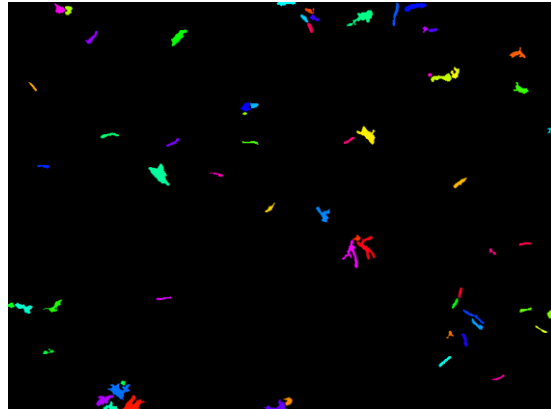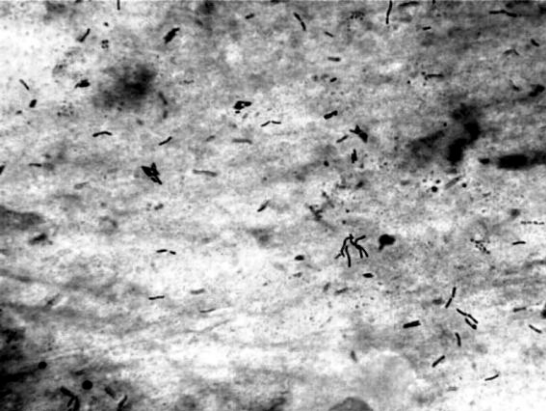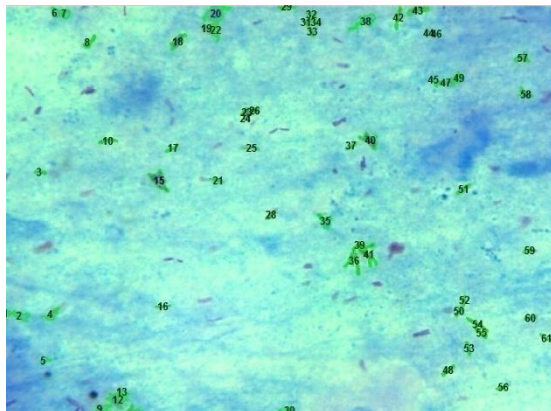
(f)

Figure 5.4 Stepwise presentation of Watershed segmentation method for detection and classification of bacilli in ZN stained sputum smear image. (a) Original image, (b) RGB to grayscale conversion, (c) contrast enhancement, (d) binarized image, (e) artefacts removal and Watershed segmentation, and (f) Labelled Image

Table 5.2 Performance of the watershed method in image classification as TB positive or negative.

Image content	Sensitivity (%)	Specificity (%)
Low density	100	93
High density	100	72

Table 5.3 Performance of the watershed method in true bacilli detection.

Sensitivity (%)	Precision (%)
90.3	77

Camera-enabled Smartphone microscopes can significantly contribute to the healthcare technology, especially in the remote areas of TB-endemic developing countries where skilled medical staff and better clinical laboratory are not available. It can also enable the accessibility of these tests to the high-quality healthcare as an EHR for better microscopic evaluation of sputum smear and other samples. Camera-enabled Smartphone microscopy used in this Chapter for bacilli detection can be used to monitor the TB patients. This system would support the WHO's DOTS program, which was established to abolition of TB worldwide [177].

In third category, images were grouped on the basis of different infection level (Scanty, 1+, 2+ and 3+, Table 5.1). Sensitivity, specificity and Precision rate of watershed segmentation method on different infection level are depicted in Table 5.3. The performance of this segmentation method is related to the level of infection. Performance is better when infection level is higher. Furthermore, this segmentation provided a discordant rate of 3.73% with respect to tuberculosis positive and negative cases.

Table 5.3 Performance of watershed segmentation method on different infection level

Grade	TB Positive or Negative (%)		True Bacilli (%)	
	Sensitivity[a]	Specificity[a]	Sensitivity[b]	Precision[b]
Scanty	42.86	74.73	55.56	26.19
1+	81.25	75.29	55.56	52.4
2+	92.86	NA[*]	61.73	72
3+	100	NA[*]	90.23	79.09

[b]Sensitivity and precision rate of watershed segmentation method for identifying true bacilli in the view-field images.

[*]Datasets does not contain tuberculosis negative view-field images.

5.4 Conclusion

A method is presented to detect and classify the bacilli from ZN stained sputum smear microscopy images. Image pre-processing techniques were implemented for contrast enhancement and removal of unwanted regions from the images. Circularity and size of objects were used to extract the bacilli. For final segmentation and separation, watershed segmentation was used which provided better results for all four types of images. Performance of the current method was evaluated on different infection level to evaluate the robustness w.r.t infection levels. This method has shown better performance on higher infection level images. This method is very significant in detecting bacilli even for challenging images with high density and overlapped bacilli.

CHAPTER 6

CONCLUSION AND FUTURE WORK

6.1 Conclusion

In the proposed thesis, work in support of automated microscopy development using image analysis techniques has been performed. Current work advances the knowledge of automated microscopy development. In this thesis, a web resource of ZN stained sputum smear images (ZNSM-iDB), identification of robust autofocusing method, establishment of robust hybrid focus measure functions, and implementation of bacilli segmentation methods have been performed to support the automated microscopy development.

In Chapter 2, a newly developed web resource called "ZNSM-iDB" is presented. The ZNSM-iDB is a unified and well versed database in terms of imaging contents and acquisition technology. This resource may serve as the standard platform to validate existing methods as well as to develop new ones for automated microscopy (*i.e.* autofocusing, autostitching and automated grading). Smartphone-based inexpensive automated disease diagnosis system may be developed and validated using MS-3 datasets of ZNSM-iDB. This system can be used in the remote areas of TB-endemic countries where laboratory resources are limited but Smartphones are widely used. Furthermore, Smartphone camera is also a portable computer which can be used simultaneously for automatic bacilli segmentation and grading using image processing techniques and maintaining electronic health record. The ZNSM-iDB is expected to serve as a referral resource for the research groups working in the domains of automated microscopy algorithms development.

In Chapter 3, robust autofocusing functions were identified using comprehensive analysis. Autofocusing using focus measure functions (FMFs) assists segmentation methods in segmenting bacilli more effectively. Therefore, the identification of robust and accurate FMFs for a particular imaging system assumes lots of significance for the development of auto-focusing instrument. A comprehensive analyses of 24 FMFs on diverse bright-field CM images provided GDR, TGR, SFB and HSM as the most robust and accurate FMFs. These FMFs can be used for the development of new automated conventional microscopy system which can capture an image directly from ZN stained sputum smear slide.

In Chapter 4, a robust hybrid focus measure function was identified. A comprehensive analysis of twenty-eight hybrid FMFs on diverse datasets, spanning almost all image categories, provided nineteen hybrid methods with accuracy >90%. VGRnSFB is found to be the most robust and accurate HFMF as it showed the best overall accuracy and robustness in different image conditions. This HFMF may be implemented in any imaging system which can capture the best focused image automatically.

In Chapter 5, a bacilli segmented method was presented. Performance of the watershed segmentation method was evaluated on different infection level to evaluate the robustness w.r.t infection levels. This method has shown better performance on higher infection level images. This method is very significant in detecting bacilli even for challenging images with high density and overlapped bacilli.

Automated microscope developed through these methods may provide the mass screening of cases in TB-endemic countries. Automation will deliver faster results to assist early diagnosis of tuberculosis. It will also increase the sensitivity and specificity of tuberculosis diagnosis using ZN sputum smear test.

6.2 Future Prospect

In the future, sensitivity and specificity of watershed segmentation method may be optimized for better disease diagnosis. Following improvements can be incorporated in existing approach:

- Use of color feature in bacilli segmentation to remove overstrained blue artifacts and retain bacilli with reddish color.
- Incorporation of machine learning for supervised classification of TB positive and negative images.
- Comparative analysis of watershed algorithm with previously reported techniques.

[1]. Shortliffe EH, Cimino JJ. *Biomedical informatics: computer applications in health care and biomedicine*: Springer Science & Business Media. 2013

[2]. THE IMPORTANCE OF MEDICAL RECORDS: A CRITICAL PROFESSIONAL RESPONSIBILITY. [cited 2017 15 September]; Available from: https://www.gapmedics.com/blog/2014/03/25/the-importance-of-medical-records-a-critical-professional-responsibility/.

[3]. Type of Medical Data. MIT computer science and artificial intelligence laboratory [cited 2017 10 September]; Available from: https://groups.csail.mit.edu/medg/courses/6872/96/notes/Tsien/sld016.htm.

[4]. Medical Record and its Importance. 2017; Available from: http://www.healthnet.org.np/reports/bpklcos/mrecord.html.

[5]. The Importance of Data in Health Care. [cited 2017 15 September]; Available from: http://www.lumedx.com/the-importance-of-data-in-health-care-.aspx.

[6]. What are the benefits of personal health records? [cited 2017 15 September]; Available from: https://www.healthit.gov/providers-professionals/faqs/what-are-benefits-personal-health-records.

[7]. History Taking. [cited 2017 15 September]; Available from: https://patient.info/in/doctor/history-taking.

[8]. Sharing medical data: From the perspective of a doctor. [cited 2017 15 September]; Available from: https://www.futurehealthindex.com/2017/01/31/sharing-medical-data-perspective-doctor/.

[9]. Dresselhaus TR, Peabody JW, Lee M, Wang MM, Luck J. *Measuring compliance with preventive care guidelines*. Journal of General Internal Medicine. 15(11):782-8. 2000

[10]. Dexheimer JW, Talbot TR, Sanders DL, Rosenbloom ST, Aronsky D. *Prompting clinicians about preventive care measures: a systematic review of randomized controlled trials*. Journal of the American Medical Informatics Association. 15(3):311-20. 2008

[11]. Zhou L, Hripcsak G. *Temporal reasoning with medical data—a review with emphasis on medical natural language processing*. Journal of biomedical informatics. 40(2):183-202. 2007

[12]. D'Souza J, Ng V. *Classifying temporal relations in clinical data: a hybrid, knowledge-rich approach*. Journal of biomedical informatics. 46:S29-S39. 2013

[13]. Collett D. *Modelling survival data in medical research*: CRC press. 2015

[14]. Pakhomov S, Weston SA, Jacobsen SJ, Chute CG, Meverden R, Roger VL. *Electronic medical records for clinical research: application to the identification of heart failure*. Am J Manag Care. 13(6 Part 1):281-8. 2007

[15]. Weaknesses of the Traditional Medical-Record System. [cited 2017 17 September]; Available from: https://groups.csail.mit.edu/medg/courses/6872/96/notes/Tsien/tsld019.htm.

[16]. 5 Top Disadvantages of Manual Medical Records. [cited 2017 17 September]; Available from: http://www.medleague.com/5-top-disadvantages-of-manual-medical-records-emr-expert/.

[17]. Wrenn JO, Stein DM, Bakken S, Stetson PD. *Quantifying clinical narrative redundancy in an electronic health record*. Journal of the American Medical Informatics Association. 17(1):49-53. 2010

[18]. Langer SG. *Challenges for data storage in medical imaging research*. Journal of digital imaging. 24(2):203-7. 2011

[19]. Ilie V, Courtney JF, Van Slyke C, editors. *Paper versus electronic: Challenges associated with physicians' usage of electronic medical records*.

[20]. Okumura A, Suzuki J, Furukawa I, Ono S, Ashihara T. *Signal analysis and compression performance evaluation of pathological microscopic images*. IEEE transactions on medical imaging. 16(6):701-10. 1997

[21]. Hoerbst A, Ammenwerth E. *Electronic health records*. Methods of Information in Medicine. 49(4):320-36. 2010

[22]. Cooke RE, Gaeta MG, Kaufman DM, Henrici JG. Picture archiving and communication system. Google Patents. 2003

[23]. McNerney R. *Diagnostics for developing countries*. Diagnostics. 5(2):200-9. 2015

[24]. Petti CA, Polage CR, Quinn TC, Ronald AR, Sande MA. *Laboratory medicine in Africa: a barrier to effective health care*. Clinical Infectious Diseases. 42(3):377-82. 2006

[25]. McNerney R, Sollis K, Peeling RW. *Improving access to new diagnostics through harmonised regulation: priorities for action: opinion paper*. African Journal of Laboratory Medicine. 3(1):1-7. 2014

[26]. Dowdy DW, Steingart KR, Pai M. *Serological testing versus other strategies for diagnosis of active tuberculosis in India: a cost-effectiveness analysis*. PLoS medicine. 8(8):e1001074. 2011

[27]. *WHO TB Global Report*. 2015

[28]. Osibote OA, Dendere R, Krishnan S, Douglas TS, J. *Automated focusing in bright-field microscopy for tuberculosis detection*. 240(2):155-63. 2010

[29]. Panicker RO, Soman B, Saini G, Rajan J. *A review of automatic methods based on image processing techniques for tuberculosis detection from microscopic sputum smear images*. Journal of medical systems. 40(1):17. 2016

[30]. Peeling RW, McNerney R. *Emerging technologies in point-of-care molecular diagnostics for resource-limited settings*. Expert review of molecular diagnostics. 14(5):525-34. 2014

[31]. Prince JL, Links JM. *Medical imaging signals and systems*: Pearson Prentice Hall Upper Saddle River, New Jersey. 2006

[32]. Sun and Other Types of Radiation. American cancer society; 2017; Available from: https://www.cancer.org/cancer/cancer-causes/radiation-exposure.html.

[33]. Byrns G, Palatianos KC, Shands L, Fennelley K, McCammon C, Boudreau A, et al. *Chemical hazards in radiology*. Applied occupational and environmental hygiene. 15(2):203-8. 2000

[34]. Shakhatreh FM. *Reproductive health of male radiographers*. Saudi medical journal. 22(2):150-2. 2001

[35]. Ultrasound - Breast. RadiologyInfo.org; [cited 2017 12 Sept]; Available from: https://www.radiologyinfo.org/en/info.cfm?PG=breastus.

[36]. Ultrasound. Breastcancer.org; [cited 2017 9 Sept]; Available from: http://www.breastcancer.org/testing_ultrasound.html.

[37]. Ultrasound Imaging. [cited 2017 15 September]; Available from: https://www.cancerquest.org/patients/detection-and-diagnosis/ultrasound#footnote8_xppkmw1.

[38]. How do the imaging choices compare? [cited 2017 15 September]; Available from: https://www.nps.org.au/medical-info/consumer-info/imaging-explained?c=how-do-the-imaging-choices-compare-291782b0.

[39]. Gurcan MN, Boucheron LE, Can A, Madabhushi A, Rajpoot NM, Yener B. *Histopathological image analysis: A review*. IEEE reviews in biomedical engineering. 2:147-71. 2009

[40]. Fox H. *Is H&E morphology coming to an end?* Journal of clinical pathology. 53(1):38-40. 2000

[41]. Janowczyk A, Madabhushi A. *Deep learning for digital pathology image analysis: A comprehensive tutorial with selected use cases*. Journal of pathology informatics. 7. 2016

[42]. Bhargava R, Madabhushi A. *Emerging themes in image informatics and molecular analysis for digital pathology*. Annual review of biomedical engineering. 18:387-412. 2016

[43]. Rubin GD. *Data explosion: the challenge of multidetector-row CT*. European journal of radiology. 36(2):74-80. 2000

[44]. van Ginneken B, Schaefer-Prokop CM, Prokop M. *Computer-aided diagnosis: how to move from the laboratory to the clinic*. Radiology. 261(3):719-32. 2011

[45]. Cheng J-Z, Ni D, Chou Y-H, Qin J, Tiu C-M, Chang Y-C, et al. *Computer-aided diagnosis with deep learning architecture: applications to breast lesions in US images and pulmonary nodules in CT scans*. Scientific reports. 6:24454. 2016

[46]. Doi K. *Computer-aided diagnosis in medical imaging: historical review, current status and future potential*. Computerized medical imaging and graphics. 31(4):198-211. 2007

[47]. Giger ML, Chan HP, Boone J. *Anniversary paper: History and status of CAD and quantitative image analysis: the role of Medical Physics and AAPM*. Medical physics. 35(12):5799-820. 2008

[48]. Cheng J-Z, Chou Y-H, Huang C-S, Chang Y-C, Tiu C-M, Chen K-W, et al. *Computer-aided US diagnosis of breast lesions by using cell-based contour grouping*. Radiology. 255(3):746-54. 2010

[49]. Giger ML, Karssemeijer N, Schnabel JA. *Breast image analysis for risk assessment, detection, diagnosis, and treatment of cancer*. Annual review of biomedical engineering. 15:327-57. 2013

[50]. Joo S, Yang YS, Moon WK, Kim HC. *Computer-aided diagnosis of solid breast nodules: use of an artificial neural network based on multiple sonographic features*. IEEE transactions on medical imaging. 23(10):1292-300. 2004

[51]. Chen C-M, Chou Y-H, Han K-C, Hung G-S, Tiu C-M, Chiou H-J, et al. *Breast lesions on sonograms: computer-aided diagnosis with nearly setting-independent features and artificial neural networks*. Radiology. 226(2):504-14. 2003

[52]. Drukker K, Sennett CA, Giger ML. *Automated method for improving system performance of computer-aided diagnosis in breast ultrasound*. IEEE transactions on medical imaging. 28(1):122-8. 2009

[53]. Awai K, Murao K, Ozawa A, Nakayama Y, Nakaura T, Liu D, et al. *Pulmonary nodules: estimation of malignancy at thin-section helical CT—effect of computer-aided diagnosis on performance of radiologists*. Radiology. 239(1):276-84. 2006

[54]. McCarville MB, Lederman HM, Santana VM, Daw NC, Shochat SJ, Li C-S, et al. *Distinguishing benign from malignant pulmonary nodules with helical chest CT in children with malignant solid tumors*. Radiology. 239(2):514-20. 2006

[55]. Singh S, Maxwell J, Baker JA, Nicholas JL, Lo JY. *Computer-aided classification of breast masses: performance and interobserver variability of expert radiologists versus residents*. Radiology. 258(1):73-80. 2011

[56]. Sahiner B, Petrick N, Chan H-P, Hadjiiski LM, Paramagul C, Helvie MA, et al. *Computer-aided characterization of mammographic masses: accuracy of mass segmentation and its effects on characterization*. IEEE transactions on medical imaging. 20(12):1275-84. 2001

[57]. Sun T, Zhang R, Wang J, Li X, Guo X. *Computer-aided diagnosis for early-stage lung cancer based on longitudinal and balanced data*. PloS one. 8(5):e63559. 2013

[58]. Armato SG, Sensakovic WF. *Automated lung segmentation for thoracic CT: Impact on computer-aided diagnosis1*. Academic Radiology. 11(9):1011-21. 2004

[59]. Armato SG, 3rd, McLennan G, Bidaut L, McNitt-Gray MF, Meyer CR, Reeves AP, et al. *The Lung Image Database Consortium (LIDC) and Image Database Resource Initiative (IDRI): a completed reference database of lung nodules on CT scans*. Med Phys. 38(2):915-31. Epub 2011/04/02. 2011

[60]. Way T, Chan H-P, Hadjiiski L, Sahiner B, Chughtai A, Song TK, et al. *Computer-Aided Diagnosis of Lung Nodules on CT Scans:: ROC Study of Its Effect on Radiologists' Performance*. Academic Radiology. 17(3):323-32. 2010

[61]. Way TW, Sahiner B, Chan HP, Hadjiiski L, Cascade PN, Chughtai A, et al. *Computer‐aided diagnosis of pulmonary nodules on CT scans: Improvement of classification performance with nodule surface features*. Medical physics. 36(7):3086-98. 2009

[62]. Newell D, Nie K, Chen J-H, Hsu C-C, Hon JY, Nalcioglu O, et al. *Selection of diagnostic features on breast MRI to differentiate between malignant and benign lesions using computer-aided diagnosis: differences in lesions presenting as mass and non-mass-like enhancement*. European radiology. 20(4):771-81. 2010

[63]. Yang M-C, Moon WK, Wang Y-CF, Bae MS, Huang C-S, Chen J-H, et al. *Robust texture analysis using multi-resolution gray-scale invariant features for breast sonographic tumor diagnosis*. IEEE transactions on medical imaging. 32(12):2262-73. 2013

[64]. Gómez W, Pereira W, Infantosi AFC. *Analysis of co-occurrence texture statistics as a function of gray-level quantization for classifying breast ultrasound*. IEEE transactions on medical imaging. 31(10):1889-99. 2012

[65]. Tourassi GD, Frederick ED, Markey MK, Floyd CE. *Application of the mutual information criterion for feature selection in computer-aided diagnosis*. Medical physics. 28(12):2394-402. 2001

[66]. Jaeger S, Karargyris A, Candemir S, Siegelman J, Folio L, Antani S, et al. *Automatic screening for tuberculosis in chest radiographs: a survey*. Quantitative imaging in medicine and surgery. 3(2):89. 2013

[67]. Nakamura K, Ohmi A, Kurihara T, Suzuki S, Tadera M. *Studies on the diagnostic value of 70 mm radiophotograms by mirror camera and the reading ability of physicians*. Kekkaku (Tuberculosis). 45(4):121-8. 1970

[68]. Noor NM, Rijal OM, Yunus A, Mahayiddin AA, Peng GC, Abu-Bakar S, editors. *A statistical interpretation of the chest radiograph for the detection of pulmonary tuberculosis*. Biomedical Engineering and Sciences (IECBES), 2010 IEEE EMBS Conference on; 2010

[69]. Schilham AM, Van Ginneken B, Loog M. *A computer-aided diagnosis system for detection of lung nodules in chest radiographs with an evaluation on a public database*. Medical image analysis. 10(2):247-58. 2006

[70]. Toman K. *Toman's Tuberculosis: case detection, treatment, and monitoring: questions and answers*: World Health Organization. 2004

[71]. Shen R, Cheng I, Basu A. *A hybrid knowledge-guided detection technique for screening of infectious pulmonary tuberculosis from chest radiographs*. IEEE transactions on biomedical engineering. 57(11):2646-56. 2010

[72]. Maduskar P, Hogeweg L, Philipsen R, Schalekamp S, van Ginneken B, editors. *Improved texture analysis for automatic detection of tuberculosis (TB) on chest radiographs with bone suppression images*. SPIE Medical Imaging; 2013: International Society for Optics and Photonics.

[73]. Jaeger S, Karargyris A, Antani S, Thoma G, editors. *Detecting tuberculosis in radiographs using combined lung masks*. Engineering in Medicine and Biology Society (EMBC), 2012 Annual International Conference of the IEEE; 2012

[74]. Noor NM, Rijal O, Fah CY, editors. *Wavelet as features for Tuberculosis (MTB) using standard x-ray film images*. Signal Processing, 2002 6th International Conference on; 2002

[75]. Xu T, Cheng I, Long R, Mandal M. *Novel coarse-to-fine dual scale technique for tuberculosis cavity detection in chest radiographs*. EURASIP Journal on Image and Video Processing. 2013(1):3. 2013

[76]. Song Y-L, Yang Y, editors. *Localization algorithm and implementation for focal of pulmonary tuberculosis chest image*. Machine Vision and Human-Machine Interface (MVHI), 2010 International Conference on; 2010

[77]. Rijal OM, Ebrahimian H, Noor NM, editors. *Determining features for discriminating PTB and normal lungs using phase congruency model*. Biomedical and Health Informatics (BHI), 2012 IEEE-EMBS International Conference on; 2012

[78]. Leibstein JM, Nel AL. *Detecting tuberculosis in chest radiographs using image processing techniques*. University of Johannesburg. 2006

[79]. Koeslag A, de Jager G. *Computer aided diagnosis of miliary tuberculosis*. Proceedings of the Pattern Recognition Association of South Africa. 2001

[80]. Sarkar S, Chaudhuri S, editors. *Automated detection of infiltration and cavitation in digital chest radiographs of chronic pulmonary tuberculosis*. Engineering in Medicine and Biology Society, 1996 Bridging Disciplines for Biomedicine Proceedings of the 18th Annual International Conference of the IEEE; 1997

[81]. Le K, editor. *Automated detection of early lung cancer and tuberculosis based on X-ray image analysis*. Proc WSEAS International Conference on Signal, Speech and Image Processing; 2006

[82]. Hariharan S, Ray A, Ghosh M, editors. *An algorithm for the enhancement of chest X-ray images of tuberculosis patients*. Industrial Technology 2000 Proceedings of IEEE International Conference on. 2000

[83]. Tan JH, Acharya UR, Tan C, Abraham KT, Lim CM. *Computer-assisted diagnosis of tuberculosis: a first order statistical approach to chest radiograph*. Journal of medical systems. 36(5):2751-9. 2012

[84]. Arzhaeva Y, Hogeweg L, de Jong PA, Viergever MA, van Ginneken B, editors. *Global and local multi-valued dissimilarity-based classification: Application to computer-aided detection of tuberculosis*. International Conference on Medical Image Computing and Computer-Assisted Intervention; 2009

[85]. Lieberman R, Kwong H, Liu B, Huang H, editors. *Computer-assisted detection (CAD) methodology for early detection of response to pharmaceutical therapy in tuberculosis patients*. Proceedings of SPIE--the International Society for Optical Engineering; 2009: NIH Public Access.

[86]. Chauhan A, Chauhan D, Rout C. *Role of gist and phog features in computer-aided diagnosis of tuberculosis without segmentation*. PloS one. 9(11):e112980. 2014

[87]. Greenberg SD, Frager D, Suster B, Walker S, Stavropoulos C, Rothpearl A. *Active pulmonary tuberculosis in patients with AIDS: spectrum of radiographic findings (including a normal appearance)*. Radiology. 193(1):115-9. 1994

[88]. Breslauer DN, Maamari RN, Switz NA, Lam WA, Fletcher DA, S. *Mobile phone based clinical microscopy for global health applications*. Plo e6320. 4(7). 2009

[89]. Tapley A, Switz N, Reber C, Davis JL, Miller C, Matovu JB, et al. *Mobile digital fluorescence microscopy for diagnosis of tuberculosis*. Journal of clinical microbiology. 51(6):1774-8. 2013

[90]. Firestone L, Cook K, Culp K, Talsania N, Preston K. *Comparison of autofocus methods for automated microscopy*. Cytometry. 12(3):195-206. 1991

[91]. Geusebroek JM, Cornelissen F, Smeulders AW, Geerts H. *Robust autofocusing in microscopy*. Cytometry Part A. 39(1):1-9. 2000

[92]. Groen FC, Young IT, Ligthart G. *A comparison of different focus functions for use in autofocus algorithms*. Cytometry. 6(2):81-91. 1985

[93]. Gu CC, Wu KJ, Hu J, Hao C, Guan XP. *Region sampling for robust and rapid autofocus in microscope*. Microsc Res Tech. 78(5):382-90. 2015

[94]. Costa Filho CF, Costa MF, Júnior A. *Autofocus functions for tuberculosis diagnosis with conventional sputum smear microscopy*. Proc of Current Microscopy Contributions to Advances in Science and Technology Formatex Research Center.13-20. 2012

[95]. Fan Z, Chen S, Hu H, Chang H, Fu Q, editors. *Autofocus algorithm based on wavelet packet transform for infrared microscopy*. Image and Signal Processing (CISP), 2010 3rd International Congress on; 2010

[96]. Huang W, Jing Z. *Evaluation of focus measures in multi-focus image fusion*. Pattern recognition letters. 28(4):493-500. 2007

[97]. Kimura A, Costa MG, Filho FF, Fujimoto L, Salem J. *Evaluation of autofocus functions of conventional sputum smear microscopy for tuberculosis*. In Engineering in Medicine and Biology Society EMBC Annual International Conference of the IEEE pp.3041-4 SRC - GoogleScholar. 2010

[98]. MateosPerez JM, Cristóbal G, Escalante-Ramírez B, Redondo R, Nava R, Valdiviezo JC, et al. *Comparative evaluation of autofocus algorithms for a real-time system for automatic detection of Mycobacterium tuberculosis*. doi 101002cytoa2. 2012

[99]. Pech-Pacheco JL, Cristóbal G, Chamorro-Martinez J, Fernández-Valdivia J, editors. *Diatom autofocusing in brightfield microscopy: a comparative study*. Pattern Recognition, 2000 Proceedings 15th International Conference on; 2000

[100]. Pertuz S, Puig D, A. M. *Garcia of focus measure operators for shape-from-focus*. Pattern Recognition doi101016jpatcog11011. 46(5):1415-32. 2012

[101]. Redondo R, Bueno G, Valdiviezo JC, Nava R, Cristóbal G, Déniz O, et al. *Autofocus evaluation for brightfield microscopy pathology*. Journal of biomedical optics. 17(3):0360081-8. 2012

[102]. Russell MJ, Douglas TS, editors. *Evaluation of autofocus algorithms for tuberculosis microscopy*. Engineering in Medicine and Biology Society, 2007 EMBS 2007 29th Annual International Conference of the IEEE; 2007

[103]. Santos A, Ortiz de Solórzano C, Vaquero JJ, Pena J, Malpica N, Del Pozo F. *Evaluation of autofocus functions in molecular cytogenetic analysis*. Journal of Microscopy. 188(3):264-72. 1997

[104]. Sun Y, Duthaler S, Nelson BJ. *Autofocusing in computer microscopy: selecting the optimal focus algorithm*. Microscopy research and technique. 65(3):139-49. 2004

[105]. Sun Y, Duthaler S, Nelson BJ, editors. *Autofocusing algorithm selection in computer microscopy*. Intelligent Robots and Systems, 2005(IROS 2005) 2005 IEEE/RSJ International Conference on; 2005

[106]. Brown M, Lowe DG. *Automatic panoramic image stitching using invariant features*. International journal of computer vision. 74(1):59-73. 2007

[107]. Yang F, Deng ZS, Fan QH. *A method for fast automated microscope image stitching*. Micron. 48:17-25. 2013

[108]. Piccinini F, Bevilacqua A, Lucarelli E. *Automated image mosaics by non‐automated light microscopes: the MicroMos software tool*. Journal of Microscopy. 252(3):226-50. 2013

[109]. Subramanyam M, editor. *Automatic image mosaic system using steerable Harris corner detector*. Machine Vision and Image Processing (MVIP), 2012 International Conference on; 2012

[110]. Ali S, Hussain M. *Panoramic image construction using feature based registration methods*. In 15th International Multitopic Conference INMIC.209-14. 2012

[111]. Bai X, Ning X, Wang L, Ieee. *Analysis and comparison of feature detection and matching algorithms for rovers vision navigation*. In 8th Symposium on Instrumentation and Control Technology ISICT pp.66-71. 2012

[112]. Makkapati V, Agrawal R, Acharya R, editors. *Segmentation and classification of tuberculosis bacilli from ZN-stained sputum smear images*. Automation Science and Engineering, 2009 CASE 2009 IEEE International Conference on; 2009

[113]. Forero MG, Cristóbal G, Desco M. *Automatic identification of Mycobacterium tuberculosis by Gaussian mixture models*. 223(2):120-32. 2006

[114]. Forero-Vargas M, Sroubek F, Alvarez-Borrego J, Malpica N, Cristóbal G, Santos A, et al. *Segmentation, autofocusing and signature extraction of tuberculosis sputum images*. Photonic Devices and Algorithms for Computing IV Proceedings.341-52. 2002

[115]. Desikan P. *Sputum smear microscopy in tuberculosis: Is it still relevant?* Indian J Med Res. 137(3):442. 2013

[116]. Sotaquira M, Rueda L, Narvaez R, International P. *Detection and quantification of bacilli and clusters present in sputum smear samples: a novel algorithm for pulmonary tuberculosis diagnosis*. In Digital Image pp IEEE March. 2009:117-21.

[117]. Shingadia D, Novelli V. *Diagnosis and treatment of tuberculosis in children*. Lancet Infect Dis. 3(10):624-32. 2003

[118]. Lewis JJ, Chihota VN, van Fourie PB, Fielding KL, Grant AD, der Meulen M, et al. *"Proof-Of-Concept" Evaluation of an Automated Sputum Smear Microscopy System for Tuberculosis Diagnosis*. PLoS ONE. 7(11). 2012

[119]. Yang F, Deng Z-S, Fan Q-H. *A method for fast automated microscope image stitching*. Micron. 48:17-25. 2013

[120]. Khutlang R, Krishnan S, Whitelaw A, Douglas TS, J. *Automated detection of tuberculosis in Ziehl‐Neelsen‐stained sputum smears using two one‐class classifiers*. 237(1):96-102. 2010

[121]. Patel B, Douglas TS, editors. *Creating a virtual slide map of sputum smears by auto-stitching*. Engineering in Medicine and Biology Society, EMBC, 2011 Annual International Conference of the IEEE; 2011

[122]. Lamdan Y, Wolfson HJ. *Geometric hashing: A general and efficient model-based recognition scheme*. 1988

[123]. Lamdan Y, Wolfson HJ, editors. *On the error analysis of'Geometric Hashing'*. Computer Vision and Pattern Recognition, 1991 Proceedings CVPR'91, IEEE Computer Society Conference on; 1991

[124]. Wolfson HJ, Rigoutsos I. *Geometric hashing: An overview*. IEEE computational science and engineering. 4(4):10-21. 1997

[125]. Begelman G, Lifshits M, Rivlin E. *Visual positioning of previously defined ROIs on microscopic slides*. IEEE Transactions on Information Technology in Biomedicine. 10(1):42-50. 2006

[126]. Lifshits M, Goldenberg R, Rivlin E, Rudzsky M, Adel M. *Image-based wafer navigation*. IEEE transactions on semiconductor manufacturing. 17(3):432-43. 2004

[127]. Dogan H, Ekinci M. *Automatic panorama with auto-focusing based on image fusion for microscopic imaging system*. Signal, image and video processing. 8(1):5-20. 2014

[128]. Chauhan A. Development of efficient computer aided diagnosis methods for tuberculosis diagnosis (Unpublished doctoral thesis). Jaypee University of Information Technology, India 2016.

[129]. Costa MG, Filho FF, Sena JF, Salem J, de Lima MO. *Automatic identification of mycobacterium tuberculosis with conventional light microscopy*. In Engineering in Medicine and Biology Society EMBC 30th Annual International Conference of the IEEE.382-5. 2008

[130]. Priya E, Srinivasan S, J. *Automated identification of tuberculosis objects in digital images using neural network and neuro fuzzy inference systems*. Imaging Health Inform. 5(3):506-12. 2015

[131]. Tadrous PJ, J. *Computer-assisted screening of Ziehl-Neelsen–stained tissue for mycobacteria algorithm design and preliminary studies on 2,000 images*. American Pathol. 133(6):849-58. 2010

[132]. Sadaphal P, Rao J, Comstock G, Beg M. *Image processing techniques for identifying Mycobacterium tuberculosis in Ziehl-Neelsen stains*. The International Journal of Tuberculosis and Lung Disease. 12(5):579-82. 2008

[133]. Osman MK, Mashor MY, Jaafar H, editors. *Segmentation of tuberculosis bacilli in Ziehl-Neelsen tissue slide images using Hibrid Multilayered Perceptron network*. Information Sciences Signal Processing and their Applications (ISSPA), 2010 10th International Conference on; 2010

[134]. Osman MK, Ahmad F, Saad Z, Mashor MY, Jaafar H, editors. *A genetic algorithm-neural network approach for Mycobacterium tuberculosis detection in Ziehl-Neelsen stained tissue slide images*. Intelligent Systems Design and Applications (ISDA), 2010 10th International Conference on; 2010

[135]. Osman MK, Noor MHM, Mashor MY, Jaafar H, editors. *Compact single hidden layer feedforward network for mycobacterium tuberculosis detection*. Control System, Computing and Engineering (ICCSCE), 2011 IEEE International Conference on; 2011

[136]. Osman M, Mashor M, Jaafar H, editors. *Tuberculosis bacilli detection in Ziehl-Neelsen-stained tissue using affine moment invariants and Extreme Learning Machine*. Signal Processing and its Applications (CSPA), 2011 IEEE 7th International Colloquium on; 2011

[137]. Khutlang R, Krishnan S, Dendere R, Whitelaw A, Veropoulos K, Learmonth G, et al. *Classification of Mycobacterium tuberculosis in images of ZN-stained sputum smears*. IEEE Transactions on Information Technology in Biomedicine. 14(4):949-57. 2010

[138]. Costa MGF, Filho CFF, Kimura A, Levy PC, Xavier CM, Fujimoto LB. *A sputum smear microscopy image database for automatic bacilli detection in conventional microscopy*. In Engineering in Medicine and Biology Society EMBC 36th Annual International Conference of the IEEE pp August.2841-4. 2014

[139]. Sreeramareddy CT, Panduru KV, Menten J, Ende J, C. BM. *Van den Time delays in diagnosis of pulmonary tuberculosis: a systematic review of literature*. Dis 91 1. 9(1). 2009

[140]. Small PM, Pai M. *Tuberculosis diagnosis—time for a game change*. N Engl J Med. 363(11):1070-1. 2010

[141]. Ba F, Rieder HL. *A comparison of fluorescence microscopy with the Ziehl-Neelsen technique in the examination of sputum for acid-fast bacilli*. The international journal of tuberculosis and lung disease : the official journal of the International Union against Tuberculosis and Lung Disease. 3(12):1101-5. Epub 1999/12/22. 1999

[142]. Mesker WE, Torrenga H, Sloos WCR, Vrolijk H, Tollenaar R, de Bruin PC, et al. *Supervised automated microscopy increases sensitivity and efficiency of detection of sentinel node micrometastases in patients with breast cancer Pathology*
J Clin Pathol. 57(9):960-4. 2004

[143]. Depeursinge A, Vargas A, Platon A, Geissbuhler A, Poletti PA. *Müller, H.. Building a reference multimedia database for interstitial lung diseases*. Comput Med Imaging Graph a. 36(3):227-38. 2012

[144]. Diciotti S, Lombardo S, Falchini M, Picozzi G, Mascalchi M, Ieee. *Automated segmentation refinement of small lung nodules in CT scans by local shape analysis*. Biomed Eng. 58(12):3418-28. 2011

[145]. Filho AO, de Sampaio WB, Silva AC, de Paiva AC, Nunes RA, Gattass M. *de Carvalho & Automatic detection of solitary lung nodules using quality threshold clustering, genetic algorithm and diversity index*. Artif Intell Med. 60(3):165-77. 2014

[146]. Song Y, Cai W, Zhou Y, Feng DD, Ieee. *Feature-based image patch approximation for lung tissue classification*. Med Imaging. 32(4 SRC - GoogleScholar):797-808. 2013

[147]. Real-Time P. *S. Beucher and C*. Lantuejoul Use of watersheds in contour detection In International Workshop on Image and Motion Detection Estimation. 1979

[148]. *Revised National Tuberculosis Control Programme*. Module for laboratory technicians New Delhi Directorate General of Health Services Ministry of Health and Family Welfare 15. 1999

[149]. Bhalla D. *Calculating Concordant, Discordant and Tied Pairs", (accessed 11 April*. 2014

[150]. Dayton CM. *Logistic regression analysis*. Stat.474-574. 1992

[151]. Sawadogo TL, Savadogo LG, Diande S, Ouedraogo F, Mourfou A, Gueye A, et al. *Nebié B., & Comparison of Kinyoun, auramine O, and Ziehl-Neelsen staining for diagnosing tuberculosis at the National Tuberculosis Center in Burkina Faso*. Med Sante Trop. 22(3):302-6. 2011

[152]. Dawson DJ, Kim SJ. *Quality Assurance of Sputum Microscopy in Dots Programmes: Regional Guidelines for Countries in the Western Pacific*: World Health Organization, Regional Office for the Western Pacific, Stop TB Special Project. 2003

[153]. Steingart KR, Henry M, Ng V, Hopewell PC, Ramsay A, Cunningham J, et al. *Fluorescence versus conventional sputum smear microscopy for tuberculosis: a systematic review*. The Lancet infectious diseases. 6(9):570-81. 2006

[154]. Goyal R, Kumar A. *A comparison of Ziehl-Neelsen staining and fluorescent microscopy for diagnosis of pulmonary tuberculosis*. IOSR J Dent Med Sci. 8:05-8. 2013

[155]. Depeursinge A, de Ville D, Platon A, Geissbuhler A, Poletti PA, Ieee. *Van & Müller, H.. Near-affine-invariant texture learning for lung tissue analysis using isotropic wavelet frames*. Inf Technol Biomed b. 16(4):665-75. 2012

[156]. Golosio B, Masala GL, Piccioli A, Oliva P, Carpinelli M, Cataldo R, et al. *A novel multithreshold method for nodule detection in lung CT*. Medical physics. 36(8):3607-18. 2009

[157]. Messay T, Hardie RC, Rogers SK. *A new computationally efficient CAD system for pulmonary nodule detection in CT imagery*. Medical image analysis. 14(3):390-406. 2010

[158]. Vollath D. *Automatic focusing by correlative methods*. Journal of Microscopy. 147(3):279-88. 1987

[159]. Vollath D. *The influence of the scene parameters and of noise on the behaviour of automatic focusing algorithms*. Journal of Microscopy. 151(2):133-46. 1988

[160]. Shenai S, Minion J, Vadwai V, Tipnis T, Shetty S, Salvi A, et al. *Evaluation of light emitting diode-based fluorescence microscopy for the detection of mycobacteria in a tuberculosis-endemic region*. The International Journal of Tuberculosis and Lung Disease. 15(4):483-8. 2011

[161]. Brenner JF, Dew BS, Horton JB, King T, Neurath PW, Selles WD. *An automated microscope for cytologic research a preliminary evaluation*. Journal of Histochemistry & Cytochemistry. 24(1):100-11. 1976

[162]. Subbarao M, Choi T-S, Nikzad A. *Focusing techniques*. Optical Engineering. 32(11):2824-37. 1993

[163]. Nayar SK, Nakagawa Y. *Shape from focus*. IEEE Transactions on Pattern analysis and machine intelligence. 16(8):824-31. 1994

[164]. Thelen A, Frey S, Hirsch S, Hering P. *Improvements in shape-from-focus for holographic reconstructions with regard to focus operators, neighborhood-size, and height value interpolation*. IEEE Transactions on Image Processing. 18(1):151-7. 2009

[165]. Yang G, Nelson BJ, editors. *Wavelet-based autofocusing and unsupervised segmentation of microscopic images*. Intelligent Robots and Systems, 2003(IROS 2003) Proceedings 2003 IEEE/RSJ International Conference on; 2003

[166]. Xie H, Rong W, Sun L, editors. *Wavelet-based focus measure and 3-d surface reconstruction method for microscopy images*. Intelligent Robots and Systems, 2006 IEEE/RSJ International Conference on; 2006

[167]. Helmli FS, Scherer S, editors. *Adaptive shape from focus with an error estimation in light microscopy*. Image and Signal Processing and Analysis, 2001 ISPA 2001 Proceedings of the 2nd International Symposium on; 2001

[168]. Minhas R, Mohammed AA, Wu QJ. *An efficient algorithm for focus measure computation in constant time*. IEEE Transactions on Circuits and Systems for Video Technology. 22(1):152-6. 2012

[169]. Widjaja J, Jutamulia S, editors. *Wavelet transform-based autofocus camera systems*. Circuits and Systems, 1998 IEEE APCCAS 1998 The 1998 IEEE Asia-Pacific Conference on; 1998

[170]. Kang Z-m, Zhang L, Xie P. *Implementation of an automatic focusing algorithm based on spatial high frequency energy and entropy*. Acta Electronica Sinica. 31(4):552-5. 2003

[171]. Kongfeng GZJWZ. *Auto-focusing Algorithm Based on Most Gradient and Threshold [J]*. Journal of Electronic Measurement and Instrument. 5:014. 2007

[172]. Benes R, Dvorak P, Faundez-Zanuy M, Espinosa-Duro V, Mekyska J. *Multi-focus thermal image fusion*. Pattern recognition letters. 34(5):536-44. 2013

[173]. Zukal M, Mekyska J, Cika P, Smekal Z. *Interest points as a focus measure in multi-spectral imaging*. Radioengineering. 22(1):68-81. 2013

[174]. Xu X, Wang Y, Tang J, Zhang X, Liu X. *Robust automatic focus algorithm for low contrast images using a new contrast measure*. Sensors. 11(9):8281-94. 2011

[175]. Shah MI, Mishra S, Yadav VK, Chauhan A, Sarkar M, Sharma SK, et al. *Ziehl–Neelsen sputum smear microscopy image database: a resource to facilitate automated bacilli detection for tuberculosis diagnosis*. Journal of Medical Imaging. 4(2):027503. 2017

[176]. Shah M, Mishra S, Sarkar M, Rout C. *Identification of robust focus measure functions for the automated capturing of focused images from Ziehl–Neelsen stained sputum smear microscopy slide*. Cytometry Part A. 2017

[177]. Veropoulos K, Campbell C, Learmonth G. *Image processing and neural computing used in the diagnosis of tuberculosis*. 1998

[178]. de Jager K, Fickling S, Krishnan S, Jabbari M, Learmonth GW, Douglas TS. *Automated fluorescence microscope for tuberculosis detection*. Journal of Medical Devices. 8(3):030943. 2014

[179]. Priya E, Srinivasan S. *Automated decision support system for tuberculosis digital images using evolutionary learning machines*. European Journal for Biomedical Informatics. 9(2):3-8. 2013

[180]. CostaFilho CF, Levy PC, Xavier CM, Costa MG, Fujimoto LB, Salem J, editors. *Mycobacterium tuberculosis recognition with conventional microscopy*. Engineering in Medicine and Biology Society (EMBC), 2012 Annual International Conference of the IEEE; 2012

[181]. Zhai Y, Liu Y, Zhou D, Liu S, editors. *Automatic identification of mycobacterium tuberculosis from ZN-stained sputum smear: Algorithm and system design*. Robotics and Biomimetics (ROBIO), 2010 IEEE International Conference on; 2010

[182]. Beucher S, Lantuéjoul C. *Use of watersheds in contour detection*. 1979

[183]. Tarabalka Y, Chanussot J, Benediktsson JA. *Segmentation and classification of hyperspectral images using watershed transformation*. Pattern Recognition. 43(7):2367-79. 2010

PUBLICATIONS

Journal Publications

1. **Shah MI,** Mishra S, Yadav VK , Chauhan A, Sarkar M, Sudarshan SK, Rout C. "Ziehl–Neelsen sputum smear microscopy image database: a resource to facilitate automated bacilli detection for tuberculosis diagnosis", *J. Med. Imag*. 4(2), 027503 (Jun 30, 2017).; **DOI: 10.1117/1.JMI.4.2.027503**

2. **Shah MI,** Mishra S, Sarkar M, Rout C. "Identification of robust focus measure functions for the automated capturing of focused images from Ziehl–Neelsen stained sputum smear microscopy slide." Cytometry Part A. 2017 Jun 2. **DOI: 10.1002/cyto.a.23142**

3. **Shah MI,** Mishra S, Rout C. Establishment of hybridized focus measure functions as a universal method for autofocusing. Journal of Biomedical Optics. 2017 Dec;22(12): 126004. **DOI: 10.1117/1.JBO.22.12.126004**

Conference Publications

1. **Shah MI**, Mishra S, Sarkar M, Sudarshan SK. "Automatic detection and classification of tuberculosis bacilli from camera-enabled smartphone microscopic images." In Fourth International Conference on Parallel, Distributed and Grid Computing, 2016 Dec (pp. 287-290). IEEE. **DOI: 10.1109/PDGC.2016.7913161**

2. **Shah MI**, Mishra S, Sarkar M, Rout C. "Automatic Detection and Classification of Tuberculosis Bacilli from ZN-stained Sputum Smear Images using Watershed Segmentation." In International Conference on Signal Processing (ICSP), 2016 Nov (pp. 20-4.). IET. **DOI: 10.1049/cp.2016.1459**